Quantum control and information processing in atoms and ions

Svetoslav Stoychev Ivanov

Supervisor: Prof. D.Sc. Nikolay V. Vitanov

A thesis presented for the degree of
Doctor of Philosophy

Group of Quantum Optics and Quantum Information
Theoretical Physics Division
Faculty of Physics
SOFIA UNIVERSITY ST. KLIMENT OHRIDSKI
Sofia

February 2010

Copyright

This thesis is based on research carried out in the *Group of Quantum Optics and Quantum information*, Department of Theoretical Physics, Sofia University "St. Kliment Ohridski". The author has not submitted any part of the thesis elsewhere for any other degree or qualification.

Acknowledgements

I am grateful to my supervisor Prof. D.Sc. Nikolay Vitanov for his support throughout the past five years. I would like also to express my acknowledgement to the European Commission projects EMALI and FASTQUAST, the Bulgarian National Science Fund grants VU-F-205/06, VU-I-301/07, D002-90/08, and Sofia University Grant No. 020/2009 for the financial support. I am thankful to all members and guests of the Group of Quantum Optics and Quantum information at Sofia University for useful discussions.

Contents

Introduction

Many branches of contemporary physics require atoms or molecules prepared in specified quantum states not only for traditional studies of different quantum processes, but also in more recently developing research areas of atom optics and quantum information. Of great interest is the fraction of all atoms or molecules in a specific state, a time-varying probability here termed the *population* $P(t)$. Schemes for transferring population selectively (i.e., to a single predetermined quantum state), such as excitation with frequency-swept pulses and stimulated Raman adiabatic passage (STIRAP), have opened new opportunities for coherent control of atomic and molecular processes. With the growing interest of quantum information, there is also concern with creating and controlling specified coherent superpositions of quantum states.

The first part of this thesis describes techniques that can be used to control state vectors and, in particular, to transfer population selectively, between quantum states of atoms or molecules. One goal of the theory of coherent excitation is to predict, for a given set of radiation pulses, the probabilities that the atoms will undergo a transition between the initial state and the desired target state (population *transfer efficiency*). More generally, theory can predict the changes of a state vector $\psi(t)$ produced by specified radiation. Alternatively, theory can provide a prescription of pulses that will produce a desired population transfer or state vector change.

We begin with a brief summary of the theory of coherent control of quantum systems, focusing on adiabatic transfer schemes. The theoretical description of such schemes is most easily presented with the aid of adiabatic states: if the evolution is adiabatic, then at all times the state vector remains aligned with one of these states. The progress of the changing state vector can be followed by viewing a plot of adiabatic eigenvalues and noting the crossings of diabatic energies. Whenever such crossings are encountered, the transition probability is traditionally estimated by the famous Landau-Zener (LZ) formula [1]. Although the LZ model involves the simplest nontrivial time dependence – linearly changing energies and a constant interaction of infinite duration, when applied to real physical systems with more sophisticated time dependences the LZ model often provides more accurate results than expected. This

feature, and the extreme simplicity of the LZ transition probability, have determined the vast popularity of the model, despite the availability of more sophisticated exactly soluble level-crossing models. That motivated us to use the LZ model to develop the theory of coherent manipulation, which is presented in part one.

The second part of the thesis concerns quantum information processing with trapped ions. The ions, or charged atomic particles, are confined and suspended in free space using electromagnetic fields. Qubits are stored in stable electronic states of each ion, and quantum information is processed and transferred through the collective quantized motion of the ions in the trap (interacting through the Coulomb force). Lasers are applied to induce coupling between the qubit states (for single qubit operations) or coupling between the internal qubit states and the external motional states (for entanglement between qubits). The fundamental operations of a quantum computer have been demonstrated experimentally with high accuracy in trapped ion systems and a strategy has been developed for scaling the system to arbitrarily large numbers of qubits by shuttling ions in an array in the ion traps. This makes the trapped ion quantum computer system one of the most promising architectures for a scalable, universal quantum computer.

Working in the trapped-ion framework we developed the quantum search algorithm, which is one of the most celebrated applications of quantum information processing. It allows an initially unknown element to be determined from $\mathcal{N}$ equally likely possibilities in $O(\sqrt{\mathcal{N}})$ queries [2]. This outperforms the optimum classical strategy (a random 'trial and error' of elements), which requires $O(\mathcal{N})$ steps on average. Proof-of-principle quantum search has been successfully demonstrated in nuclear magnetic resonance, linear optical and trapped-ion systems, as well as with individual Rydberg atoms and in classical optics. Of these, only the trapped-ion platform possesses a fully scalable Hilbert space and in this sense it is realistically the only candidate for performing a practically useful quantum search. We note, however, that while the trapped-ion system is scalable, the largest dimensional quantum search so far performed with trapped ions was for a database size of $\mathcal{N} = 4$ [3]. Extending the approach of Ref. [3] to a large number of ions in the traditional way is highly demanding, since it requires an enormous amount of physical operations. However, we found an elegant way to a simple implementation of the algorithm, which is presented in part two. The technique proposed raises the prospect of demonstrating Grover's algorithm in a moderately sized trapped-ion database comprising up to several hundred elements; this is a necessary step on the path to demonstrating a practically useful quantum search, which remains a long-term goal for quantum information processing.

Part I

Coherent Control of Quantum Systems

Chapter 1

Two-State System in an External Pulsed Field

The present chapter presents the basic quantum theory of light-atom interaction for a two state atom governed by the time-dependent Scrödinger equation. Light with circular and linear polarization is investigated. The rotating-wave approximation is derived and the concept of diabatic and adiabatic basis is presented.

1.1 The Two-State Schrödinger Equation

The Schrödinger picture of quantum dynamics describes probability distributions for atomic states. It does so by means of probability amplitudes, whose absolute squares provide the desired probabilities. The states referenced by the probability may be states in which an atomic electron has a definite position, in which case the probability amplitude is known as a wavefunction. However, our concern is not primarily with electron density distributions within atoms, but rather with excitation from one stationary state to another. These are states in which, when no radiation is present, the atom has sharply defined energy. (In the absence of spontaneous emission they are stationary states.) They may be labeled by the value of the excitation energy and by any other convenient, mutually compatible labels or, more simply, they may just be assigned indices $1, 2, \ldots$ within a suitable catalog. We require probability amplitudes for these states, but we need not be concerned with the internal atomic dynamics (the electron behavior) associated with the states.

The description of the internal excitation of a quantum system in a *pure state*, is embodied

in a *state vector* $\Psi(t) \in \mathcal{H}$ and we can express it as a time-varying superposition,

$$\Psi(t) = \sum_n C_n(t) \exp\{-i\zeta_n(t)\}\psi_n, \tag{1.1}$$

where the phase $\zeta_n(t)$ is chosen *a priori* for mathematical convenience, and the complex valued function of time $C_n(t)$ is a *probability amplitude*, whose absolute square is the probability $P_n(t)$ that the atom will be found in state ψ_n during a measurement

$$P_n(t) = |C_n(t)|^2 = |(\psi_n, \Psi(t))|^2 . \tag{1.2}$$

If the quantum system is closed, then the sum of all probability amplitudes does not change with time, but remains unity,

$$\sum_n P_n(t) = 1. \tag{1.3}$$

Probability conservation (1.3) amounts to the statement that the state vector maintains constant (unit) norm at all time,

$$(\Psi, \Psi) = 1. \tag{1.4}$$

We chose the basis states to be stationary and this means that they are eigenstates of $\hat{H}^0$ and satisfy the *time-independent Schrödinger equation*

$$\hat{H}^0\psi_i = E_i^0\psi_i, \tag{1.5}$$

where $\hat{H}^0$ is a time-independent Hamiltonian operator, which governs the evolution of the system when no external field is applied. In terms of the laser field interactions this assumption suggests that if the system is initialized in a stationary state it will remain in it, so long as no external force intervenes.

Once we introduce a laser field to interact with the quantum system, the state vector varies, governed by the *time-dependent Schrödinger equation* (in units $\hbar = 1$),

$$i\frac{d}{dt}\Psi(t) = \hat{H}(t)\Psi(t), \tag{1.6}$$

where $\hat{H}(t)$ is the Hamiltonian operator, which represents the total energy of the system – the sum of kinetic, potential and interaction energies. When the external field depends upon time (as they do when the interaction begins and ends at finite times or is periodic), the elements of the matrix $\hat{H}(t)$ depend explicitly upon time either.

Equation (1.6) underlies all nonrelativistic descriptions of microscopic temporal behavior. It is the basis for the quantum mechanical description of coherent excitation. In particular,

it provides the foundation of all discussions of coherent excitation and defines the dynamical behavior of a quantum system.

The definition of a state vector $\Psi(t)$ in energy representation (1.1) has some flexibility in choosing the phases $\zeta_n(t)$. Their choice, for a given representation, establishes a *picture*. The simplest, and most obvious choice, $\zeta_n \equiv 0$, defines the *Schrödinger picture*.

1.1.1 The Two-State Schrödinger Atom

The idealized notion of two-state system provides the simplest application of time-dependent Scrödinger equation. By definition, such system can exist in two, and only two, possible states of motion – a ground state ψ_1 and an excited state ψ_2.

The Hilbert space for this system is 2-dimensional and the space vector is expressed as

$$\Psi(t) = C_1(t)\exp\{-i\zeta_1(t)\}\psi_1 + C_2(t)\exp\{-i\zeta_2(t)\}\psi_2, \tag{1.7}$$

where the complex-valued expansion coefficient $C_i(t)$ is the projection of the state vector $\Psi(t)$ onto the fixed basis vector ψ_i.

Let us assume the case of no external forces acting upon the system and substitute the state vector (1.7) into the Schrödinger equation (in units $\hbar = 1$)

$$i\frac{d}{dt}\Psi(t) = E_1^0 e^{-i\zeta_1(t)}C_1(t)\psi_1 + E_2^0 e^{-i\zeta_2(t)}C_2(t)\psi_2.$$

Taking into account that the basis states are stationary we multiply this equation sequentially with ψ_1 and ψ_2 from the left. As a result we obtain a set of two independent first-order linear differential equations for the probability amplitudes

$$i\dot{C}_n(t) = \left(E_n^0 - \dot{\zeta}_n(t)\right)C_n(t)\ , \quad n = 1, 2\ . \tag{1.8}$$

The solution is a probability amplitude with time evolution only in its phase,

$$C_n(t) = C_n(0)\exp\{-i(E_n^0 - \dot{\zeta}_n(t))t/\}, \tag{1.9}$$

and so the probabilities remain fixed at their initial values

$$P_n(t) = |C_n(0)|^2 = P_n(0)\,. \tag{1.10}$$

This constancy implies the meaning of a stationary state.

If the system interacts with a laser field, its Hamiltonian operator $\hat{H}(t)$ from the time-dependent Schrödinger equation (1.6), can be expressed as a sum of the time-independent

Hamiltonian $\hat{H}^0$ and another operator $\hat{V}(t)$, representing the perturbative time-dependent interaction with the pulsed field

$$\hat{H}(t) = \hat{H}^0 + \hat{V}(t). \tag{1.11}$$

We assume that $\hat{H}(t)$ is Hermitian, which provides real eigenvalues and hence real excitation energies. This, together with (1.11), suggests that the interaction operator $\hat{V}(t)$ is also Hermitian, i.e. its matrix elements satisfy

$$\hat{V}_{ij} = \hat{V}^*_{ji}. \tag{1.12}$$

The time-dependent Schrödinger equation for the state vector

$$i\frac{d}{dt}\begin{bmatrix} C_1(t) \\ C_2(t) \end{bmatrix} = \begin{bmatrix} E_1^0 - \dot{\zeta}_1(t) + \hat{V}_{11}(t) & \hat{V}_{12}(t)e^{-i\zeta_2(t)+i\zeta_1(t)} \\ \hat{V}_{21}(t)e^{-i\zeta_1(t)+i\zeta_2(t)} & E_2^0 - \dot{\zeta}_2(t) + \hat{V}_{22}(t) \end{bmatrix} \begin{bmatrix} C_1(t) \\ C_2(t) \end{bmatrix} \tag{1.13}$$

is transformed in a set of two coupled first order differential equations for the probability amplitudes $C_n(t)$. Written in a vector–matrix form this reads

$$i\frac{d}{dt}\mathbf{C}(t) = \hat{H}(t)\mathbf{C}(t), \tag{1.14}$$

where $\mathbf{C}(t) = [C_1(t), C_2(t)]^T$.

The two-state problem is to determine the probabilities at $t \to \infty$, $|C_m(\infty)|^2$, $m = 1, 2$, if we know their initial values (at $t \to -\infty$). We usually solve (1.13) with initial conditions

$$C_1(-\infty) = 1, \quad C_2(-\infty) = 0, \tag{1.15}$$

which physically means that in the beginning of the evolution the system was in state ψ_1. Equation (1.13), together with initial conditions (1.15), completes the mathematical description of the two-state atom. The Schrödinger picture suggests that all phases in the expression for the state vector (1.7) are fixed at zero and

$$\Psi(t) = \sum_{n=1}^{2} C_n(t)\psi_n. \tag{1.16}$$

The equations for the probability amplitudes obtain the form

$$i\frac{d}{dt}\begin{bmatrix} C_1(t) \\ C_2(t) \end{bmatrix} = \begin{bmatrix} E_1^0 + \hat{V}_{11}(t) & \hat{V}_{12}(t) \\ \hat{V}_{21}(t) & E_2^0 + \hat{V}_{22}(t) \end{bmatrix} \begin{bmatrix} C_1(t) \\ C_2(t) \end{bmatrix}. \tag{1.17}$$

Although, it may look easier to solve this set of equations, compared to the set involving time-dependent phases (1.13), in many cases this assumption proves wrong. The freedom of choosing the phases $\zeta_n(t)$ often gives us the advantage to solve the set (1.13) analytically.

1.1.2 Light–Atom Interaction

For radiation within the optical region of the spectrum, wavelengths are much larger than the atomic dimensions and we can assume that the interaction is that between a spatially uniform electric field and an atomic dipole moment. The interaction energy is

$$\hat{V}(t) = -\mathbf{d} \cdot \mathbf{E}(t), \tag{1.18}$$

where $\mathbf{d}$ is the atomic dipole transition moment operator and $\mathbf{E}(t)$ is the electric field operator evaluated at the center of mass of the atom. For electric dipole induced transitions amongst bound atomic states of an isolated atom the matrix representation of $\hat{V}(t)$ usually has no diagonal elements. If the external field is *static* any diagonal elements, $\hat{V}_{nn}$, would produce an energy shift in the undisturbed energies of the atom. With a simple phase transformation of the kind

$$\tilde{C}_n(t) = C_n(t) \exp\{-i\hat{V}_{nn}t\}, \tag{1.19}$$

this energy shift can be incorporated in the definition of the probability amplitudes. This is identical to fixing the diagonal elements of $\hat{V}(t)$ at zero. Therefore, we shall assume that the only nonvanishing two-state elements of the interaction Hamiltonian are those that connect state ψ_1 to state ψ_2.

In the simplest examples the electric field $\mathbf{E}(t)$ has the form of a periodic variation at a carrier frequency (the optical frequency ω)and a more slowly varying envelope $\mathcal{E}(t)$

$$\mathbf{E}(t) = e\mathcal{E}(t)\cos(\omega t + \phi) = \frac{1}{2}e\,|\mathcal{E}(t)|\,[\exp\{i\omega t + i\phi\} + \exp\{-i\omega t - i\phi\}], \tag{1.20}$$

where e is a unit vector defining the direction of the electric field vector, i.e. the polarization direction, and ϕ is the phase of the amplitude $\mathcal{E}(t)$, i.e. the phase of the laser wave.

We need to determine the matrix element of the dipole transition moment between basis states 1 and 2, which is the component of the vector operator $\mathbf{d}$ along the direction of the electric field. The quantitive description of the atomic properties enters the theory through the matrix elements

$$(\psi_n, \mathbf{d} \cdot e\psi_m) \equiv \mathbf{d}_{nm} \cdot e. \tag{1.21}$$

Using these definitions and approximations we can write the nonvanishing matrix elements of the interaction as

$$\hat{V}_{21}(t) = -\mathbf{d}_{21} \cdot e\frac{1}{2}\,|\mathcal{E}(t)|\,\mathrm{Re}[\exp\{i\omega t + i\phi\}] = \hat{V}_{12}^{*}(t). \tag{1.22}$$

1.1.3 Light with Circular Polarization

The treatment of the interaction between an atom and circularly polarized light involves complex unit vectors. For complex-valued vectors e, say the vector appropriate to right-circular polarization $e = (e_x - ie_y)/\sqrt{2}$, the matrix element becomes

$$\begin{aligned}\hat{V}_{21}(t) &= -\frac{1}{2}\left(\psi_2, (d_x - id_y)\,\psi_1\right)\frac{|\mathcal{E}(t)|}{\sqrt{2}}\exp\{-i\omega t - i\phi\} \\ &\quad -\frac{1}{2}\left(\psi_2, (d_x + id_y)\,\psi_1\right)\frac{|\mathcal{E}(t)|}{\sqrt{2}}\exp\{i\omega t + i\phi\},\end{aligned} \tag{1.23}$$

The replacement $id_y \to -id_y$ gives the matrix elements for left-circular polarization. Angular momentum selection rules ordinarily permit only one of the operators $d_x + id_y$ or $d_x - id_y$ to have non-zero matrix elements between any two states, so that one of the contributions to $\hat{V}_{21}(t)$ vanishes. Expression (1.23) shows that for light with circular polarization the interaction element of the Hamiltonian $\hat{V}_{21}(t)$ is complex valued – it is proportional to either $\exp\{+i\omega t\}$ or $\exp\{-i\omega t\}$. We see that

$$\hat{V}_{21}(t) = \begin{cases} \frac{1}{2}\Omega(t)\exp\{i\omega t + i\phi\}, \\ \frac{1}{2}\Omega(t)\exp\{-i\omega t - i\phi\}, \end{cases} \qquad \text{for circular polarization,} \tag{1.24}$$

where $\Omega(t)$ is real-valued quantity with dimension of angular frequency. This frequency is known as the *Rabi frequency*. Together with the Bohr frequency ω_0 and the interaction frequency ω, the Rabi frequency provides one of the three characteristic time scales for the coherent atomic excitation, and it parameterizes the interaction strength between the atom and the external field. For the expression above, the Rabi frequency is evaluated as

$$|\Omega(t)| = |\mathbf{d}_{21}\cdot e|\,|\mathcal{E}(t)|\,. \tag{1.25}$$

So, the elements of the interaction Hamiltonian are

$$\hat{V}_{11}(t) = \hat{V}_{22}(t) = 0, \tag{1.26a}$$

$$\hat{V}_{21}(t) = \hat{V}^*_{12}(t) = \frac{1}{2}\Omega(t)\exp\{-i\omega t - i\phi\} \tag{1.26b}$$

and we substitute them in the time-dependent Schrödinger equation

$$i\frac{d}{dt}C_1(t) = (E_1^0 - \dot{\zeta}_1(t))C_1(t) + \frac{1}{2}\Omega(t)e^{i(\omega t+\phi)}e^{-i\zeta_2(t)+i\zeta_1(t)}C_2(t) \tag{1.27a}$$

$$i\frac{d}{dt}C_2(t) = \frac{1}{2}\Omega(t)e^{-i(\omega t+\phi)}e^{-i\zeta_1(t)+i\zeta_2(t)}C_1(t) + (E_2^0 - \dot{\zeta}_2(t))C_2(t). \tag{1.27b}$$

From this expression we can see that by choosing the arbitrary phase functions $\zeta_n(t)$ appropriately we can simplify these equations and eliminate completely the time-varying exponential factors.

Let us set

$$\zeta_2(t) - \zeta_1(t) = \omega t + \phi \tag{1.28}$$

and fix $\dot{\zeta}_1(t)$ to be

$$\dot{\zeta}_1(t) = E_1^0 + \frac{1}{2}\Delta(t), \tag{1.29}$$

which is the *Dirac picture*. Here we introduce *the detuning* $\Delta(t)$

$$\Delta(t) = \omega_0 - \omega, \tag{1.30}$$

which is the difference between the atomic Bohr (or transition) frequency ω_0 and the carrier frequency of the laser pulse ω.

The next step is to put these phases in (1.27) and as a result we obtain

$$i\frac{d}{dt}\begin{bmatrix} C_1(t) \\ C_2(t) \end{bmatrix} = \frac{1}{2}\begin{bmatrix} -\Delta(t) & \Omega(t) \\ \Omega(t) & \Delta(t) \end{bmatrix}\begin{bmatrix} C_1(t) \\ C_2(t) \end{bmatrix}. \tag{1.31}$$

These equations govern the dynamics of a two-state system under the influence of the exponentially oscillating interaction (1.26a).

1.1.4 Light with Linear Polarization

For a linearly polarized laser wave we can choose the unit vector e, defining the polarization direction to be real. By introducing real unit vectors $\mathbf{e}(x)$, $\mathbf{e}(y)$ and $\mathbf{e}(z)$ we can express the atomic dipole operator in Cartesian coordinates

$$\mathbf{d} = d_x\mathbf{e}(x) + d_y\mathbf{e}(x) + d_z\mathbf{e}(x). \tag{1.32}$$

The interaction takes simplest form if we choose the atomic axis z to lie along the polarization direction $e = \mathbf{e}(z)$, for then we have the expression

$$\hat{V}_{21}(t) = -\left(\psi_2, \hat{d}_z\psi_1\right)|\mathcal{E}(t)|\cos(\omega t + \phi). \tag{1.33}$$

This expression makes it clear, that for a linear polarization of monochromatic light, $\hat{V}_{21}(t)$ may be taken as real-valued. We conclude that the matrix elements of the interaction operator $\hat{V}(t)$ in the stationary basis are

$$\hat{V}_{11}(t) = \hat{V}_{22}(t) = 0, \tag{1.34a}$$

$$\begin{aligned}\hat{V}_{12}(t) &= \hat{V}_{21}(t) = \hat{V}_{21}\cos(\omega t + \phi) \\ &= \frac{1}{2}\hat{V}_{21}[\exp\{i\omega t + i\phi\} + \exp\{-i\omega t - i\phi\}],\end{aligned} \tag{1.34b}$$

where V_{21} is real. We substitute them in Eq. (1.13) and the full Hamiltonian operator for this type of interaction in this basis has the explicit elements

$$\hat{H}(t) = \begin{bmatrix} E_1^0 - \dot{\zeta}_1(t) & \frac{1}{2}\hat{V}_{21}[e^{i\omega t+i\phi} + e^{-i\omega t-i\phi}]e^{-i\zeta_2(t)+i\zeta_1(t)} \\ \frac{1}{2}\hat{V}_{21}[e^{i\omega t+i\phi} + e^{-i\omega t-i\phi}]e^{i\zeta_2(t)-i\zeta_1(t)} & E_2^0 - \dot{\zeta}_2(t). \end{bmatrix} \tag{1.35}$$

As we saw above, a suitable choice of the phases can often facilitate solution of the Schrödinger equation, so we introduce the so-called *rotating-wave picture*, in which the phase difference is set to

$$\zeta_2(t) - \zeta_1(t) = \omega t + \zeta_0, \tag{1.36}$$

where ζ_0 is independent of time. By doing so, the difference $\zeta_2 - \zeta_1$ incorporates the time dependence $\pm\omega t$ and we can replace one of the two exponentials in Eq. (1.35) with unity. With the further choice (as in the case for complex-valued interactions)

$$\dot{\zeta}_1(t) = E_1^0 + \frac{1}{2}\Delta(t), \tag{1.37a}$$

$$\dot{\zeta}_2(t) = E_2^0 - \frac{1}{2}\Delta(t), \tag{1.37b}$$

the final form of the time-dependent Schrödinger equation, with the Hamiltonian (1.35), is

$$i\frac{d}{dt}\begin{bmatrix} C_1(t) \\ C_2(t) \end{bmatrix} = \frac{1}{2}\begin{bmatrix} -\Delta(t) & \Omega(t)[1 + e^{-2i(\omega t+\phi)}] \\ \Omega^*(t)[1 + e^{2i(\omega t+\phi)}] & \Delta(t) \end{bmatrix}\begin{bmatrix} C_1(t) \\ C_2(t) \end{bmatrix}. \tag{1.38}$$

The Rabi frequency $\Omega(t)$ that appears in the Hamiltonian operator is defined as

$$\Omega(t) = \hat{V}_{21}\exp\{i\phi - i\zeta_0\}, \tag{1.39}$$

and so it may be complex-valued. This Rabi frequency is connected to the interaction Rabi frequency (1.25) through a phase transformation and for simplicity we denote them with one and the same symbol. If and only if, the excitation phase ϕ remains fixed, then it is always possible to choose the arbitrary constant ζ_0 such that $\Omega(t)$ becomes real and positive.

In Eq. (1.38) we involved no approximations, apart form that of a two-state atom. The rotating-wave picture is particularly suited to the use of approximations that allow simple exact solutions, as we shall see next.

1.2 Rotating-Wave Approximation (RWA)

The principle concern in laser-induced excitation is with optical frequencies ω much larger than the Rabi frequency Ω. To eliminate the uninteresting high frequency components that oscillate

at frequency ω, we average the differential equations over the optical period $\tau = 2\pi/\omega$ and obtain the cycle-averaged amplitude and derivative

$$\bar{C}_n(t) = \frac{1}{\tau}\int_t^{t+\tau} C_n(t')dt', \tag{1.40a}$$

$$\frac{d}{dt}\bar{C}_n(t) = \frac{1}{\tau}\int_t^{t+\tau} \frac{d}{dt'}C_n(t')dt'. \tag{1.40b}$$

We assume that during such an interval the function $C_n(t)$ changes very little. Under this condition we may replace the cycle average of $\exp\{2i\omega t\}C_n(t)$ by its average value, zero

$$\frac{1}{\tau}\int_t^{t+\tau} \exp\{2i\omega t'\}C_n(t')dt' \simeq \bar{C}_n(t)\frac{1}{\tau}\int_t^{t+\tau} \exp\{2i\omega t'\}dt' = 0. \tag{1.41}$$

This approximation, known in the context of the two-state atomic excitation as the *rotating-wave approximation* (RWA) [4,5], essentially assumes that the exponential $\exp\{2i\omega t\}$ undergoes many oscillations during the time needed for $C_n(t)$ to change appreciably. Thus, the RWA amounts to the replacement

$$\{1 + \exp\{2i\omega t\}\} \simeq 1 \tag{1.42}$$

for the time average. In this approximation the Schrödinger equation obtains the form

$$i\frac{d}{dt}\begin{bmatrix} C_1(t) \\ C_2(t) \end{bmatrix} = \frac{1}{2}\begin{bmatrix} -\Delta(t) & \Omega(t) \\ \Omega^*(t) & \Delta(t) \end{bmatrix}\begin{bmatrix} C_1(t) \\ C_2(t) \end{bmatrix}, \tag{1.43}$$

where the overline explicitly indicates time average, is omitted, and we will simply have $C_n(t)$ instead of $\bar{C}_n(t)$. The dynamical behavior becomes identical to that of a two-state atom subjected to a suddenly-applied steady interaction.

1.3 Adiabatic Basis, Adiabatic Approximation

The Schrödinger equation (1.14) is rewritten in the so-called *diabatic basis*, which is the stationary basis of the system, involving the time-independent Hamiltonian $\hat{H}^0$ eigenvectors (ψ_1, ψ_2)(1.5). However, we have the possibility to choose any other basis, for mathematical convenience, which would simplify the expression of the Schrödinger equation. Theoretical discussion of time-evolving quantum systems is greatly facilitated by introducing instantaneous eigenstates (Φ_-, Φ_+) of the time-varying Hamiltonian matrix

$$\hat{H}(t)\Phi_i(t) = \varepsilon_i(t)\Phi_i(t), \quad (i = -, +). \tag{1.44}$$

Because the Hamiltonian changes with time, both the eigenvalues $\varepsilon_i(t)$ and the eigenvectors, the *adiabatic states* $\Phi_i(t)$, will change with time. Knowing the explicit form of the time-dependent Hamiltonian (1.43), it is easy to find its eigenvalues

$$\varepsilon_{\pm}(t) = \pm\frac{1}{2}\sqrt{\Omega^2(t) + \Delta^2(t)} \tag{1.45}$$

and their difference

$$\varepsilon(t) = \varepsilon_{+}(t) - \varepsilon_{-}(t) = \sqrt{\Omega^2(t) + \Delta^2(t)}\,, \tag{1.46}$$

which defines the energy splitting. We express the state vector $\Psi(t)$ as a superposition of the adiabatic states

$$\Psi(t) = A_{-}(t)\Phi_{-}(t) + A_{+}(t)\Phi_{+}(t) \tag{1.47}$$

with coefficients $A_{-}(t)$ and $A_{+}(t)$. Comparing it with the expression for the state vector, written in the diabatic basis (1.7), we find that the two bases are connected through orthogonal rotating transformation

$$\begin{bmatrix} \Phi_{-}(t) \\ \Phi_{+}(t) \end{bmatrix} = \underbrace{\begin{bmatrix} \cos\vartheta(t) & -\sin\vartheta(t) \\ \sin\vartheta(t) & \cos\vartheta(t) \end{bmatrix}}_{\hat{R}^{-1}(\vartheta(t))} \begin{bmatrix} \psi_1 \\ \psi_2 \end{bmatrix}, \tag{1.48}$$

or shortly

$$\mathbf{\Phi}(t) = \hat{R}^{-1}(\vartheta(t))\psi\,, \tag{1.49}$$

where $\mathbf{\Phi}(t) = [\Phi_{-}(t), \Phi_{+}(t)]^{\mathrm{T}}$ and $\psi = [\psi_1, \psi_2]^{\mathrm{T}}$. The rotating angle $\vartheta(t)$, being a function of time, is defined as follows

$$\tan 2\vartheta(t) = \frac{\Omega(t)}{\Delta(t)}\,. \tag{1.50}$$

The connection between the superposition coefficients for the diabatic basis $(C_1(t), C_2(t))$ and the adiabatic basis $(A_{-}(t), A_{+}(t))$ is expressed in terms of $\hat{R}(\vartheta(t))$

$$\begin{bmatrix} C_1(t) \\ C_2(t) \end{bmatrix} = \underbrace{\begin{bmatrix} \cos\vartheta(t) & \sin\vartheta(t) \\ -\sin\vartheta(t) & \cos\vartheta(t) \end{bmatrix}}_{\hat{R}(\vartheta(t))} \begin{bmatrix} A_{-}(t) \\ A_{+}(t) \end{bmatrix}. \tag{1.51}$$

Substituting the adiabatic states as a time-varying superposition (1.49) in the expression (1.44), we obtain that

$$\hat{R}^{-1}(\vartheta(t))\hat{H}(t)\hat{R}(\vartheta(t)) = \begin{bmatrix} -\varepsilon & 0 \\ 0 & +\varepsilon \end{bmatrix}. \tag{1.52}$$

Let's rewrite the Schrödinger equation in the adiabatic basis. We use its representation in the diabatic basis (1.14) and express the diabatic amplitudes according to (1.51)

$$i\frac{d}{dt}[\hat{R}(\vartheta(t))\mathbf{A}(t)] = \hat{H}(t)[\hat{R}(\vartheta(t))\mathbf{A}(t)]\,. \tag{1.53}$$

After taking the time derivative, the result for the Schrödinger equation is

$$i\frac{d}{dt}\mathbf{A}(t) = [\underbrace{\hat{R}^{-1}(\vartheta(t))\hat{H}(t)\hat{R}(\vartheta(t))}_{\text{diagonal part}} - i\underbrace{\hat{R}^{-1}(\vartheta(t))\dot{\hat{R}}(\vartheta(t))}_{\text{non-diagonal part}}]\mathbf{A}(t)\,, \tag{1.54}$$

or written in matrix form

$$i\frac{d}{dt}\begin{bmatrix} A_-(t) \\ A_+(t) \end{bmatrix} = \begin{bmatrix} -\varepsilon & -i\dot{\vartheta} \\ i\dot{\vartheta} & +\varepsilon \end{bmatrix}\begin{bmatrix} A_-(t) \\ A_+(t) \end{bmatrix}. \tag{1.55}$$

The adiabatic states can serve as a moving coordinate system in which to place the state vector $\Psi(t)$ as it changes under the influence of the coherent radiation pulse. Such coordinates are most useful when the elements of the Hamiltonian – the Rabi frequency and the detuning – change sufficiently slowly (i.e. adiabatically); then the state vector remains fixed in the adiabatic coordinate space. Mathematically, adiabatic evolution requires the off-diagonal elements of the Hamiltonian (1.55) to be negligible compared to the diagonal ones, or

$$\left|\dot{\vartheta}(t)\right| \ll \varepsilon(t)\,, \tag{1.56}$$

which expresses the *adiabatic condition*. According to this condition, adiabatic evolution requires a smooth pulse, long interaction time, and large Rabi frequency and/or large detuning.

When the adiabatic condition holds, there are no transitions between the adiabatic states and their populations are conserved. That is, the state vector remains fixed in the time-varying coordinate system of adiabatic states, as the latter move with respect to the fixed basis states ψ_1 and ψ_2. In particular, if the state vector $\Psi(t)$ coincides with a single adiabatic state at some time t, then it will remain in that adiabatic state as long as the evolution is adiabatic; the state vector $\Psi(t)$ will *adiabatically follow* the state $\Phi(t)$.

1.4 Rapid Adiabatic Passage

Here we present a scheme for complete transfer of atomic or molecular population between two bound states called *rapid adiabatic passage* (RAP), which produces frequency-swept pulses and thus induces a level crossing, which in case of adiabatic limit leads to complete population transfer. In brief, coherent excitation of a two-state quantum system is described by the Schrödinger equation, which in the rotating-wave approximation (RWA) [4] reads

$$i\frac{d}{dt}\mathbf{C}(t) = \hat{H}(t)\mathbf{C}(t), \tag{1.57}$$

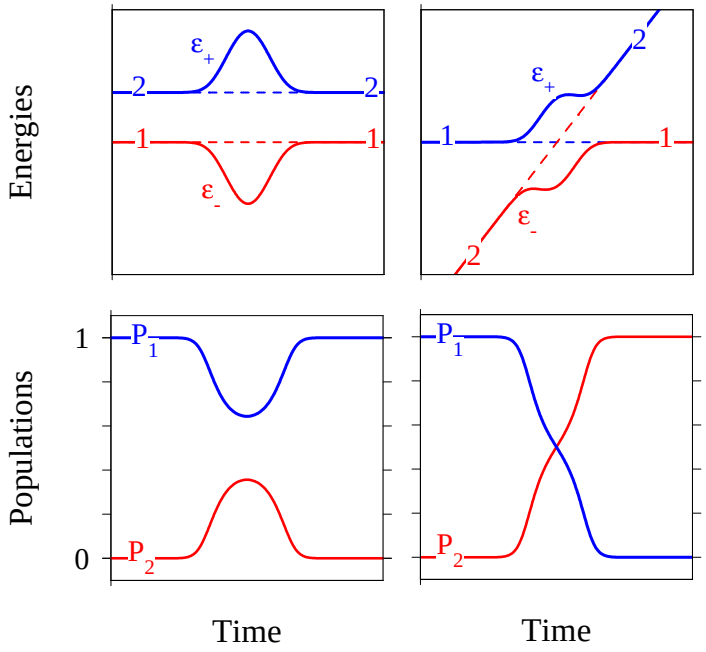

Figure 1.1: Time evolution of the energies (upper frames) and the populations (lower frames) in a two-state system. In the upper plots, the dashed lines show the unperturbed (diabatic) energies, and the solid curves show the adiabatic energies. The left-hand frames are for the no-crossing case, and the right-hand frames are for the level-crossing case.

where $\mathbf{C}(t) = [C_1(t), C_2(t)]^T$ is the column-vector with the probability amplitudes $C_1(t)$ and $C_2(t)$ of the two states ψ_1 and ψ_2, and $\hat{H}(t)$ is the Hamiltonian, [4]

$$\hat{H}(t) = \frac{1}{2}\begin{bmatrix} 0 & \Omega(t) \\ \Omega(t) & 2\Delta(t) \end{bmatrix}. \tag{1.58}$$

Above $\Omega(t)$ is the Rabi frequency and $\Delta(t)$ is detuning. Now to derive the properties of Rapid adiabatic passage (RAP), we consider the adiabatic states $\Phi_{\pm}$. These states are the instantaneous eigenvectors of (1.58)(see also Chapter 2) and can be expressed as coherent superpositions of the bare states ψ_1 and ψ_2 by:

$$\Phi_+(t) = \cos\vartheta(t)\,\psi_1 + \sin\vartheta(t)\,\psi_2, \tag{1.59}$$

$$\Phi_-(t) = \sin\vartheta(t)\,\psi_1 - \cos\vartheta(t)\,\psi_2. \tag{1.60}$$

with the mixing angle $\vartheta(t)$ given by

$$\tan 2\vartheta(t) = \frac{\Omega(t)}{\Delta(t)}. \tag{1.61}$$

There are two distinct types of adiabatic population changes depending on the behavior of the diabatic energies of the Hamiltonians (1.58). The no-crossing case is depicted in Fig. 1.1

(top left frame) in the particular case of constant detuning; the diabatic energies are parallel to each other. In the absence of interaction, the adiabatic energies coincide with the diabatic ones, but the (pulsed) interaction $\Omega(t)$ pushes them away from each other. As Eq. (1.59) and (1.60) show, at early and late times each adiabatic state is identified with the same diabatic state: $\Phi_-(t \to \pm\infty) = \psi_1$, $\Phi_+(t \to \pm\infty) = \psi_2$, whereas at intermediate times it is a superposition of diabatic states. Consequently, starting from the ground state ψ_1, the population makes a partial excursion into the excited state ψ_2 at intermediate times and eventually returns to ψ_1 in the end (bottom left frame). Hence, in the no-crossing case adiabatic evolution leads to complete population return. A rather different situation occurs when the detuning $\Delta(t)$ sweeps slowly from some very large negative value to some very large positive value or vice versa (irrespective of whether the laser frequency or the transition frequency is changed), as shown in Fig. 1.1 (top right frame). Then the angle $\vartheta(t)$ rotates clockwise from 0 to $-\pi/2$ and the adiabatic eigenstate $\Phi_-(t)$ changes from ψ_1 to ψ_2:

$$\Phi_-(-\infty) = \psi_1 \tag{1.62}$$

$$\Phi_-(+\infty) = \psi_2 \tag{1.63}$$

Thus such an adiabatic change (chirp) of $\Delta(t)$ will produce complete population transfer from the initially populated state ψ_1 to the initially unpopulated state ψ_2 Fig. 1.1 (bottom right frame). The process is known as rapid adiabatic passage (RAP) [4].

1.5 The Landau-Zener Model

The time evolution of a coherently driven two-state quantum system is described by the two coupled ordinary differential equations for the probability amplitudes $C_1(t)$ and $C_2(t)$ of states ψ_1 and ψ_2:

$$i\frac{d}{dt}C_1(t) = -\tfrac{1}{2}\Delta(t)C_1(t) + \tfrac{1}{2}\Omega(t)C_2(t), \tag{1.64}$$

$$i\frac{d}{dt}C_2(t) = \tfrac{1}{2}\Omega(t)C_1(t) + \tfrac{1}{2}\Delta(t)C_2(t). \tag{1.65}$$

where $\Omega(t)$ is the coupling (assumed real) between the two states and $\Delta(t)$ is the frequency detuning.

In the Landau-Zener model [1], the coupling and the detuning are given by

$$\Omega(t) = \Omega_0, \qquad \Delta(t) = \beta^2 t. \tag{1.66}$$

In the *original* Landau-Zener model [1], the coupling $\Omega(t)$ is supposed to last from $t \to -\infty$ to $t \to +\infty$. In the finite LZ model [9], the coupling lasts from time t_i until time t_f,

$$\Omega(t) = \begin{cases} \Omega_0, & t_i \le t \le t_f \\ 0, & \text{anywhere else} \end{cases}, \qquad \Delta(t) = \beta^2 t. \tag{1.67}$$

The real constants Ω_0 and β have the dimension of frequency and will be assumed positive without loss of generality. We have chosen the slope β^2 of the detuning at the crossing $t = 0$ to be positive in order to avoid unnecessary complications: the case of $\Delta(t) = -\beta^2 t$ leads to complex conjugation of the evolution matrix and change of sign of the non-diagonal elements.

It is convenient to introduce the dimensionless parameters

$$\tau = \frac{\beta t}{\sqrt{2}}, \qquad \alpha = \frac{\Omega_0}{\sqrt{2}\beta}. \tag{1.68}$$

Hence for the initial and final moment of time

$$\tau_{i,f} = \frac{\beta t_{i,f}}{\sqrt{2}} \tag{1.69}$$

The evolution matrix elements are

$$U_{11}(\tau_f, \tau_i) = \frac{\Gamma(1 - \frac{1}{2}i\alpha^2)}{\sqrt{2\pi}} \left[D_{\frac{1}{2}i\alpha^2}(z_f) D_{-1+\frac{1}{2}i\alpha^2}(-z_i) + D_{\frac{1}{2}i\alpha^2}(-z_f) D_{-1+\frac{1}{2}i\alpha^2}(z_i) \right], \tag{1.70}$$

$$U_{12}(\tau_f, \tau_i) = \frac{\Gamma(1 - \frac{1}{2}i\alpha^2)}{\alpha\sqrt{\pi}} e^{i\frac{\pi}{4}} \left[-D_{\frac{1}{2}i\alpha^2}(z_f) D_{\frac{1}{2}i\alpha^2}(-z_i) + D_{\frac{1}{2}i\alpha^2}(-z_f) D_{\frac{1}{2}i\alpha^2}(z_i) \right], \tag{1.71}$$

where $z = \tau\sqrt{2}e^{-i\frac{\pi}{4}}$. We can find the other evolution-matrix elements using the unitarity of $\mathsf{U}(\tau_f, \tau_i)$ which implies that $U_{22}(\tau_f, \tau_i) = U_{11}^*(\tau_f, \tau_i)$ and $U_{21}(\tau_f, \tau_i) = -U_{12}^*(\tau_f, \tau_i)$.

If the system has initially been in state ψ_1, i.e.

$$C_1(\tau_i) = 1, \qquad C_2(\tau_i) = 0, \tag{1.72}$$

the populations at time τ_f are given by $P_1(\tau_f, \tau_i) = |U_{11}(\tau_f, \tau_i)|^2$, $P_2(\tau_f, \tau_i) = |U_{21}(\tau_f, \tau_i)|^2$ with $P_1(\tau_f, \tau_i) + P_2(\tau_f, \tau_i) = 1$. The transition probability is

$$P_2(\tau_f, \tau_i) = \frac{1}{2\sinh\frac{1}{2}\pi\alpha^2} \left| -D_{\frac{1}{2}i\alpha^2}(z_f) D_{\frac{1}{2}i\alpha^2}(-z_i) + D_{\frac{1}{2}i\alpha^2}(-z_f) D_{\frac{1}{2}i\alpha^2}(z_i) \right|^2. \tag{1.73}$$

For the original LZ model we have

$$U_{11}(+\infty, -\infty) = e^{-\frac{1}{2}\pi\alpha^2},$$

$$U_{12}(+\infty, -\infty) = -\sqrt{1 - e^{-\pi\alpha^2}} \exp\left\{ i \left[\frac{1}{2}(\tau_i^2 + \tau_f^2) + \frac{1}{4}\alpha^2 \ln 4\tau_i^2\tau_f^2 + \frac{\pi}{4} + \arg\Gamma(1 - \frac{1}{2}i\alpha^2) \right] \right\}$$

The populations are

$$P_1(+\infty) = |U_{11}(+\infty, -\infty)|^2 = e^{-\pi\alpha^2}, \tag{1.74}$$

$$P_2(+\infty) = |U_{12}(+\infty, -\infty)|^2 = 1 - e^{-\pi\alpha^2}. \tag{1.75}$$

Chapter 2

Steering Quantum Transitions Between Three Crossing Energy Levels

In this chapter we calculate the propagator and the transition probabilities for a coherently driven quantum system with three-states, whose energies change linearly in time. We derive a highly accurate analytic approximation based on the two state Landau-Zener model, which is the most popular tool for estimating the transition probability between two states with crossing energies.

2.1 Definition of the Problem

2.1.1 Description of the System

We consider a three-state system driven coherently by a pulsed external field, with the rotating-wave approximation (RWA) Hamiltonian (in units $\hbar = 1$)

$$\hat{H}(t) = \begin{bmatrix} \Delta_0 + At & \frac{1}{2}\Omega_{12}(t) & 0 \\ \frac{1}{2}\Omega_{12}(t) & 0 & \frac{1}{2}\Omega_{23}(t) \\ 0 & \frac{1}{2}\Omega_{23}(t) & \Delta_0 - At \end{bmatrix}. \tag{2.1}$$

The diagonal elements are the (diabatic) energies (in units $\hbar$) of the three states, the second of which is taken as the zero reference point without loss of generality. Δ_0 is a static detuning, and $\pm At$ are the linearly changing terms. To be specific, we shall use the language of laser-atom interactions, where the difference between each pair of diagonal elements is the detuning for the respective transition: the offset of the laser carrier frequency from the Bohr transition frequency.

The pulse-shaped functions $\Omega_{12}(t)$ and $\Omega_{23}(t)$ are the Rabi frequencies, which quantify the field-induced interactions between each pair of adjacent states, $\psi_1 \leftrightarrow \psi_2$ and $\psi_2 \leftrightarrow \psi_3$, respectively. Each of the Rabi frequencies is proportional to the respective transition dipole moment and the laser electric-field envelope. As evident from the zeroes in the corners of the Hamiltonian (2.1) we assume that the direct transition $\psi_1 \leftrightarrow \psi_3$ is forbidden, as it occurs in free atoms when $\psi_1 \leftrightarrow \psi_2$ and $\psi_2 \leftrightarrow \psi_3$ are electric-dipole transitions.

The probability amplitudes of our system $\mathbf{C}(t) = [C_1(t), C_2(t), C_3(t)]^T$ satisfy the Schrödinger equation

$$i\dot{\mathbf{C}}(t) = \hat{H}(t)\mathbf{C}(t), \tag{2.2}$$

where the overdot denotes a time derivative.

Without loss of generality, the couplings $\Omega_{12}(t)$ and $\Omega_{23}(t)$ are assumed real and positive and, for the sake of simplicity, with the same time dependence. For the time being the detuning Δ_0 and the slope A are assumed to be also positive,

$$\Delta_0 > 0 \ , \quad A > 0; \tag{2.3}$$

we shall consider the cases of negative Δ_0 and A later on. With the assumptions above, the crossing between the diabatic energies of states ψ_1 and ψ_2 occurs at time $t_- = -\tau$, where $\tau = \Delta_0/A$, between ψ_2 and ψ_3 at time $t_+ = \tau$, and the one between ψ_1 and ψ_3 at time $t_0 = 0$.

Fig. 2.1 plots diabatic and adiabatic energies vs time for a Gaussian-shaped laser pulse. We use ψ_k and χ_k to denote diabatic and adiabatic states, respectively.

The objective of this paper is to find analytical expressions for the evolution matrix and for the transition probabilities between different diabatic states.

2.1.2 Implementation

The Hamiltonian (2.1) appears naturally in a number of specific problems of interest in time-dependent quantum dynamics of simple systems.

The first example is ladder climbing of electronic energy states in some alkali atoms, for instance, in rubidium [10]. A linearly chirped laser pulse couples simultaneously both transitions 5s-5p and 5p-6s. If the carrier frequency of the pulse is tuned on two-photon resonance with the 5s-6s transition, then the intermediate state 5p remains off resonance, by a detuning Δ, which leads to the "triangle" linkage pattern in Fig. 2.1. The couplings $\Omega_{12}(t)$ and $\Omega_{23}(t)$ are the Rabi frequencies of the two transitions, which may be different (because of the different transition dipole moments) but have the same time dependence since they are induced by the same laser pulse.

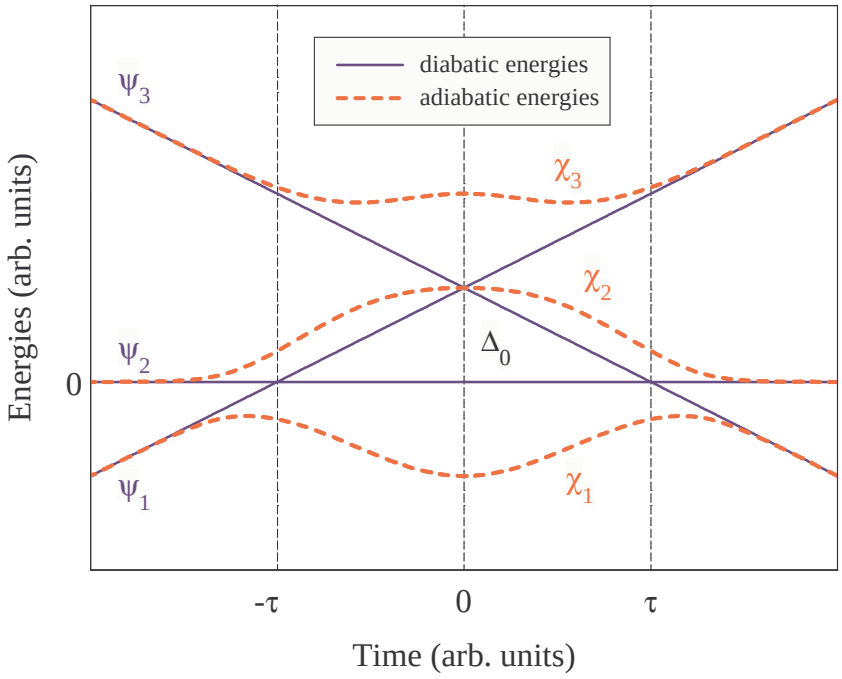

Figure 2.1: Diabatic and adiabatic energies vs time for a Gaussian-shaped laser pulse. The labels denote the respective diabatic and adiabatic states.

A second example is found in rf transitions between the three magnetic sublevels $m = -1, 0, 1$ of a level with an angular momentum $J = 1$ in an atom trapped in a magnetooptical trap. The rf pulse provides the pulsed coupling between the $m = -1$ and $m = 0$ sublevels, and also between the $m = 0$ and $m = 1$ sublevels. The trapping magnetic field causes Zeeman shifts in the magnetic sublevels $m = -1$ and 1 in different directions but it does not affect the $m = 0$ level [11]. This linkage pattern is an example of a bowtie level crossing [12–15]. If a quadratic Zeeman shift is taken into account, then the sublevels $m = -1$ and 1 will be shifted in the same direction, which will break the symmetry of the bowtie linkage and will create the "triangle"pattern of Fig. 2.1.

A third example is found in quantum rotors, for instance, in rotational ladder climbing in molecules by using a pair of chirped ultrashort laser pulses [16]. The energy slope is due to the laser chirp, and the static detuning Δ_0 arises due to the rotational energy splitting. If the laser pulse duration is chosen appropriately then only three rotational states will be coupled, with their energies forming the "triangle" pattern of Fig. 2.1.

The fourth example is the entanglement between two spin-1/2 particles interacting with two crossed magnetic fields, a linear field along one axis and a pulsed field along another axis [17]. The role of the static detuning Δ_0 is played by the spin-spin coupling constant. Three of the four collective states form a chain, which has exactly the "triangle" linkage pattern of Fig. 2.1.

In this system, states ψ_1 and ψ_3 correspond to the product states $|\downarrow\rangle|\downarrow\rangle$ and $|\uparrow\rangle|\uparrow\rangle$, whereas state ψ_2 is the entangled state $(|\downarrow\rangle|\uparrow\rangle + |\uparrow\rangle|\downarrow\rangle)/\sqrt{2}$.

2.2 Evolution Matrix

An exact solution of the Schrödinger equation (2.2) for the Hamiltonian (2.1) is not known. We shall derive an approximation, which is most conveniently obtained in the adiabatic basis.

2.2.1 Adiabatic Picture

The adiabatic states are defined as the eigenvectors $\chi_k(t)$ $(k = 1, 2, 3)$ of the instantaneous Hamiltonian $\hat{H}(t)$. The corresponding adiabatic amplitudes $\mathbf{A}(t) = [A_1(t), A_2(t), A_3(t)]^T$ and the diabatic ones $\mathbf{C}(t)$ are related as

$$\mathbf{C}(t) = \hat{R}(t)\mathbf{A}(t), \tag{2.4}$$

where $\hat{R}(t)$ is an orthogonal (because $\hat{H}(t)$ is real) transformation matrix, $\hat{R}^{-1}(t) = \hat{R}^T(t)$, whose columns are the adiabatic states χ_k $(k = 1, 2, 3)$, with χ_1 having the lowest energy and χ_3 the highest energy. As we are only interested in the populations at infinite times, we need only $\hat{R}(\pm\infty)$, rather than the explicit function $\hat{R}(t)$. $\hat{R}(\pm\infty)$ can be easily obtained using the asymptotic behavior of $\hat{H}(t)$ at infinite times,

$$\hat{R}(-\infty) = \begin{bmatrix} 1 & 0 & 0 \\ 0 & 1 & 0 \\ 0 & 0 & 1 \end{bmatrix}, \quad \hat{R}(+\infty) = \begin{bmatrix} 0 & 0 & 1 \\ 0 & 1 & 0 \\ 1 & 0 & 0 \end{bmatrix}. \tag{2.5}$$

The Schrödinger equation in adiabatic basis reads

$$i\dot{\mathbf{A}}(t) = \hat{H}_A(t)\mathbf{A}(t), \tag{2.6}$$

with $\hat{H}_A(t) = \hat{R}^T(t)\hat{H}(t)\hat{R}(t) - i\hat{R}^T(t)\dot{\hat{R}}(t)$, or

$$\hat{H}_A(t) = \begin{bmatrix} \lambda_1(t) & -i\nu_{12}(t) & -i\nu_{13}(t) \\ -i\nu_{21}(t) & \lambda_2(t) & -i\nu_{23}(t) \\ -i\nu_{31}(t) & -i\nu_{32}(t) & \lambda_3(t) \end{bmatrix}, \tag{2.7}$$

where the nonadiabatic coupling between the adiabatic states $\chi_k(t)$ and $\chi_l(t)$ is

$$\nu_{kl}(t) = \langle \chi_k(t) | \dot{\chi}_l(t) \rangle = -\nu_{lk}(t). \tag{2.8}$$

2.2.2 Assumptions

Our approach is based on two simplifying assumptions. First, we assume that appreciable transitions take place only between neighboring adiabatic states, $\chi_1(t) \leftrightarrow \chi_2(t)$ and $\chi_2(t) \leftrightarrow \chi_3(t)$, but not between states $\chi_1(t)$ and $\chi_3(t)$, because the energies of the latter pair are split by the largest gap (cf. Fig. 2.1). Second, we assume that the nonadiabatic transitions occur instantly at the corresponding avoided crossings and the evolution is adiabatic elsewhere. This allows us to obtain the evolution matrix in the adiabatic basis by multiplying seven evolution matrices describing either LZ nonadiabatic transitions or adiabatic evolution.

2.2.3 Evolution Matrix in the Adiabatic Basis

The adiabatic evolution matrix $\hat{U}^A(\infty, -\infty)$ is most conveniently determined in the adiabatic interaction representation, where the diagonal elements of $\hat{H}_A(t)$ are nullified. The transformation to this basis reads

$$\mathbf{A}(t) = \hat{M}(t, t_0)\mathbf{B}(t), \tag{2.9}$$

where

$$\hat{M}(t, t_0) = \begin{bmatrix} e^{-i\Lambda_1(t,t_0)} & 0 & 0 \\ 0 & e^{-i\Lambda_2(t,t_0)} & 0 \\ 0 & 0 & e^{-i\Lambda_3(t,t_0)} \end{bmatrix}, \tag{2.10a}$$

$$\Lambda_k(t, t_0) = \int_{t_0}^{t} \lambda_k(t')dt', \tag{2.10b}$$

and t_0 is an arbitrary fixed time. The Schrödinger equation in this basis reads

$$i\dot{\mathbf{B}}(t) = \hat{H}_B(t)\mathbf{B}(t), \tag{2.11}$$

with

$$\hat{H}_B(t) = -i \begin{bmatrix} 0 & \nu_{12}e^{i\Lambda_{12}(t,t_0)} & \nu_{13}e^{i\Lambda_{13}(t,t_0)} \\ \nu_{21}e^{i\Lambda_{21}(t,t_0)} & 0 & \nu_{23}e^{i\Lambda_{23}(t,t_0)} \\ \nu_{31}e^{i\Lambda_{31}(t,t_0)} & \nu_{32}e^{i\Lambda_{32}(t,t_0)} & 0 \end{bmatrix}, \tag{2.12}$$

where $\Lambda_{kl}(t, t_0) \equiv \Lambda_k(t, t_0) - \Lambda_l(t, t_0)$. In this basis the propagator for adiabatic evolution is the identity matrix.

The LZ transitions at the crossings at times $-\tau, 0, \tau$ are described by the transition matrices

[18]

$$\hat{U}_{LZ}(-\tau) = \begin{bmatrix} \sqrt{q_-}e^{-i\phi_-} & -\sqrt{p_-} & 0 \\ \sqrt{p_-} & \sqrt{q_-}e^{i\phi_-} & 0 \\ 0 & 0 & 1 \end{bmatrix}, \tag{2.13a}$$

$$\hat{U}_{LZ}(0) = \begin{bmatrix} 1 & 0 & 0 \\ 0 & \sqrt{q_0}e^{-i\phi_0} & -\sqrt{p_0} \\ 0 & \sqrt{p_0} & \sqrt{q_0}e^{i\phi_0} \end{bmatrix}, \tag{2.13b}$$

$$\hat{U}_{LZ}(\tau) = \begin{bmatrix} \sqrt{q_+}e^{-i\phi_+} & -\sqrt{p_+} & 0 \\ \sqrt{p_+} & \sqrt{q_+}e^{i\phi_+} & 0 \\ 0 & 0 & 1 \end{bmatrix}, \tag{2.13c}$$

where $p_\varkappa$ ($\varkappa = -, 0, +$) is the LZ probability of nonadiabatic transition and $q_\varkappa$ is the no-transition probability at the crossings at times $-\tau, 0, \tau$,

$$p_\varkappa = e^{-\pi a_\varkappa^2}, \quad q_\varkappa = 1 - p_\varkappa. \tag{2.14}$$

Here

$$a_- = \Omega_{12}(-\tau)/(2A)^{1/2}, \tag{2.15a}$$

$$a_0 = \Omega_{eff}(0)/2A^{1/2}, \tag{2.15b}$$

$$a_+ = \Omega_{23}(\tau)/(2A)^{1/2}, \tag{2.15c}$$

$$\phi_\varkappa = \arg\,\Gamma(1 - ia_\varkappa^2) + \frac{\pi}{4} + a_\varkappa^2(\ln a_\varkappa^2 - 1), \tag{2.15d}$$

where $\Omega_{eff}(0)$ is the effective coupling between states ψ_1 and ψ_3 at crossing time $t = 0$; it is determined by the splitting between the adiabatic curves $\lambda_2(t)$ and $\lambda_3(t)$,

$$\Omega_{eff}(0) = \lambda_2(0) - \lambda_3(0) = \frac{1}{2}\left(-\Delta_0 + \sqrt{\Delta_0^2 + 2\Omega_0^2}\right). \tag{2.16}$$

The propagator in the adiabatic basis reads

$$\begin{aligned} \hat{U}^A(\infty, -\infty) = \hat{M}(\infty, \tau)\hat{U}_{LZ}(\tau)\hat{M}(\tau, 0)\hat{U}_{LZ}(0) \\ \times \hat{M}(0, -\tau)\hat{U}_{LZ}(-\tau)\hat{M}(-\tau, -\infty). \end{aligned} \tag{2.17}$$

2.2.4 Propagator and Transition Probabilities in the Diabatic Basis

Below we present the diabatic propagator in an explicit form. For simplicity, we assume equal couplings

$$\Omega_{12}(t) = \Omega_{23}(t) = \Omega(t), \tag{2.18}$$

although our approach is valid in the general case. This constraint is not applicable for the ladder climbing system, considered in Sec. 2.1.2, where the couplings are naturally different due to the different transition dipole moments, but is still valid for the other systems discussed. Then $\Lambda_{kl}(0,-t) = \Lambda_{kl}(t,0)$, $a_+ = a_- = a$, $\phi_+ = \phi_- = \phi$, $p_+ = p_- = p$, and $q_+ = q_- = q$.

We find the propagator in the original diabatic basis by using Eqs. (2.4), (2.5) and (2.17) as $\hat{U}(\infty,-\infty) = \hat{R}(\infty)\hat{U}^A(\infty,-\infty)\hat{R}^T(-\infty)$, or explicitly,

$$\hat{U}(\infty,-\infty) = \begin{bmatrix} e^{i\varphi_1+i\varphi_3}\sqrt{pp_0} & e^{i\phi+i\varphi_2+i\varphi_3}\sqrt{qp_0} & e^{i\phi_0+2i\varphi_3}\sqrt{q_0} \\ e^{-i\phi-i\varphi_1+i\varphi_2}\sqrt{pq} + e^{i\phi-i\phi_0+i\varphi_1+i\varphi_2}\sqrt{pqq_0} & -e^{-2i\varphi_1+2i\varphi_2}p + e^{2i\phi-i\varphi_0+2i\varphi_2}q\sqrt{q_0} & -e^{i\phi+i\varphi_2+i\varphi_3}\sqrt{qp_0} \\ e^{-2i\phi}q - e^{-i\phi_0+2i\varphi_1}p\sqrt{q_0} & -e^{-i\phi-i\varphi_1+i\varphi_2}\sqrt{pq} - e^{i\phi-i\phi_0+i\varphi_1+i\varphi_2}\sqrt{pqq_0} & e^{i\varphi_1+i\varphi_3}\sqrt{pp_0} \end{bmatrix} \tag{2.19}$$

with $\varphi_1 = \Lambda_{12}(\tau,0)$, $\varphi_2 = \Lambda_{12}(\infty,0)$, $\varphi_3 = \Lambda_{13}(\infty,0)$. The transition probability matrix, i.e. the matrix of the absolute squares of the elements of the propagator (2.19), reads

$$\mathbf{P} = \begin{bmatrix} pp_0 & qp_0 & q_0 \\ qp + pq_0q + 2qp\sqrt{q_0}\cos\gamma & p^2 + q^2q_0 - 2qp\sqrt{q_0}\cos\gamma & qp_0 \\ q^2 + q_0p^2 - 2qp\sqrt{q_0}\cos\gamma & qp + pq_0q + 2qp\sqrt{q_0}\cos\gamma & pp_0 \end{bmatrix}, \tag{2.20}$$

where

$$\gamma = 2\phi - \phi_0 + 2\varphi_1. \tag{2.21}$$

The element at the m-th row and the n-th column of the matrix (2.20) is the transition probability $P_{n\to m}$, that is the population of state m at infinite time, when the system starts in state n in the infinite past. The survival probabilities $P_{1\to1}$ and $P_{3\to3}$ coincide with the exact expressions conjectured [15] and derived exactly for constant couplings [19, 20] earlier.

In Eq. (2.20) we recognize interference terms, which arise because of the availability of two alternative propagating paths in the Hilbert space. There is also a symmetry with respect to the skew diagonal due to the equal couplings between neighboring states (2.18) and the equal (in magnitude) slopes of the energies of states ψ_1 and ψ_3 (2.1).

2.2.5 Conditions of Validity

As already stressed, our approach presumes that the nonadiabatic transitions occur in well-separated confined time intervals. This means that the characteristic transition times are shorter than the times between the crossings, or $t_{transition} \lesssim \tau$. The transition times for diabatic

($\Omega^2 \ll A$) and adiabatic ($\Omega^2 \gg A$) regimes are [21]

$$t_{transition} \approx \sqrt{2\pi/A}, \quad \text{diabatic regime,} \tag{2.22a}$$

$$t_{transition} \approx 2\Omega/A, \quad \text{adiabatic regime.} \tag{2.22b}$$

This leads to the following conditions for validity:

$$\Delta_0 \gtrsim \sqrt{2\pi A}, \quad \text{diabatic regime,} \tag{2.23a}$$

$$\Delta_0 \gtrsim 2\Omega, \quad \text{adiabatic regime.} \tag{2.23b}$$

We shall demonstrate that the LZ-based approximation (2.20) outperforms its formal conditions of validity (2.23) and is valid beyond the respective ranges.

2.2.6 Case of $\Delta_0 < 0$ and/or $A < 0$

Above we assumed that $\Delta_0 > 0$ and $A > 0$. Now we consider the cases $\Delta_0 < 0$ and $A < 0$. We assume that the couplings are even functions, $\Omega(-t) = \Omega(t)$.

Negative static detuning ($\Delta_0 < 0$).

The Schrödinger equation for the propagator $\hat{U}(\Delta_0; t, t_i)$ is

$$i\frac{\partial}{\partial t}\hat{U}(\Delta_0; t, t_i) = \hat{H}(\Delta_0, t)\hat{U}(\Delta_0; t, t_i). \tag{2.24}$$

By changing the signs of Δ_0, t and t_i in Eq (2.24), we obtain the same equation, but with the $\Omega(t)$ replaced by $-\Omega(t)$ [see Eq. (2.1)]. It is easy to see that the change of sign of $\Omega(t)$ is equivalent to the transformation $\hat{U} \to \hat{U}' = \mathbf{Q}\hat{U}\mathbf{Q}$ where $\mathbf{Q}$ is the diagonal matrix $\mathbf{Q} = \mathrm{diag}\{1, -1, 1\}$. Hence we find

$$i\frac{\partial}{\partial t}\hat{U}'(-\Delta_0; -t, -t_i) = \hat{H}(\Delta_0, t)\hat{U}'(-\Delta_0; -t, -t_i). \tag{2.25}$$

Because the initial condition at $t \to -\infty$ for $\hat{U}(\Delta_0; t, t_i)$ and $\hat{U}'(-\Delta_0; -t, -t_i)$ at $t \to -\infty$ is the same,

$$\hat{U}(\Delta_0; -\infty, -\infty) = \hat{U}'(-\Delta_0; \infty, \infty) = \mathbf{I}, \tag{2.26}$$

we conclude that $\hat{U}(\Delta_0; t, t_i) = \hat{U}'(-\Delta_0; -t, -t_i)$; hence

$$\begin{aligned} \hat{U}(-\Delta_0; \infty, -\infty) &= \mathbf{Q}\hat{U}(\Delta_0; -\infty, \infty)\mathbf{Q} \\ &= \mathbf{Q}\hat{U}(\Delta_0; \infty, -\infty)^{\dagger}\mathbf{Q}. \end{aligned} \tag{2.27}$$

Therefore

$$P_{m\to n}(-\Delta_0) = P_{n\to m}(\Delta_0), \quad (m, n = 1, 2, 3). \tag{2.28}$$

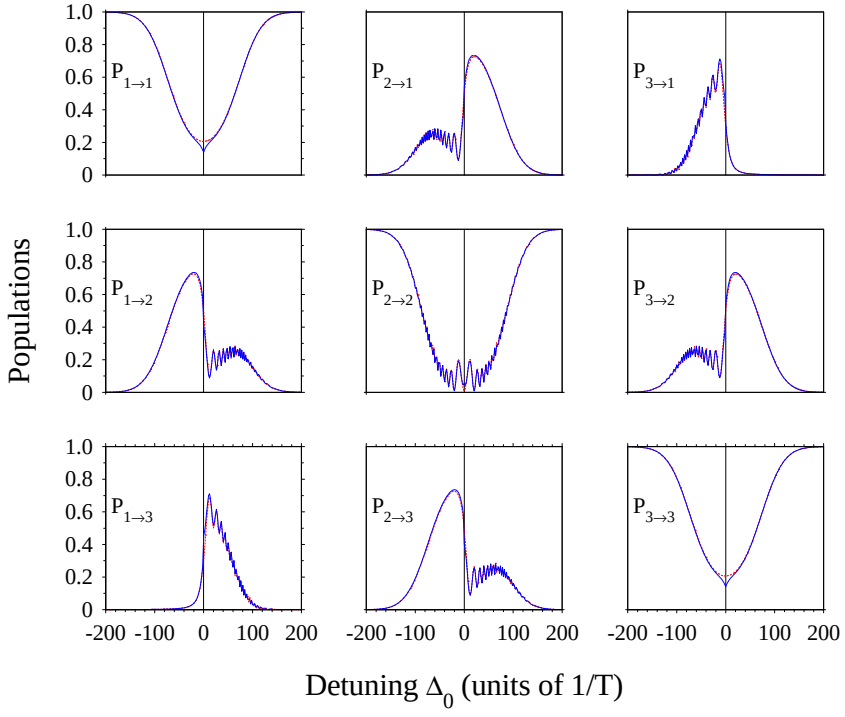

Figure 2.2: The transition probabilities $P_{m\to n}$ for the transition $m \to n$ vs the detuning Δ_0 for $A = 100/T^2$, $\Omega_0 = 10/T$. Each frame compares the numerical (dashed red) and analytical (solid blue) results.

Negative chirp rate ($A < 0$).

We notice that $H_{11}(A) = H_{33}(-A)$, i.e. the change of sign of A is equivalent to exchanging the indices 1 and 3. Hence the probabilities for $A < 0$ are obtained from these for $A > 0$ using the relation

$$P_{m\to n}(-A) = P_{4-m\to 4-n}(A), \quad (m, n = 1, 2, 3)\,. \tag{2.29}$$

2.3 Comparison of Analytical and Numerical Results

Below we compare our analytical approximation with numerical simulations. We take for definiteness the couplings in Eq. (2.1) to be Gaussians, $\Omega(t) = \Omega_0 e^{-t^2/T^2}$.

Figure 2.2 shows the nine transition probabilities vs the static detuning Δ_0. An excellent agreement is observed between analytics and numerics, which are barely discernible. This agreement indicates that the dynamics is indeed driven by separated level-crossing transitions of LZ type. The analytic approximation (2.20) is clearly valid beyond its formal range of validity, defined by conditions (2.23), which suggest $|\Delta_0| \gtrsim 25/T$ for the parameters in this figure. The figure also demonstrates that the detuning can be used as a control parameter for

the probabilities in wide ranges.

For $\Delta_0 > 0$ the five probabilities on the first row and the last column vary smoothly, in agreement with the analytic prediction. The two-photon probability $P_{3\to1}$ vanishes rapidly with Δ_0, as expected, at a much faster pace than the other probabilities. The other four probabilities $P_{1\to2}$, $P_{1\to3}$, $P_{2\to2}$ and $P_{2\to3}$ exhibit oscillations, in agreement with the analytic prediction, due to the existence of two alternative paths of different length from the initial to the final state (see Fig. 2.1), with an ensuing interference. It is noteworthy that these oscillations, due to path interference, are not particularly pronounced, which might be a little surprising at first glance. However, a more careful analysis reveals that when a control parameter is varied, such as the static detuning Δ_0 here, it changes not only the relative phase along the two paths (which causes the oscillations), but also the LZ probabilities $p_\varkappa$ and $q_\varkappa$ ($\varkappa = -, 0, +$). Indeed, as Δ_0 increases, we have $p_\pm \to 1$ because the crossings at times $\pm\tau$ move away from the center of the pulses and $\Omega(\pm\tau) \to 0$. These probabilities affect both the average value of $P_{m\to n}$ and the oscillation amplitude, with $P_{m\to n}$ tending eventually to either 0 or 1 for large Δ_0, while the oscillation amplitude (which is proportional to $p_\pm$) is damped.

Similar conclusions apply to the case of $\Delta_0 < 0$ because of the symmetry property (2.28). It is easy to see from here that the survival probabilities $P_{n\to n}$ ($n = 1, 2, 3$) are symmetric vs Δ_0, as indeed seen in Fig. 2.2.

Figure 2.3 displays the transition probabilities vs the chirp rate A. An excellent agreement is again observed between analytics and numerics. We have verified that the analytic approximation (2.20) is valid well beyond its formal range of validity conditions (2.23), which suggest $|A| \lesssim 140/T^2$ for this figure; this is not shown because our intention here is to show the small-A range that exhibits interference patterns. As with the static detuning in Fig. 2.2, this figure demonstrates the symmetry with respect to the sign inversion of A, derived in Eq. (2.29): the change $A \to -A$ is equivalent to the exchange of the indices 1 and 3. The observed additional symmetry, $P_{2\to1} \equiv P_{3\to2}$ and $P_{1\to2} \equiv P_{2\to3}$, is a consequence from the assumptions of equal Rabi frequencies and equal (in magnitude) slopes of the energies of states ψ_1 and ψ_3. The figure also shows that, with the exception of the survival probabilities $P_{n\to n}$ ($n = 1, 2, 3$), all other probabilities are asymmetric vs the chirp rate A, unlike the two-state level-crossing case. For $A > 0$, as for $\Delta_0 > 0$ in Fig. 2.2, oscillations are observed in the four probabilities in the lower left corner but not for the probabilities in the top row and the right column. On the contrary, for $A < 0$, oscillations are observed only in the four probabilities in the top right corner. As discussed in regard to Fig. 2.2, the observation of these oscillations is in full agreement with their interpretation as resulting from interference between two different evolution paths to the

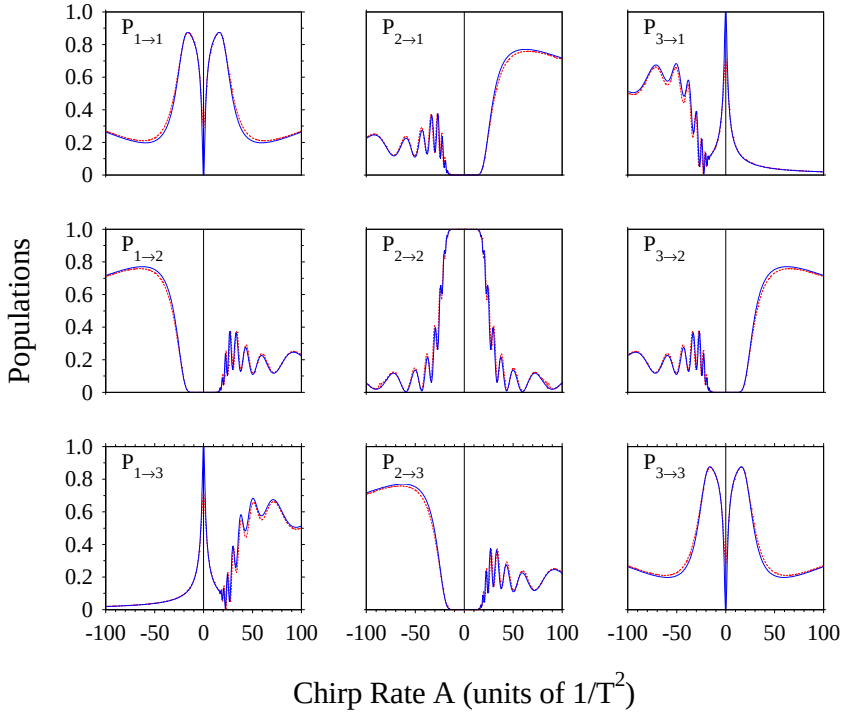

Figure 2.3: The transition probabilities $P_{m\to n}$ for the transition $m \to n$ vs the energy slope A for $\Delta_0 = 30/T$, $\Omega_0 = 10/T$. Each frame compares the numerical (dashed red) and analytical (solid blue) results.

relevant final state.

Like the static detuning Δ_0, the energy slope A can be used as a control parameter because it affects the probabilities considerably. Around the origin ($A = 0$) the system is in adiabatic regime, while for large $|A|$ it is in diabatic regime. For instance, when the system is initially in ψ_1, around the origin ($A = 0$) the population flows mostly into state ψ_3, following the adiabatic state $\chi_1(t)$. On the contrary, for large A it eventually returns to ψ_1 (not visible for the chirp range in Fig. 2.3).

Diabatic and adiabatic regimes are easy to identify also in Fig. 2.4, where the nine probabilities are plotted vs the peak Rabi frequency Ω_0, which is another control parameter. Consider our system initially prepared in state ψ_1. For weak couplings the system evolves diabatically and therefore it is most likely to end up in the same state ψ_1. As the couplings increase, the system switches gradually from diabatic to adiabatic evolution; for strong couplings the evolution proceeds along the adiabatic state $\chi_1(t)$, and we observe nearly complete population transfer to state ψ_3.

Returning to the issue of oscillations, such are barely seen in Fig. 2.4. As discussed in relation to Fig. 2.2, a varying control parameter changes, besides the relative phase of the

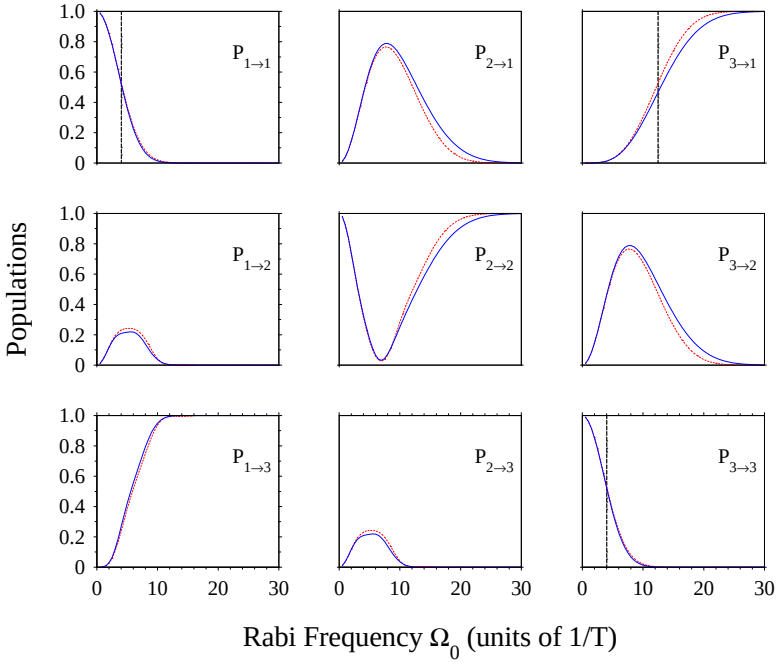

Figure 2.4: The transition probabilities $P_{m\to n}$ for the transition $m \to n$ vs the Rabi frequency Ω_0 for $\Delta_0 = 10/T,\ A = 30/T^2$. Each frame compares the numerical (dashed red) and analytical (solid blue) results. The vertical dashed lines for $P_{1\to1}$, $P_{3\to3}$ and $P_{3\to1}$ show the values $\Omega_{1/2}$ of the Rabi frequency for half population in the relevant states, predicted by our model, Eqs. (2.30) and (2.31).

interfering paths, also the probabilities $p_\varkappa$ and $q_\varkappa$, which eventually acquire their asymptotic values of 0 or 1; in these limits the oscillations vanish. The probabilities depend on the peak Rabi frequency Ω_0 much more sensitively than on the static detuning Δ_0 and the energy slope A; consequently, clear oscillations are seen vs Δ_0 and A, but not vs Ω_0, because the dependence of $p_\varkappa$ on Ω_0 is strongest (essentially Gaussian), and hence the approach to the asymptotic values of the probabilities is fastest.

2.4 Applications of Analytics

In this section we shall use our analytic approximation for the transition probabilities (2.20) to derive several useful properties of the triple-crossing system.

2.4.1 Analytical Linewidth

We begin by deriving approximate expressions for the Rabi frequency required to reach 50% population in the n-th state for the transition $m \to n$. Simple expressions are found for the

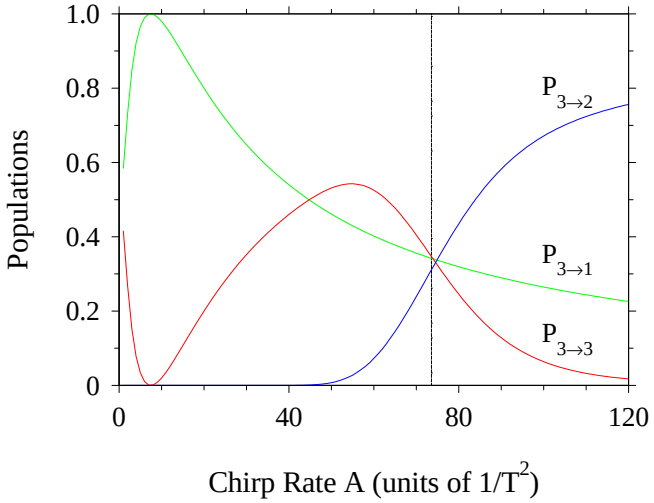

Figure 2.5: The final populations of states ψ_1, ψ_2 and ψ_3 vs the chirp rate A for fixed $\Delta_0 = 100/T$ and $\Omega_0 = 36.2/T$, provided the system is initially in state ψ_3. The three curves cross at about $A \approx 74.5/T^2$, indicating the creation of a maximally coherent superposition with populations $P_1 = P_2 = P_3 = 1/3$, which is very close to the solution of Eqs. (2.32a) and (2.32b), $A = 73.6/T^2$, shown with a vertical dashed line.

transition $3 \to 1$,

$$\Omega_{1/2} = 2\sqrt{\frac{2A\ln 2 + \Delta_0\sqrt{\pi A \ln 2}}{\pi}}, \tag{2.30}$$

and for the transitions $1 \to 1$ and $3 \to 3$,

$$\begin{aligned}\Omega_{1/2} \;=\; & \frac{2}{(\alpha+4)}\left[\frac{2A\alpha(\alpha+4)\ln 2}{\pi} - \alpha\Delta_0^2\right. \\ & \left. +\alpha\Delta_0\sqrt{\Delta_0^2 + \frac{A\alpha(\alpha+4)\ln 2}{\pi}}\right]^{\frac{1}{2}},\end{aligned} \tag{2.31}$$

where $\alpha = \exp(2\Delta_0^2/A^2)$. These values are indicated by vertical lines in Fig. 2.4 and are seen to be in excellent agreement with the exact values.

2.4.2 Creation of Superpositions

If we prepare our system initially in state ψ_1 and use $A < 0$, or in state ψ_3 and use $A > 0$, it is possible to determine by means of our analytical model values of Δ_0, A and Ω_0, so that we achieve arbitrary preselected populations at the end. For example, for a maximally coherent superposition state, i.e. $P_1 = P_2 = P_3 = \frac{1}{3}$, we need $p = \frac{1}{2}$ and $p_0 = \frac{2}{3}$. This yields the following

set of equations for Δ_0, Ω_0, and A:

$$\tfrac{1}{2}e^{2\Delta_0^2/A^2}\ln 2 - \Delta_0\sqrt{\tfrac{\pi \ln 3/2}{A}} - 2\ln 3/2 = 0, \tag{2.32a}$$

$$\Omega_0 = \sqrt{\tfrac{2A\ln 2}{\pi}}e^{\Delta_0^2/A^2}. \tag{2.32b}$$

An example is shown in Fig. 2.5 where the three final probabilities $P_{3\to 1}$, $P_{3\to 2}$ and $P_{3\to 3}$ are plotted versus the chirp rate A. The three probabilities cross (indicating the creation of a maximally coherent superposition state) approximately at the value predicted by Eqs. (2.32a) and (2.32b), shown by the vertical line.

2.5 Comparison with the Exactly Soluble Carroll-Hioe Model for $\Delta_0 = 0$

For $\Delta_0 = 0$ and constant couplings, the Hamiltonian (2.1) allows for an exact solution – this is the Carroll-Hioe (CH) bowtie model [12]. The transition probability matrix for the CH model reads

$$\mathbf{P}_{CH} = \begin{bmatrix} p_c^2 & 2p_c(1-p_c) & (1-p_c)^2 \\ 2p_c(1-p_c) & (1-2p_c)^2 & 2p_c(1-p_c) \\ (1-p_c)^2 & 2p_c(1-p_c) & p_c^2 \end{bmatrix}, \tag{2.33}$$

where

$$p_c = e^{-\pi a^2/2}, \quad a = \Omega/\sqrt{2A}. \tag{2.34}$$

We use this exact result as a reference for the $\Delta_0 = 0$ limit of our approximate method, applied for constant coupling $\Omega(t) = \Omega = const$. We emphasize that taking this limit is an abuse of the method because in the derivation we have assumed that the crossings are *separated*, which has justified the multiplication of propagators. Nonetheless, it is curious and instructive to push our approximation to this limit. For $\Delta_0 = 0$ the LZ parameters are $a_\pm = \Omega/\sqrt{2A} = a$ and $a_0 = a/2$. Therefore we have $p_0^4 = p_c^2 = p$.

Figure 2.6 presents a comparison between the exact Carroll-Hioe solution (2.33) and our approximate solution (2.20). Quite astonishingly, our approximate solution is not only qualitatively correct but it is even in a very good quantitative agreement with the exact solution; we witness here yet another LZ surprise where our LZ-based model outperforms expectations in a limit where it should not be adequate.

The observed feature of our approximate solution can be explained by examining the asymptotics of the approximate probabilities (2.20) and the exact CH values (2.33) for $a \ll 1$ and

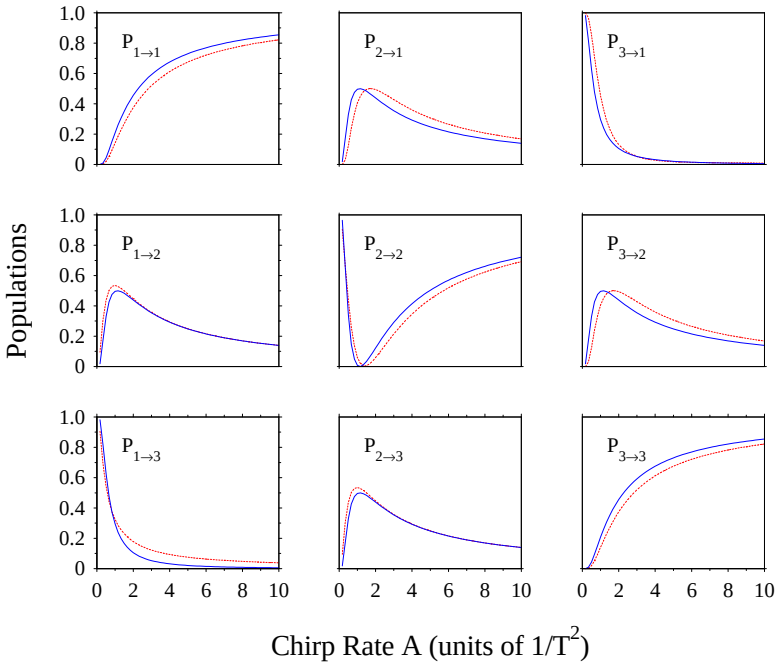

Figure 2.6: Comparison of the probabilities (2.33) in the exactly soluble Carroll-Hioe model (dashed red line) with our approximate solution (2.20) (solid blue line) for $\Delta_0 = 0$ as functions of the chirp rate A. Here $\Omega = 1/T$.

$a \gg 1$. For $a \ll 1$ the approximation (2.20) and the CH solution (2.33) read, up to $\mathcal{O}(a^4)$, respectively

$$\mathbf{P} \sim \begin{bmatrix} 1 - 5\pi a^2/4 & \pi a^2 & \pi a^2/4 \\ \pi a^2 & 1 - 2\pi a^2 & \pi a^2 \\ \pi a^2/4 & \pi a^2 & 1 - 5\pi a^2/4 \end{bmatrix}, \tag{2.35a}$$

$$\mathbf{P}_{CH} \sim \begin{bmatrix} 1 - \pi a^2 & \pi a^2 & 0 \\ \pi a^2 & 1 - 2\pi a^2 & \pi a^2 \\ 0 & \pi a^2 & 1 - \pi a^2 \end{bmatrix}. \tag{2.35b}$$

For $a \gg 1$ they read, up to $\mathcal{O}(e^{-\pi a^2})$, respectively

$$\mathbf{P} \sim \begin{bmatrix} 0 & e^{-\pi a^2/4} & 1 - e^{-\pi a^2/4} \\ 0 & 1 - e^{-\pi a^2/4} & e^{-\pi a^2/4} \\ 1 & 0 & 0 \end{bmatrix}, \tag{2.36a}$$

$$\mathbf{P}_{CH} \sim \begin{bmatrix} 0 & 2e^{-\pi a^2/2} & 1 - 2e^{-\pi a^2/2} \\ 2e^{-\pi a^2/2} & 1 - 4e^{-\pi a^2/2} & 2e^{-\pi a^2/2} \\ 1 - 2e^{-\pi a^2/2} & 2e^{-\pi a^2/2} & 0 \end{bmatrix}. \tag{2.36b}$$

Equations (2.35a) and (2.35b) demonstrate that our approximate solution (2.20) reproduces

well, for some probabilities even exactly, the correct small-a asymptotics, which corresponds to the large-A ranges in Fig. 2.6. The reason is that the small-a (diabatic) regime corresponds to weak coupling; in the perturbative regime the presence of level crossings, let alone their distribution in time, is less significant. In the large-a (adiabatic) regime the crossings become very important and definitive for the dynamics. Then Eq. (2.36a) deviates from the correct asymptotics (2.36b), but still has the correct asymptotic values for $a \to \infty$. The correct, or nearly correct, small-a and large-a asymptotics of our approximate solution (2.20) explain its surprising overall accuracy in Fig. 2.6.

2.6 Discussion and Conclusions

We have developed an approximate analytical model that describes the time-dependent dynamics of a quantum system with three states, which have linearly changing energies of different slopes and are coupled with pulse-shaped interactions. Our approach is based upon the two-state LZ model, i.e. we assume independent pairwise transitions between neighboring states, described by the LZ model. We have performed detailed comparison of our analytic approximation with numerical simulations, versus all possible interaction parameters and for all nine transition probabilities, which has revealed a remarkable accuracy, not only in smooth features, but also in describing detailed interference features. This accuracy shows that indeed, the physical mechanism of the three-state dynamics is dominated by separated pairwise LZ transitions, even when the crossings are too close to each other.

We have derived the *formal* conditions of validity of our LZ approach, Eqs. (2.23), using the concept of transition time. However, a comparison with numeric simulations has revealed that our approximation is valid well beyond the formal ranges of validity. One of the reasons is that for two of the survival probabilities, $P_{1\to1}$ and $P_{3\to3}$, our LZ approximation produces the exact results. We have found that even in the extreme case of vanishing static detuning, where our approach *should not be valid* because the three crossings coalesce into a triply degenerate bowtie single crossing, it still produces remarkably accurate results because of nearly correct asymptotic behaviors of the transition probabilities.

One of the useful and interesting features of the "triangle" linkage pattern (Fig. 2.1) is the presence of intrinsic interference effects. Our "sandwich" approach, with its implementation in the adiabatic interaction representation, allows for an easy incorporation of different evolution paths in Hilbert space between a particular pair of states. Such *path interferences* are identified in only four of the nine probabilities. Another source of interferences could be nonadiabatic

transitions in the wings of the Gaussian pulses, where the nonadiabatic couplings possess local maxima; these interferences would be visible in all nine probabilities. We have found, however, that only the path interferences are clearly identified.

A substantial contribution to the path interferences is played by the LZ phases $\phi_{\varkappa}$. The LZ phase is often neglected in applications of the LZ model to multiple crossings, in the so-called "independent crossing" approximation, where only probabilities are accounted for. Although such an approach occasionally works, miraculously, as in the exactly soluble Demkov-Osherov [22] and Demkov-Ostrovsky [23] models, the present simple, but very instructive model, demonstrates that in general, the LZ phase, as well the dynamical adiabatic phases, has to be properly accounted for, which is achieved best in an evolution-matrix approach, preferably in the adiabatic-interaction representation [24].

In order to be closer to experimental reality, in the examples we have assumed pulsed interactions, specifically of Gaussian time dependence. This proved to be no hindrance for the accuracy of the model, which is remarkable because we have applied the LZ model (which presumes constant couplings) at crossings (the first and the last ones) situated at the wings of the Gaussian-shaped couplings where the latter change rapidly. This robustness of the approach can be traced to the use of the adiabatic basis where the pulse-shape details are accounted for in the adiabatic phases.

We have used the analytic results to derive some useful features of the dynamics, for instance, we have found explicitly the parameter values for which certain probabilities reach the 50% level, and for which a maximally coherent superposition is created of all three states $P_1 = P_2 = P_3 = 1/3$.

In the specific derivations we have assumed for the sake of simplicity equal couplings for the two transitions and slopes of different signs but equal magnitudes for two of the energies. These assumptions simplify considerably the ensuing expressions for the probabilities; moreover, they are actually present in some important applications (quantum rotors, Zeeman sublevels in magnetic field and spin-spin entanglement). The formalism is readily extended to the general case, of unequal couplings and different slopes, and we have verified that the resulting LZ-based approximation is very accurate again.

To conclude, the present work demonstrates that, once again, the LZ model outperforms expectations when applied to multistate dynamics, with multiple level crossings and a multitude of evolution paths.

Chapter 3

Degenerate Landau-Zener Model

In this chapter a generalization of the famous Landau-Zener model is developed. We generalize the model to describe transitions between two degenerate sets of states and show some interesting effects: not all transition probabilities exist for infinite time duration. In general, apart from some special cases, only the transition probabilities between states within the same degenerate set exist, but not between states of different sets.

3.1 Definition of the degenerate Landau-Zener model

We consider a quantum system with N_a degenerate states $\{|\psi_m\rangle\}_{m=1}^{N_a}$ in the (lower) a set and N_b states $\{|\psi_{N_a+n}\rangle\}_{n=1}^{N_b}$ in the (upper) b set, as displayed in Fig. 3.1 (top). Without loss of generality we assume that $N_a \geqq N_b$. Each of the a states $|\psi_m\rangle$ is coupled to each of the b states $|\psi_n\rangle$ by a constant coupling Ω_{mn}, and all couplings can be different. The a states are not coupled to each other directly, neither are the b states. All fields are off resonance by the same detuning $\Delta(t)$, which is assumed to be linear in time, with a rate C (*chirp* in coherent atomic excitation [4, 53]),

$$\Omega_{mn} = \text{const}, \tag{3.1a}$$

$$\Delta(t) = Ct. \tag{3.1b}$$

For $N_b = 1$ the present model reduces to the N-pod model solved by Kyoseva and Vitanov [54], and for $N_a = N_b = 1$ to the nondegenerate original LZ model. The present model is therefore a generalization of the N-pod model to a degenerate b level.

We adopt a state ordering wherein the N_a sublevels of the a level are placed first, followed by the N_b sublevels of the b level. In the rotating-wave approximation (RWA) the Schrödinger

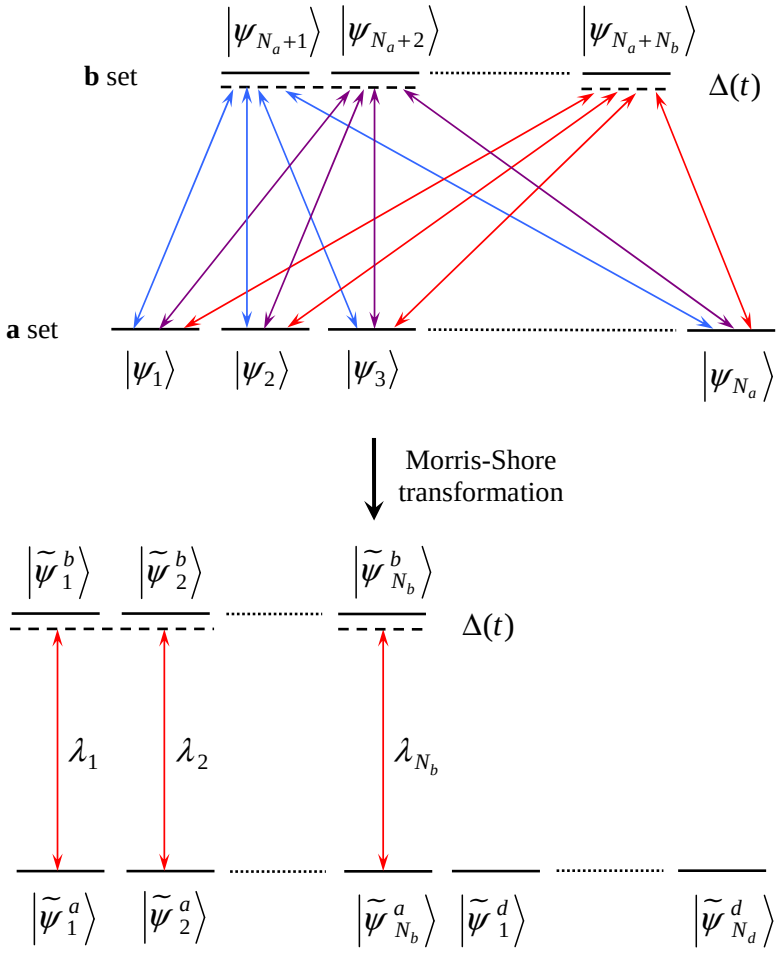

Figure 3.1: The Morris-Shore transformation: a multistate system consisting of two coupled sets of degenerate levels is decomposed into a set of independent nondegenerate two-state systems and a set of decoupled states.

equation of the system reads [4]

$$i\hbar\frac{d}{dt}\mathbf{C}(t) = \mathbf{H}(t)\mathbf{C}(t), \tag{3.2}$$

where the elements of the $(N_a + N_b)$-dimensional vector $\mathbf{C}(t)$ are the probability amplitudes of the states. The adopted state ordering allows us to write the RWA Hamiltonian as a block matrix,

$$\mathbf{H}(t) = \begin{bmatrix} \mathbf{0} & \mathbf{V} \\ \mathbf{V}^\dagger & \mathbf{D}(t) \end{bmatrix}, \tag{3.3}$$

Here $\mathbf{0}$ is the N_a-dimensional square zero matrix, in which the zero off-diagonal elements indicate the absence of couplings between the a states, while the zero diagonal elements show that the a states have the same energy, which is taken as the zero of the energy scale. The matrix $\mathbf{D}(t)$ is an N_b-dimensional square diagonal matrix, with $\Delta(t)$ on the diagonal, $\mathbf{D}(t) = \Delta(t)\mathbf{1}_{N_b}$. The

absence of off-diagonal elements in $\mathbf{D}$ reflects again the absence of couplings between the b states, while the diagonal elements Δ stand for the common energy of all b states.

In Eq. (3.3) $\mathbf{V}$ is an $(N_a \times N_b)$-dimensional interaction matrix with constant elements,

$$\mathbf{V} = \begin{bmatrix} \Omega_{11} & \Omega_{12} & ... & \Omega_{1N_b} \\ \Omega_{21} & \Omega_{22} & ... & \Omega_{2N_b} \\ \vdots & \vdots & ... & \vdots \\ \Omega_{N_a1} & \Omega_{N_a2} & ... & \Omega_{N_aN_b} \end{bmatrix} = [|\Omega_1\rangle, |\Omega_2\rangle, \ldots, |\Omega_{N_b}\rangle], \tag{3.4}$$

where $|\Omega_n\rangle$ $(n = 1, 2, \ldots, N_b)$ are N_a-dimensional vectors comprising the interactions of the nth state of the b set with all states of the a set,

$$|\Omega_n\rangle = \begin{bmatrix} \Omega_{1n} \\ \Omega_{2n} \\ \vdots \\ \Omega_{N_an} \end{bmatrix} \quad (n = 1, 2, \ldots, N_b). \tag{3.5}$$

3.2 Exact analytic solution of the degenerate Landau-Zener model

3.2.1 Morris-Shore transformation

We shall solve the degenerate LZ problem by using the Morris-Shore (MS) transformation [55]. Morris and Shore have shown that any degenerate two-level system, in which all couplings share the same time dependence (constant in our case) and the same detuning (linear here), can be reduced with a constant unitary transformation $\mathbf{S}$ to an equivalent system comprising only independent two-state systems and uncoupled (dark) states, as shown in Fig. 3.1. This transformation reads

$$|\psi_i\rangle = \sum_k S_{ki} |\widetilde{\psi}_k\rangle \quad \Longleftrightarrow \quad |\widetilde{\psi}_k\rangle = \sum_i S^*_{ki} |\psi_i\rangle, \tag{3.6}$$

where the tildas denote the MS basis hereafter. The constant transformation matrix $\mathbf{S}$ can be represented in the block-matrix form

$$\mathbf{S} = \begin{bmatrix} \mathbf{A} & \mathbf{O} \\ \mathbf{O} & \mathbf{B} \end{bmatrix}, \tag{3.7}$$

where $\mathbf{A}$ is a unitary N_a-dimensional square matrix and $\mathbf{B}$ is a unitary N_b-dimensional square matrix, $\mathbf{A}\mathbf{A}^\dagger = \mathbf{A}^\dagger\mathbf{A} = \mathbf{1}_{N_a}$ and $\mathbf{B}\mathbf{B}^\dagger = \mathbf{B}^\dagger\mathbf{B} = \mathbf{1}_{N_b}$. The constant matrices $\mathbf{A}$ and $\mathbf{B}$ mix

only sublevels of a given level: $\mathbf{A}$ mixes the a sublevels and $\mathbf{B}$ mixes the b sublevels. The transformed MS Hamiltonian has the form

$$\widetilde{\mathbf{H}}(t) = \mathbf{S}\mathbf{H}(t)\mathbf{S}^\dagger = \begin{bmatrix} \mathbf{O} & \widetilde{\mathbf{V}} \\ \widetilde{\mathbf{V}}^\dagger & \mathbf{D}(t) \end{bmatrix}, \tag{3.8}$$

where

$$\widetilde{\mathbf{V}} = \mathbf{A}\mathbf{V}\mathbf{B}^\dagger. \tag{3.9}$$

The $N_a \times N_b$ matrix $\widetilde{\mathbf{V}}$ has $N_d = N_a - N_b$ null rows ($N_a \geqq N_b$), which correspond to decoupled states. The decomposition of $\mathbf{H}$ into a set of independent two-state systems requires that, after removing the null rows, $\widetilde{\mathbf{V}}$ reduces to a N_b-dimensional diagonal matrix; let us denote its diagonal elements by λ_n ($n = 1, 2, \ldots, N_b$).

It follows from Eq. (3.9) that

$$\widetilde{\mathbf{V}}\widetilde{\mathbf{V}}^\dagger = \mathbf{A}\mathbf{V}\mathbf{V}^\dagger\mathbf{A}^\dagger, \tag{3.10a}$$

$$\widetilde{\mathbf{V}}^\dagger\widetilde{\mathbf{V}} = \mathbf{B}\mathbf{V}^\dagger\mathbf{V}\mathbf{B}^\dagger. \tag{3.10b}$$

Hence $\mathbf{A}$ and $\mathbf{B}$ are defined by the condition that they diagonalize $\mathbf{V}\mathbf{V}^\dagger$ and $\mathbf{V}^\dagger\mathbf{V}$, respectively. It is important to note that the square matrices $\mathbf{V}\mathbf{V}^\dagger$ and $\mathbf{V}^\dagger\mathbf{V}$ have different dimensions, N_a and N_b, respectively. Because all elements of $\mathbf{V}$ are constant, $\mathbf{A}$ and $\mathbf{B}$ are also constant. It is straightforward to show that the N_b eigenvalues of $\mathbf{V}^\dagger\mathbf{V}$ are all non-negative; according to Eqs. (3.9) and (3.10) they are λ_n^2 ($n = 1, 2, \ldots, N_b$). The matrix $\mathbf{V}\mathbf{V}^\dagger$ has the same eigenvalues and additional $N_d = N_a - N_b$ zero eigenvalues.

The MS Hamiltonian (3.8) has the explicit form

$$\widetilde{\mathbf{H}} = \begin{bmatrix} \mathbf{0}_{N_d} & & & & \mathbf{0} & & & & \\ & 0 & 0 & \cdots & 0 & \lambda_1 & 0 & \cdots & 0 \\ & 0 & 0 & \cdots & 0 & 0 & \lambda_2 & \cdots & 0 \\ & \vdots & \vdots & \ddots & \vdots & \vdots & \vdots & \ddots & \vdots \\ \mathbf{0} & 0 & 0 & \cdots & 0 & 0 & 0 & \cdots & \lambda_{N_b} \\ & \lambda_1 & 0 & \cdots & 0 & \Delta & 0 & \cdots & 0 \\ & 0 & \lambda_2 & \cdots & 0 & 0 & \Delta & \cdots & 0 \\ & \vdots & \vdots & \ddots & \vdots & \vdots & \vdots & \ddots & \vdots \\ & 0 & 0 & \cdots & \lambda_{N_b} & 0 & 0 & \cdots & \Delta \end{bmatrix}. \tag{3.11}$$

The structure of $\widetilde{\mathbf{H}}$ shows that in the MS basis the dynamics is decomposed into sets of N_d decoupled single states, and N_b independent two-state systems $|\widetilde{\psi}_n^a\rangle \leftrightarrow |\widetilde{\psi}_n^b\rangle$ ($n = 1, 2, \ldots, N_b$),

each composed of an a state $|\widetilde{\psi}_n^a\rangle$ and a b state $|\widetilde{\psi}_n^b\rangle$, and driven by the Hamiltonians,

$$\widetilde{\mathbf{H}}_n(t) = \begin{bmatrix} 0 & \lambda_n \\ \lambda_n & \Delta(t) \end{bmatrix} \quad (n = 1, 2, \ldots, N_b). \tag{3.12}$$

These two-state Hamiltonians have the same detuning $\Delta(t)$ but different couplings λ_n. Each of the new a states $|\widetilde{\psi}_n^a\rangle$ is the eigenstate of $\mathbf{V}\mathbf{V}^\dagger$ corresponding to the eigenvalue λ_n^2, whereas each of the new b states $|\widetilde{\psi}_n^b\rangle$ is the eigenstate of $\mathbf{V}^\dagger\mathbf{V}$, corresponding to the same eigenvalue λ_n^2. The square root of this common eigenvalue, λ_n, represents the coupling between $|\widetilde{\psi}_n^a\rangle$ and $|\widetilde{\psi}_n^b\rangle$. The N_d zero eigenvalues of $\mathbf{V}\mathbf{V}^\dagger$ correspond to decoupled (dark) states in the a set (since we assume that $N_a \geqq N_b$, dark states, if any, are in the a set). The dark states are decoupled from the dynamical evolution because they are driven by one-dimensional null Hamiltonians.

3.2.2 Solution to the degenerate LZ problem

The MS transformation

The MS decomposition allows us to reduce the degenerate two-level LZ problem to a set of nondegenerate two-state LZ problems, wherein the detuning is unchanged and given by Eq. (3.1b) while the couplings λ_n, defined as the square roots of the eigenvalues of $\mathbf{V}^\dagger\mathbf{V}$, are combinations of the initial couplings between the a and b states.

From the vector form (3.4) of $\mathbf{V}$ we obtain

$$\mathbf{V}\mathbf{V}^\dagger = \sum_{n=1}^{N_b} |\Omega_n\rangle \langle\Omega_n| , \tag{3.13a}$$

$$\mathbf{V}^\dagger\mathbf{V} = \begin{bmatrix} \langle\Omega_1|\Omega_1\rangle & \langle\Omega_1|\Omega_2\rangle & \cdots & \langle\Omega_1|\Omega_{N_b}\rangle \\ \langle\Omega_2|\Omega_1\rangle & \langle\Omega_2|\Omega_2\rangle & \cdots & \langle\Omega_2|\Omega_{N_b}\rangle \\ \vdots & \vdots & \ddots & \vdots \\ \langle\Omega_{N_b}|\Omega_1\rangle & \langle\Omega_{N_b}|\Omega_2\rangle & \cdots & \langle\Omega_{N_b}|\Omega_{N_b}\rangle \end{bmatrix}. \tag{3.13b}$$

Note that $\mathbf{V}^\dagger\mathbf{V}$ is the Gram matrix for the set of vectors $\{|\Omega_n\rangle\}_{n=1}^{N_b}$. Thus if all these vectors are linearly independent then $\det \mathbf{V}^\dagger\mathbf{V} \neq 0$ and all eigenvalues of $\mathbf{V}^\dagger\mathbf{V}$ are nonzero [56]; however, this assumption is unnecessary.

We assume that we can find the eigenvalues λ_n^2 $(n = 1, 2, \ldots, N_b)$ of the matrices (3.13a) and (3.13b), and the corresponding orthonormalized eigenvectors: the N_b coupled eigenstates $|\widetilde{\psi}_n^a\rangle$ of $\mathbf{V}\mathbf{V}^\dagger$ and $|\widetilde{\psi}_n^b\rangle$ of $\mathbf{V}^\dagger\mathbf{V}$, and the N_d decoupled eigenstates $|\widetilde{\psi}_k^d\rangle$ of $\mathbf{V}\mathbf{V}^\dagger$. We use these

eigenstates to construct the transformation matrices as

$$\mathbf{A} = \begin{bmatrix} \langle\widetilde{\psi}_1^d| \\ \vdots \\ \langle\widetilde{\psi}_{N_d}^d| \\ \langle\widetilde{\psi}_1^a| \\ \vdots \\ \langle\widetilde{\psi}_{N_b}^a| \end{bmatrix}, \quad \mathbf{B} = \begin{bmatrix} \langle\widetilde{\psi}_1^b| \\ \vdots \\ \langle\widetilde{\psi}_{N_b}^b| \end{bmatrix}. \tag{3.14}$$

Then according to the general theory the transformed interaction matrix (3.9) in the MS basis takes the form (3.11), where the positions of the N_d zero eigenvalues and the N_b eigenvalues λ_n are determined by the ordering of the eigenstates in the transformation matrices (3.14).

The MS propagators

Because the dark states are decoupled and have zero energies, their propagator is the unit matrix $\mathbf{1}_{N_d}$.

The propagator for each of the two-state MS Hamiltonians (3.12) is the LZ propagator for the respective coupling λ_n,

$$\widetilde{\mathbf{U}}_n = e^{-i\delta/2} \begin{bmatrix} \alpha_n & -\beta_n^* \\ \beta_n & \alpha_n^* \end{bmatrix}, \tag{3.15a}$$

$$\delta = \int_{t_i}^{t_f} \Delta(t)dt = \frac{1}{2}\left(\tau_f^2 - \tau_i^2\right). \tag{3.15b}$$

The Cayley-Klein parameters are [57]

$$\begin{aligned} \alpha &= \frac{\Gamma(1-i\kappa^2)}{\sqrt{2\pi}} \left[D_{i\kappa^2}(\tau_f e^{-i\pi/4}) D_{i\kappa^2-1}(\tau_i e^{3i\pi/4}) \right. \\ &\quad \left. + D_{i\kappa^2}(\tau_f e^{3i\pi/4}) D_{i\kappa^2-1}(\tau_i e^{-i\pi/4}) \right], \end{aligned} \tag{3.16a}$$

$$\begin{aligned} \beta &= \frac{\Gamma(1-i\kappa^2)}{\kappa\sqrt{2\pi}} e^{i\pi/4} \left[-D_{i\kappa^2}(\tau_f e^{-i\pi/4}) D_{i\kappa^2}(\tau_i e^{3i\pi/4}) \right. \\ &\quad \left. + D_{i\kappa^2}(\tau_f e^{3i\pi/4}) D_{i\kappa^2}(\tau_i e^{-i\pi/4}) \right], \end{aligned} \tag{3.16b}$$

where $\kappa = \Omega_0/\sqrt{C}$, $\tau = t\sqrt{C}$, and $D_v(z)$ is the parabolic-cylinder function. $\tau_i = t_i\sqrt{C}$ and $\tau_f = t_f\sqrt{C}$ are the scaled initial and final times, respectively. In the original LZ model, $\tau_i \to -\infty$ and $\tau_f \to \infty$, and the Cayley-Klein parameters read [57]

$$\alpha_n = e^{-\pi\Lambda_n}, \tag{3.17a}$$

$$\beta_n = -e^{i\phi_n}\sqrt{1 - e^{-2\pi\Lambda_n}}, \tag{3.17b}$$

with

$$\Lambda_n = \frac{\lambda_n^2}{C}, \tag{3.18a}$$

$$\phi_n = \frac{\tau_i^2+\tau_f^2}{4} + \frac{1}{2}\Lambda_n \ln\left(\tau_i^2\tau_f^2\right) + \phi_n^{LZ}, \tag{3.18b}$$

$$\phi_n^{LZ} = \frac{\pi}{4} + \arg\Gamma\left(1-i\Lambda_n\right). \tag{3.18c}$$

Hence the phase ϕ_n diverges, which is a result of the unphysical assumption of an infinitely long interaction duration. This divergence is unimportant in the original LZ model because the transition probability,

$$P_n = |\beta_n|^2 = 1 - e^{-2\pi\Lambda_n}, \tag{3.19}$$

is well defined. Hence the final populations are well defined if the system starts in one of the two states, which is usually the case. However, when the system starts in a *superposition* of states, this divergence does not allow to calculate the populations, even in the original LZ model. We shall show below that in the degenerate LZ model this divergence does not allow for definite values of some populations even when the system starts in a single state.

There are two divergent terms in the phase (3.18b): polynomial and logarithmic, with different origins and different implications. The term $\frac{1}{4}(\tau_i^2+\tau_f^2)$ is unimportant in the present context because it derives from the chosen Schrödinger representation (3.3); in the interaction representation (when the detunings turn into phase factors of the couplings) it disappears. Moreover, this term is the same for all β_n and factors out of the probabilities (see below). The term $\frac{1}{2}\Lambda_n \ln(\tau_i^2\tau_f^2)$, however, depends on β_n; it arises from the nonvanishing coupling and the rather slow divergence of the detuning. These logarithmic terms cannot be factored out, unless the MS couplings λ_n coincide or vanish by accident, and appear in some transition probabilities, as we shall see below.

The propagator in the original basis

By taking into account the LZ propagators (3.15) for the N_b two-state MS systems, the ordering of the states, and the MS Hamiltonian (3.11), the full propagator in the MS basis can be written

as

$$\widetilde{\mathbf{U}} = \begin{bmatrix} \mathbf{1}_{N_d} & & & & \mathbf{0} & & & \\ & \alpha_1 & 0 & \cdots & 0 & -\beta_1^* & 0 & \cdots & 0 \\ & 0 & \alpha_2 & \cdots & 0 & 0 & -\beta_2^* & \cdots & 0 \\ & \vdots & \vdots & \ddots & \vdots & \vdots & \vdots & \ddots & \vdots \\ & 0 & 0 & \cdots & \alpha_{N_b} & 0 & 0 & \cdots & -\beta_{N_b}^* \\ \mathbf{0} & \beta_1 & 0 & \cdots & 0 & \alpha_1^* & 0 & \cdots & 0 \\ & 0 & \beta_2 & \cdots & 0 & 0 & \alpha_2^* & \cdots & 0 \\ & \vdots & \vdots & \ddots & \vdots & \vdots & \vdots & \ddots & \vdots \\ & 0 & 0 & \cdots & \beta_{N_b} & 0 & 0 & \cdots & \alpha_{N_b}^* \end{bmatrix}. \tag{3.20}$$

By using the completeness relation

$$\sum_{n=1}^{N_b} |\widetilde{\psi}_n^a\rangle\langle\widetilde{\psi}_n^a| + \sum_{k=1}^{N_d} |\widetilde{\psi}_k^d\rangle\langle\widetilde{\psi}_k^d| = \mathbf{1}_{N_a}, \tag{3.21}$$

it is straightforward to show that the propagator in the original basis $\mathbf{U} = \mathbf{S}^\dagger\widetilde{\mathbf{U}}\mathbf{S}$ reads

$$\mathbf{U} = \begin{bmatrix} \mathbf{1}+\sum_{n=1}^{N_b}(\alpha_n-1)|\widetilde{\psi}_n^a\rangle\langle\widetilde{\psi}_n^a| & -\sum_{n=1}^{N_b}\beta_n^*|\widetilde{\psi}_n^a\rangle\langle\widetilde{\psi}_n^b| \\ \sum_{n=1}^{N_b}\beta_n|\widetilde{\psi}_n^b\rangle\langle\widetilde{\psi}_n^a| & \sum_{n=1}^{N_b}\alpha_n^*|\widetilde{\psi}_n^b\rangle\langle\widetilde{\psi}_n^b| \end{bmatrix}. \tag{3.22}$$

Note that the propagator does not depend on the decoupled states $|\widetilde{\psi}_k^d\rangle$ $(k = 1, 2, \ldots, N_d)$, which are excluded by using Eq. (3.21). This has to be expected because, owing to their degeneracy, the choice of the decoupled states is not unique: any superposition of them is also a zero-eigenvalue eigenstate of $\mathbf{V}\mathbf{V}^\dagger$. Because the dynamics in the original basis must not depend on such arbitrariness, the propagator $\mathbf{U}$ must not depend on the decoupled states at all.

Transition probabilities

If the system starts in an arbitrary state $|\psi_i\rangle$ of the a set then Eq. (3.22) gives for the matrix elements $U_{fi} = \langle\psi_f|\mathbf{U}|\psi_i\rangle$ the expressions

$$U_{fi} = \begin{cases} \delta_{fi} + \sum_{n=1}^{N_b}(\alpha_n - 1)\, a_{fn}a_{in}^* & (f \in a \text{ set}), \\ \sum_{n=1}^{N_b}\beta_n b_{fn}a_{in}^* & (f \in b \text{ set}), \end{cases} \tag{3.23}$$

where a_{kn} and b_{kn} denote the components of the MS states $|\widetilde{\psi}_n^a\rangle$ and $|\widetilde{\psi}_n^b\rangle$, respectively,

$$|\widetilde{\psi}_n^a\rangle = [a_{1n}, a_{2n}, \ldots, a_{N_a n}]^T, \tag{3.24a}$$

$$|\widetilde{\psi}_n^b\rangle = [b_{1n}, b_{2n}, \ldots, b_{N_b n}]^T. \tag{3.24b}$$

If the initial state $|\psi_i\rangle$ belongs to the b set, we have

$$U_{fi} = \begin{cases} -\sum_{n=1}^{N_b} \beta_n^* a_{fn} b_{in}^* & (f \in a \text{ set}), \\ \sum_{n=1}^{N_b} \alpha_n^* b_{fn} b_{in}^* & (f \in b \text{ set}). \end{cases} \tag{3.25}$$

In both cases, the transition probability from state $|\psi_i\rangle$ to state $|\psi_f\rangle$ is

$$P_{i\to f} = |U_{fi}|^2 . \tag{3.26}$$

Equations (3.23)-(3.26) reveal several important features of the degenerate LZ model.

(i) The transition probability $P_{i\to f}$ is always well defined if the initial and final states belong to the same set of states (a or b) because then $P_{i\to f}$ involves only the Cayley-Klein parameters α_n, which are real and positive and hence do not have divergent phases, see Eq. (3.17a).

(ii) When the initial and final states belong to different sets, $|\psi_i\rangle$ to the a set and $|\psi_f\rangle$ to the b set, or vice versa, the transition probability $P_{i\to f}$ is well defined only if the corresponding sums in Eq. (3.23) or (3.25) reduce to one term (because some of the a and b coefficients may vanish accidentally) or if the phases of all participating β_n's are the same. The latter may only happen accidentally if all MS couplings λ_n are equal: then the phases factor out and cancel in the transition probability.

(iii) Baring accidental cases discussed in the previous point, the transition probabilities between states from different sets are *not defined* due to the divergence of the phases of the Cayley-Klein LZ parameters β_n.

Summary

In summary, Eq. (3.22) gives the propagator for the degenerate LZ model. The transition probabilities can be calculated from Eqs. (3.23)-(3.26), which require the knowledge of the coupled MS states $|\widetilde{\psi}_n^a\rangle$ of the a set and $|\widetilde{\psi}_n^b\rangle$ of the b set. The former are the eigenstates of $\mathbf{V}\mathbf{V}^\dagger$ and the latter are the eigenstates of $\mathbf{V}^\dagger\mathbf{V}$. The knowledge of the decoupled zero-eigenvalue states $|\widetilde{\psi}_n^d\rangle$ of the a set is not necessary for the calculation of the propagator. Not all transition probabilities are defined for infinite time duration because of the divergent phases of the Cayley-Klein parameters β_n. For any *finite* initial and final times, though, all transition probabilities are well defined.

An alternative: the Allen-Eberly-Hioe model

In a real physical situation with degenerate levels, a more realistic alternative to the LZ model is the lesser known Allen-Eberly-Hioe model [53, 58]

$$\Omega(t) = \Omega_0 \,\mathrm{sech}(t/T), \tag{3.27a}$$

$$\Delta(t) = B \tanh(t/T). \tag{3.27b}$$

Here the coupling $\Omega(t)$ is a bell-shaped pulse, with a characteristic width T. The detuning crosses resonance at time $t = 0$ and does not diverge at infinity but tends to the finite values $\pm B$. The Cayley-Klein parameters for this model, including their phases, are well defined.

3.3 Examples

3.3.1 $J_a = 2 \leftrightarrow J_b = 1$ transition

General case

We illustrate the above results with a specific example: transition between two atomic levels with total angular momenta $J_a = 2$ and $J_b = 1$ in the field of two circularly polarized (right σ^+ and left σ^-) chirped-frequency laser fields with linear chirp and steady amplitudes. In the absence of magnetic fields, the 5 magnetic sublevels of the J_a level are degenerate and so are the 3 magnetic sublevels of the J_b level, as shown in Fig. 3.2. This system therefore represents a physical realization of the degenerate LZ model with $N_a = 5$ and $N_b = 3$. When only σ^+ and σ^- polarized fields are present the eight-state system decouples into a five-state M system, which is composed of the sublevels with $M_a = -2, 0, 2$ and $M_b = -1, 1$, and a three-state Λ system comprising the sublevels with $M_a = -1, 1$ and $M_b = 0$ [59]. If there is also a linearly (π) polarized field then the M and Λ systems couple and all eight states will be involved in the dynamics.

The two σ^+ and σ^- polarized fields can be produced by a single elliptically polarized field; then the amplitude ratio and the relative phase of the σ^+ and σ^- fields can be controlled, respectively, by the ellipticity and the rotation angle of the field. Moreover the σ^+ and σ^- fields will have automatically the same detuning.

We shall only consider the M-system, because the Λ-system contains a non-degenerate upper state and can be treated with a simpler formalism [54].

The interaction matrix for the M system, with the Clebsch-Gordan coefficients accounted

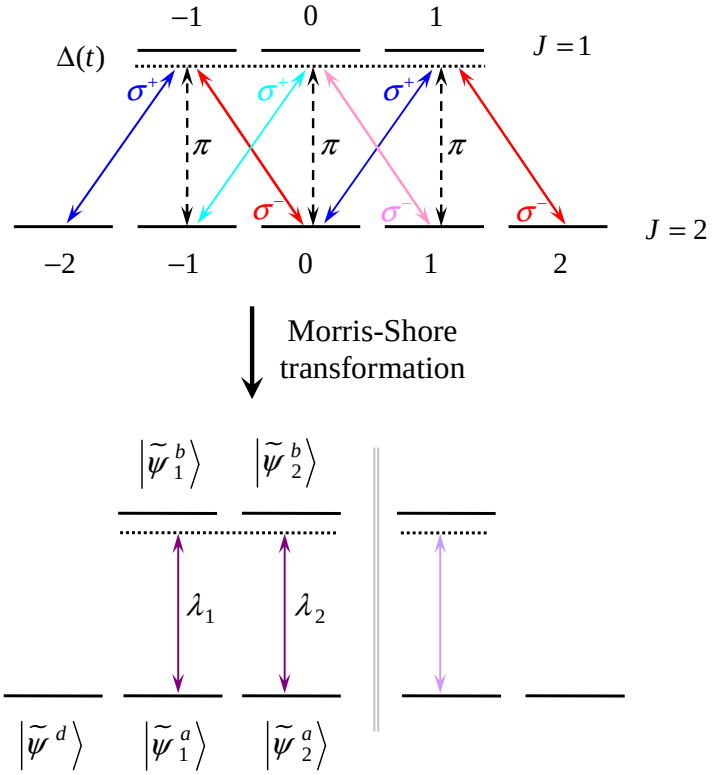

Figure 3.2: The $J_a = 2 \leftrightarrow J_b = 1$ transition in the original basis (top) and in the MS basis (bottom). With only circularly polarized fields the full eight-state system decouples into a five-state M system and a three-state Λ system. A linearly polarized field would couple the M and Λ systems. The Morris-Shore transformation turns the M system into a pair of two independent nondegenerate two-state systems and a decoupled state (bottom left), and the Λ system into a two-state system and a decoupled state (bottom right).

for, reads [59]

$$\mathbf{V} = \frac{1}{\sqrt{10}} \begin{bmatrix} \sqrt{6}\Omega_+ e^{i\theta_+} & 0 \\ \Omega_- e^{i\theta_-} & \Omega_+ e^{i\theta_+} \\ 0 & \sqrt{6}\Omega_- e^{i\theta_-} \end{bmatrix}, \tag{3.28}$$

and hence the matrices $\mathbf{V}\mathbf{V}^\dagger$ and $\mathbf{V}^\dagger\mathbf{V}$ are

$$\mathbf{V}\mathbf{V}^\dagger = \frac{1}{10} \begin{bmatrix} 6\Omega_+^2 & \sqrt{6}\Omega_+\Omega_- e^{i\theta} & 0 \\ \sqrt{6}\Omega_+\Omega_- e^{-i\theta} & \Omega_-^2 + \Omega_+^2 & \sqrt{6}\Omega_+\Omega_- e^{i\theta} \\ 0 & \sqrt{6}\Omega_+\Omega_- e^{-i\theta} & 6\Omega_-^2 \end{bmatrix}, \tag{3.29a}$$

$$\mathbf{V}^\dagger\mathbf{V} = \frac{1}{10} \begin{bmatrix} 6\Omega_+^2 + \Omega_-^2 & \Omega_+\Omega_- e^{i\theta} \\ \Omega_+\Omega_- e^{-i\theta} & \Omega_+^2 + 6\Omega_-^2 \end{bmatrix}, \tag{3.29b}$$

with $\theta = \theta_+ - \theta_-$ being the relative phase of the two fields. The eigenvalues of $\mathbf{V}\mathbf{V}^\dagger$ are λ_n^2

$(n = 0, 1, 2)$, where

$$\lambda_0 = 0, \tag{3.30a}$$

$$\lambda_{1,2} = \Omega\sqrt{\frac{7 \pm \sqrt{1+24\varepsilon^2}}{20}}, \tag{3.30b}$$

with $\Omega = \sqrt{\Omega_+^2 + \Omega_-^2}$ and $\varepsilon = (\Omega_+^2 - \Omega_-^2)/(\Omega_+^2 + \Omega_-^2)$. The eigenvalues of $\mathbf{V}^\dagger\mathbf{V}$ are λ_1^2 and λ_2^2. The eigenstates of $\mathbf{V}\mathbf{V}^\dagger$ are a decoupled state $|\widetilde{\psi}^d\rangle$ and two coupled states $|\widetilde{\psi}_1^a\rangle$ and $|\widetilde{\psi}_2^a\rangle$, which are composed of a states, whereas the eigenstates of $\mathbf{V}^\dagger\mathbf{V}$ are two new b states [59],

$$|\widetilde{\psi}^d\rangle = \sum_{m=-2,0,2} d'_m e^{-im\theta/2} |\psi_m\rangle\,, \tag{3.31a}$$

$$|\widetilde{\psi}_n^a\rangle = \sum_{m=-2,0,2} a'_{mn} e^{-im\theta/2} |\psi_m\rangle \quad (n = 1, 2), \tag{3.31b}$$

$$|\widetilde{\psi}_n^b\rangle = \sum_{m=-1,1} b'_{mn} e^{-im\theta/2} |\psi_m\rangle \quad (n = 1, 2). \tag{3.31c}$$

The coefficients of these new MS basis states are given in Table 3.1 [59]; they are related to the coefficients in Eqs. (3.23)-(3.26) as $d_m = d'_m e^{-im\theta/2}$, $a_{mn} = a'_{mn} e^{-im\theta/2}$, and $b_{mn} = b'_{mn} e^{-im\theta/2}$. By using these coefficients and Eqs. (3.15)-(3.18), (3.23)-(3.26), and (3.30), one can find the transition probability between any two states.

Case of equal couplings

We shall consider in some detail the special case $\Omega_+ = \Omega_-$; then $\varepsilon = 0$ and the coefficients in Table 3.1 simplify. The MS couplings (3.30b), the LZ factors, and the Cayley-Klein parameters reduce to

$$\lambda_1 = \Omega\sqrt{\frac{4}{10}}, \quad \Lambda_1 = \frac{4}{10}\frac{\Omega^2}{C}, \tag{3.32a}$$

$$\lambda_2 = \Omega\sqrt{\frac{3}{10}}, \quad \Lambda_2 = \frac{3}{10}\frac{\Omega^2}{C}. \tag{3.32b}$$

$$\alpha_1 = e^{-4\xi}, \quad \beta_1 = -e^{i\phi_1}\sqrt{1 - e^{-8\xi}}, \tag{3.32c}$$

$$\alpha_2 = e^{-3\xi}, \quad \beta_2 = -e^{i\phi_2}\sqrt{1 - e^{-6\xi}}, \tag{3.32d}$$

where $\xi = \pi\Omega^2/10\beta$. It is particularly significant that the coefficient $a_{0,2}$ associated with state $|\psi_0\rangle$ vanishes accidentally, $a_{0,2} = 0$, see Table 3.1. The implication is that the sums in Eqs. (3.23) and (3.25), which involve a_{mn} coefficients, reduce to just single terms when state $|\psi_0\rangle$ is involved. Consequently, all transition probabilities from and to state $|\psi_0\rangle$ are defined and the divergence of the phases ϕ_n does not show up here.

The propagator in the original basis reads (for $\theta = 0$)

$$\mathbf{U} = \begin{bmatrix} \frac{1}{8}+\frac{3}{8}e^{-4\xi}+\frac{1}{2}e^{-3\xi} & -\sqrt{\frac{3}{32}}\left(1-e^{-4\xi}\right) & \frac{1}{8}+\frac{3}{8}e^{-4\xi}-\frac{1}{2}e^{-3\xi} & -\sqrt{\frac{3}{16}}\beta_1^*+\frac{1}{2}\beta_2^* & -\sqrt{\frac{3}{16}}\beta_1^*-\frac{1}{2}\beta_2^* \\ -\sqrt{\frac{3}{32}}\left(1-e^{-4\xi}\right) & \frac{3}{4}+\frac{1}{4}e^{-4\xi} & -\sqrt{\frac{3}{32}}\left(1-e^{-4\xi}\right) & \sqrt{\frac{1}{8}\left(1-e^{-8\xi}\right)}e^{i\varphi_1} & \sqrt{\frac{1}{8}\left(1-e^{-8\xi}\right)}e^{i\varphi_1} \\ \frac{1}{8}+\frac{3}{8}e^{-4\xi}-\frac{1}{2}e^{-3\xi} & -\sqrt{\frac{3}{32}}\left(1-e^{-4\xi}\right) & \frac{1}{8}+\frac{3}{8}e^{-4\xi}+\frac{1}{2}e^{-3\xi} & -\sqrt{\frac{3}{16}}\beta_1^*-\frac{1}{2}\beta_2^* & -\sqrt{\frac{3}{16}}\beta_1^*+\frac{1}{2}\beta_2^* \\ \sqrt{\frac{3}{16}}\beta_1-\frac{1}{2}\beta_2 & -\sqrt{\frac{1}{8}\left(1-e^{-8\xi}\right)}e^{-i\varphi_1} & \sqrt{\frac{3}{16}}\beta_1+\frac{1}{2}\beta_2 & \frac{1}{2}\left(e^{-4\xi}+e^{-3\xi}\right) & \frac{1}{2}\left(e^{-4\xi}-e^{-3\xi}\right) \\ \sqrt{\frac{3}{16}}\beta_1+\frac{1}{2}\beta_2 & \sqrt{\frac{1}{8}\left(1-e^{-8\xi}\right)}e^{-i\varphi_1} & \sqrt{\frac{3}{16}}\beta_1-\frac{1}{2}\beta_2 & \frac{1}{2}\left(e^{-4\xi}-e^{-3\xi}\right) & \frac{1}{2}\left(e^{-4\xi}+e^{-3\xi}\right) \end{bmatrix}. \tag{3.33}$$

In the adiabatic limit $\xi \gg 1$ the matrix $\mathbf{P} = \{P_{fi}\}_{i,f=-2,0,2,-1,1}$ with the transition probabilities $P_{i\to f} = P_{fi}$ reads

$$\mathbf{P} = \begin{bmatrix} \frac{1}{64} & \frac{3}{32} & \frac{1}{64} & \left|\sqrt{\frac{3}{16}}e^{i\phi_1}-\frac{1}{2}e^{i\phi_2}\right|^2 & \left|\sqrt{\frac{3}{16}}e^{i\phi_1}+\frac{1}{2}e^{i\phi_2}\right|^2 \\ \frac{3}{32} & \frac{9}{16} & \frac{3}{32} & \frac{1}{8} & \frac{1}{8} \\ \frac{1}{64} & \frac{3}{32} & \frac{1}{64} & \left|\sqrt{\frac{3}{16}}e^{i\phi_1}+\frac{1}{2}e^{i\phi_2}\right|^2 & \left|\sqrt{\frac{3}{16}}e^{i\phi_1}-\frac{1}{2}e^{i\phi_2}\right|^2 \\ \left|\sqrt{\frac{3}{16}}e^{i\phi_1}-\frac{1}{2}e^{i\phi_2}\right|^2 & \frac{1}{8} & \left|\sqrt{\frac{3}{16}}e^{i\phi_1}+\frac{1}{2}e^{i\phi_2}\right|^2 & 0 & 0 \\ \left|\sqrt{\frac{3}{16}}e^{i\phi_1}+\frac{1}{2}e^{i\phi_2}\right|^2 & \frac{1}{8} & \left|\sqrt{\frac{3}{16}}e^{i\phi_1}-\frac{1}{2}e^{i\phi_2}\right|^2 & 0 & 0 \end{bmatrix}, \tag{3.34}$$

The β's which are left over in the propagator (3.33) have divergent phases, see Eqs. (3.17b) and (3.18b). Because the respective couplings λ_1 and λ_2 [Eq. (3.32)] are different, the logarithmic components in the phases of the β's are different and therefore give rise to an interference term in the transition probability, which oscillates in time with a logarithmically increasing frequency. Hence the transition probabilities with sums over different β's do not have a limit at infinity. At any *finite* times, however, these probabilities are well defined.

Figure 3.3 displays the time evolution of the populations of the five states in the near-adiabatic limit for linear polarization ($\varepsilon = 0$) and for three different initial conditions. In the top frame the system starts in the $J = 2$ state $|\psi_{-2}\rangle$. As predicted by Eq. (3.34) the populations of the $J = 2$ states acquire definite values as $t \to \infty$, while the populations of the $J = 1$ states oscillate: the logarithmic scale demonstrates that indeed, the oscillation phase diverges logarithmically.

Figure 3.3 (middle frame) displays the time evolution of the populations when the system starts in the $J = 2$ state $|\psi_0\rangle$. As predicted by Eq. (3.34) the populations of all five states acquire definite values at infinity, that is all transition probabilities exist, because of the accidental vanishing of the coefficient $a_{0,2}$, as discussed above.

Figure 3.3 (bottom frame) displays the time evolution of the populations when the system starts in the $J = 1$ state $|\psi_{-1}\rangle$. As predicted by Eq. (3.34) the populations of the $J = 1$ states acquire definite values (zero) as $t \to \infty$, while the populations of the $J = 2$ states oscillate,

with a logarithmic divergence of the oscillation phase. The exception is the population of state $|\psi_0\rangle$, which exists because of the accidental vanishing of the coefficient $a_{0,2}$.

3.3.2 The case of arbitrary transition with $J_a = J$ and $J_b = J - 1$ or J

For $J_a = J$ and $J_b = J - 1$ with integer J, in the presence of right and left circularly polarized fields only, the full $4J$-state system factorizes into two independent subsystems, like the M and Λ systems in Fig. 3.2. The larger, $(2J + 1)$-state system is formed of the magnetic sublevels $M_a = -J, -J+2, \ldots, J$ of the J_a level and $M_b = -J+1, -J+3, \ldots, J-1$ of the J_b level. The smaller, $(2J - 1)$-state system is formed of the magnetic sublevels $M_a = -J+1, -J+3, \ldots, J-1$ of the J_a level and $M_b = -J + 2, -J + 4, \ldots, J - 2$ of the J_b level. For equally strong σ^+ and σ^- fields ($\varepsilon = 0$) the MS couplings of the larger subsystem are given in Table 3.2. The smaller subsystem has the same MS couplings, except for the largest one (with $n = J$).

When J is half-integer the two independent subsystems are composed of similar sets of magnetic sublevels but with opposite signs of M. Because of this symmetry, the eigenvalues are exactly the same for both subsystems.

For $J_a = J_b = J$ the two subsystems are equivalent and they have the same eigenvalues, which are also listed in Table 3.2, for both integer and half-integer J.

The eigenstates (the MS states) are too cumbersome to be presented here, but they can easily be found for any particular J.

3.4 Conclusions

In this paper we have derived the solution of the time-dependent Schrödinger equation for the degenerate Landau-Zener model, which involves two crossing sets of degenerate energies. The states in each set interact with the sublevels of the other set but there are no direct couplings within the same set of states. A physical example is the transition between the magnetic sublevels of two levels with nonzero angular momenta induced by steady laser fields with linearly chirped frequencies.

The solution uses the Morris-Shore transformation, which decomposes the original fully coupled system into a set of independent nondegenerate two-state LZ systems and a set of decoupled, dark states. Using the known two-state LZ propagators we use the inverse transformation to obtain the propagator in the original basis.

Our results complement the Demkov-Ostrovsky model, which assumes two crossing bands

of equidistant *nondegenerate* energies. Our results also complement the bow-tie models, which also exclude degeneracies. Our derivation is simpler than in these nondegenerate models; however, the results are not so remarkably simple, as in these models, because of interferences between the different LZ propagators in the MS basis. More importantly, we have found that *not all transition probabilities exist* for an *infinite* coupling duration, because this unphysical assumption gives rise to a divergent phase in the original nondegenerate LZ model. In the latter model the transition probability is not affected because this phase is cancelled. In the present degenerate LZ model, however, these divergent phases interfere and make some of the transition probabilities undefined in the limit of infinite times. As a rule, the transition probability between any two states within the same set always exists, but between two states from different sets can only exist by accident.

Our results demonstrate that the LZ model should be used with care when multiple states are involved. In real physical situations the lesser known Allen-Eberly-Hioe model [53, 58] can be a viable alternative, particularly in the presence of degeneracies, because it involves a pulse-shaped interaction, and hence no phase divergence.

Table 3.1: Coefficients of the MS basis states (3.31) for the $J_a = 2 \leftrightarrow J_b = 1$ transition. The values for arbitrary elliptical polarization ε are in the second column, and those for a linear polarization $\varepsilon = 0$ in the third column. The relevant normalization coefficient ν for elliptical polarization is listed after each group of coefficients.

	arbitrary ε	$\varepsilon = 0$
d'_{-2}	$\nu_d\,(1-\varepsilon)$	$\sqrt{\frac{1}{8}}$
d'_{0}	$-\nu_d\sqrt{6\,(1-\varepsilon^2)}$	$-\sqrt{\frac{3}{4}}$
d'_{2}	$\nu_d\,(1+\varepsilon)$	$\sqrt{\frac{1}{8}}$
ν_d^{-2}	$4\,(2-\varepsilon^2)$	
$a'_{-2,1}$	$-\frac{1}{2}\nu_{1a}\,(1+\varepsilon)\left(1-6\varepsilon-\sqrt{1+24\varepsilon^2}\right)$	$\sqrt{\frac{3}{8}}$
$a'_{0,1}$	$\nu_{1a}\varepsilon\sqrt{6\,(1-\varepsilon^2)}$	$\frac{1}{2}$
$a'_{2,1}$	$\frac{1}{2}\nu_{1a}\,(1-\varepsilon)\left(1+6\varepsilon-\sqrt{1+24\varepsilon^2}\right)$	$\sqrt{\frac{3}{8}}$
ν_{1a}^{-2}	$\sqrt{1+24\varepsilon^2}\left[(1+\varepsilon^2)\sqrt{1+24\varepsilon^2}+(11\varepsilon^2-1)\right]$	
$a'_{-2,2}$	$-\frac{1}{2}\nu_{2a}\,(1+\varepsilon)\left(1-6\varepsilon+\sqrt{1+24\varepsilon^2}\right)$	$-\sqrt{\frac{1}{2}}$
$a'_{0,2}$	$\nu_{2a}\varepsilon\sqrt{6\,(1-\varepsilon^2)}$	0
$a'_{2,2}$	$\frac{1}{2}\nu_{2a}\,(1-\varepsilon)\left(1+6\varepsilon+\sqrt{1+24\varepsilon^2}\right)$	$\sqrt{\frac{1}{2}}$
ν_{2a}^{-2}	$\sqrt{1+24\varepsilon^2}\left[(1+\varepsilon^2)\sqrt{1+24\varepsilon^2}-(11\varepsilon^2-1)\right]$	
$b'_{-1,1}$	$\nu_b\sqrt{\sqrt{1+24\varepsilon^2}+5\varepsilon}$	$\sqrt{\frac{1}{2}}$
$b'_{1,1}$	$\nu_b\sqrt{\sqrt{1+24\varepsilon^2}-5\varepsilon}$	$\sqrt{\frac{1}{2}}$
$b'_{-1,2}$	$\nu_b\sqrt{\sqrt{1+24\varepsilon^2}-5\varepsilon}$	$\sqrt{\frac{1}{2}}$
$b'_{1,2}$	$-\nu_b\sqrt{\sqrt{1+24\varepsilon^2}+5\varepsilon}$	$-\sqrt{\frac{1}{2}}$
ν_b^{-2}	$2\sqrt{1+24\varepsilon^2}$	

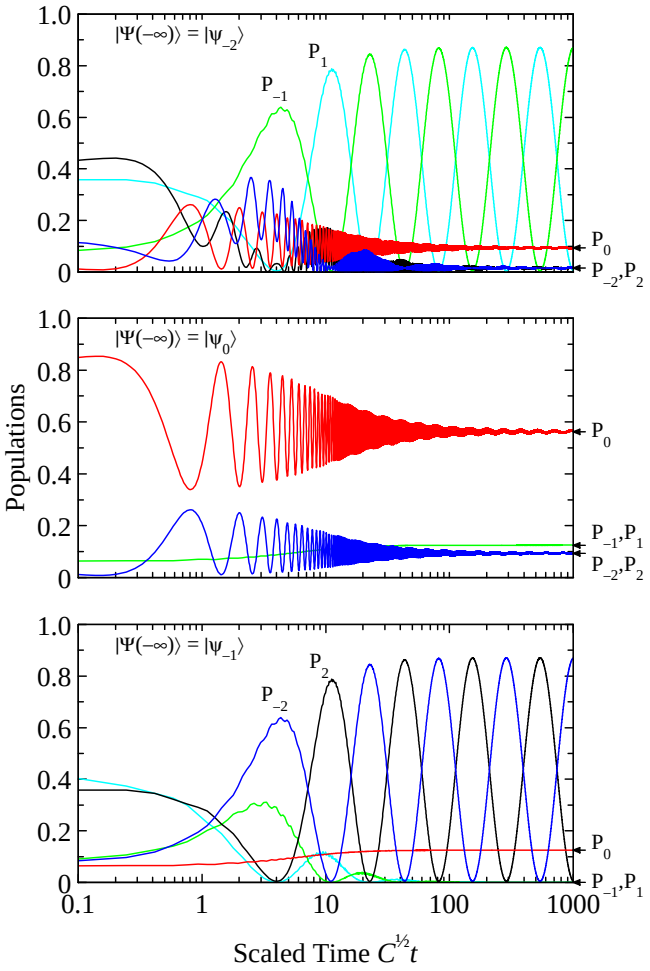

Figure 3.3: Time evolution of the populations in a five-state M system formed of the magnetic sublevels $M = -2, 0, 2$ of the $J = 2$ level and $M = -1, 1$ of the $J = 1$ level, for linear polarization ($\varepsilon = 0$), in the cases when the system starts in (i) top: state $|-2\rangle$ of the $J = 2$ level; (ii) middle: state $|0\rangle$ of the $J = 2$ level; (iii) bottom: state $|-1\rangle$ of the $J = 1$ level. The arrows on the right indicate the asymptotic values at $t \to \infty$, wherever applicable. The chirp rate C is used to define the time and frequency scales. The coupling is $\Omega = 5C^{1/2}$, which implies that the adiabatic condition ($\xi = 2.5\pi \gg 1$) is fulfilled and the adiabatic solution (3.34) applies. The initial time of the integration is $t_i = -400C^{-1/2}$.

Table 3.2: Morris-Shore couplings for transitions with $J_a = J$ and $J_b = J - 1$ or J for polarization $\varepsilon = 0$.

$J_a = J$ and $J_b = J - 1$	$J_a = J_b = J$
integer J	integer J
$\lambda_n = \Omega\sqrt{\frac{2n(2J-n)}{J(2J+1)}}$	$\lambda_n = \Omega\frac{2n}{\sqrt{2J(J+1)}}$
$(n = 0, 1, \ldots, J)$	$(n = 0, 1, \ldots, J)$
half-integer J	half-integer J
$\lambda_n = \Omega\sqrt{\frac{2n(2J-n)}{J(2J+1)}}$	$\lambda_n = \Omega\frac{2n+1}{\sqrt{2J(J+1)}}$
$(n = 0, 1, \ldots, J - 1/2)$	$(n = 0, 1, \ldots, J - 1/2)$

Chapter 4

Coherent Strong-Field Control of Multiple States by a Single Chirped Femtosecond Laser Pulse

In this chapter we present an experiment on coherent selective population of particular quantum states of Sodium atom performed by an intensive femtosecond laser. The selectivity relies on a single parameter – the chirp.

4.1 Pulse Shaping Techniques

In this section some basic properties of femtosecond laser pulses are summarized, particularly the linear properties of ultrashort light pulses. In order to describe and manage the dispersion effects, responsible for dramatic effects, a mathematical description of an ultrashort laser pulse is given first before we continue with methods how to change the temporal shape via the frequency domain.

4.1.1 Descriptive Introduction

Assuming the light field to be linearly polarized, we may write the real electric field strength $E(t)$ as a scalar quantity whereas a harmonic wave is multiplied with a temporal amplitude or envelope function $A(t)$

$$E(t) = A(t)\cos\left(\Phi_0 + \omega_0 t\right) \tag{4.1}$$

with ω_0 being the carrier circular (or angular) frequency. For simple envelope functions the pulse duration Δt is usually defined by the FWHM (full width at halfmaximum) of the temporal

intensity function $I(t)$

$$I(t) = \frac{1}{2}\varepsilon_0 cnA(t)^2 \tag{4.2}$$

with ε_0 being the vacuum permittivity, c the speed of light and n the refractive index. The factor $1/2$ arises from averaging the oscillations. In general Φ_0 is termed the absolute phase or carrier envelope phase and determines the temporal relation of the pulse envelope with respect to the underlying carrier oscillation. We may add an additional time dependent phase function $\Phi_a(t)$ to the temporal phase term in (4.1)

$$\Phi(t) = \Phi_0 + \omega_0 t + \Phi_a(t) \tag{4.3}$$

and define the momentary or instantaneous light frequency $\omega(t)$ as

$$\omega(t) = \frac{d\Phi(t)}{dt} = \omega_0 + \frac{d\Phi_a(t)}{dt}. \tag{4.4}$$

This additional phase function describes variations of the frequency in time, called a chirp. If $\Phi_a(t) = at^2$, then the detuning is linearly changing in time. For $a > 0$ ($a < 0$) we have a linear upchirp (down-chirp). Below we focus on linear optical effects where the spectrum of the pulse is unchanged and changes in the temporal pulse shape are due to manipulations in the frequency domain.

4.1.2 Mathematical Description

In linear optics the superposition principle holds and the realvalued electric field $E(t)$ of an ultrashort optical pulse at a fixed point in space has the Fourier decomposition into monochromatic waves

$$E(t) = \frac{1}{2\pi}\int_{-\infty}^{\infty} \tilde{E}(\omega)e^{i\omega t}\mathrm{d}t. \tag{4.5}$$

The, in general, complex-values spectrum $\tilde{E}(\omega)$ is obtained by the Fourier inversion theorem

$$\tilde{E}(\omega) = \int_{-\infty}^{\infty} E(t)e^{-i\omega t}\mathrm{d}\omega. \tag{4.6}$$

Since $E(t)$ is real-valued $\tilde{E}(\omega)$ is Hermitian, i.e., obeys the condition

$$\tilde{E}(\omega) = \tilde{E}^*(-\omega) \tag{4.7}$$

where * denotes complex conjugation. Hence knowledge of the spectrum for positive frequencies is sufficient for a full characterization of a light field without dc component we can define the positive part of the spectrum as

$$\tilde{E}^+(\omega) = \tilde{E}(\omega) \quad \text{for } \omega \geq 0$$
$$0 \quad \text{for } \omega < 0$$

The negative frequency part of the spectrum $\tilde{E}^-(\omega)$ is defined as

$$\tilde{E}^-(\omega) = \tilde{E}(\omega) \quad \text{for } \omega < 0$$
$$0 \quad \text{for } \omega \geq 0$$

We separate the Fourier transform integral of $E(t)$ into two parts. The complex-valued temporal function $E^+(t)$ contains only the positive frequency segment of the spectrum. By definition $E^+(t)$ and $\tilde{E}^+(\omega)$, as well as $E^-(t)$ and $\tilde{E}^-(\omega)$ are Fourier pairs where only the relations for the positive-frequency part are given as

$$E^+(t) = \frac{1}{2\pi}\int_{-\infty}^{\infty} \tilde{E}^+(\omega)e^{i\omega t}\mathrm{d}\omega \tag{4.8}$$
$$\tilde{E}^+(\omega) = \int_{-\infty}^{\infty} E^+(t)e^{-i\omega t}\mathrm{d}\omega. \tag{4.9}$$

These quantities relate to the real electric field

$$E(t) = E^+(t) + E^-(t) = 2\mathrm{Re}E^+(t) = 2\mathrm{Re}E^-(t) \tag{4.10}$$

and it's complex Fourier transform

$$\tilde{E}(\omega) = \tilde{E}^+(\omega) + \tilde{E}^-(\omega). \tag{4.11}$$

$E^+(t)$ is complex-valued and can therefore be expressed uniquely in terms of it's amplitude and phase

$$E^+(t) = \left|E^+(t)\right| e^{i\Phi(t)} = \left|E^+(t)\right| e^{i\Phi_0}e^{i\omega_0 t}e^{i\Phi_a(t)} \tag{4.12}$$

The envelope function $A(t)$ is given by

$$A(t) = 2\left|E^+(t)\right| = 2\left|E^-(t)\right| = 2\sqrt{E^+(t)E^-(t)}. \tag{4.13}$$

The complex positive-frequency part $\tilde{E}^+(\omega)$ can be analogously decomposed into amplitude and phase

$$\tilde{E}^+(\omega) = \left|\tilde{E}^+(\omega)\right| e^{-i\phi(\omega)} = \sqrt{\frac{\pi}{\varepsilon_0 cn}I(\omega)}e^{-i\phi(\omega)} \tag{4.14}$$

where $\left|\tilde{E}^+(\omega)\right|$ is the spectral amplitude, $\phi(\omega)$ is the spectral phase and $I(\omega)$ is the spectral intensity. From (4.7) the relation $\phi(\omega) = -\phi(-\omega)$ is obtained. It is precisely the manipulation of this spectral phase $\phi(\omega)$ in the experiment which – by virtue of the Fourier transformation

(4.9) – creates changes in the real electric field strength $E(t)$ without changing $I(\omega)$. If the spectral intensity $I(\omega)$ is manipulated as well, additional degrees of freedom are accessible for generating temporal pulse shapes at the expense of lower energy. The temporal phase $\Phi(t)$ contains frequency-versus-time information, leading to the definition of the instantaneous frequency $\omega(t)$.

Usually the spectral amplitude is distributed around a center frequency (or carrier frequency) ω_0 . Therefore – for well-behaved pulses – it is often helpful to expand the spectral phase into a Taylor series

$$\phi(\omega) = \sum_{j=0}^{\infty} \frac{\phi^{(j)}\omega_0}{j!} (\omega - \omega_0)^j = \phi(\omega_0) + \phi'(\omega_0)(\omega - \omega_0) + \frac{1}{2}\phi''(\omega_0)(\omega - \omega_0)^2 + \dots \tag{4.15}$$

The spectral phase coefficient of zeroth order describes in the time domain the absolute phase ($\Phi_0 = -\phi(\omega_0)$). The first-order term leads to a temporal translation of the envelope of the laser pulse in the time domain (the Fourier shift theorem) but not to a translation of the carrier. A positive $\phi'(\omega_0)$ corresponds to a shift towards later times. The coefficients of higher order are responsible for changes in the temporal structure of the electric field. The minus sign in front of the spectral phase in (4.12) is chosen so that a positive $\phi''(\omega_0)$ corresponds to a linearly up-chirped laser pulse.

There is a variety of analytical pulse shapes where this formalism can be applied to get analytical expression in both domains. Below we focus on a Gaussian laser pulse $E^+_{in}(t)$ with a corresponding spectrum $E^+_{in}(\omega)$. Phase modulation in the frequency domain leads to a spectrum $E^+_{out}(\omega)$ with a corresponding electric field $E^+_{out}(t)$. The input pulse we write as

$$E^+_{in}(t) = \frac{E_0}{2} e^{-2\ln 2 \frac{t^2}{\Delta t^2}} e^{i\omega_0 t}. \tag{4.16}$$

Here Δt denotes the FWHM of the corresponding intensity $I(t)$. The absolute phase is set to zero, the carrier frequency is set to ω_0, additional phase terms are set to zero as well. The pulse is termed an unchirped pulse in the time domain. For $\tilde{E}^+_{in}(\omega)$ we obtain the spectrum

$$\tilde{E}^+_{in}(\omega) = \frac{E_0 \Delta t}{2} \sqrt{\frac{\pi}{2\ln 2}} e^{-\frac{\Delta t^2}{8\ln 2}(\omega - \omega_0)^2}. \tag{4.17}$$

One feature of Gaussian laser pulses is that adding the quadratic term $\frac{1}{2}\phi''(\omega_0)(\omega - \omega_0)^2$ to the spectral phase function also leads to a quadratic term in the temporal phase function and therefore to linearly chirped pulses. The complex fields for such laser pulses are given by

$$\tilde{E}^+_{out}(\omega) = \frac{E_0 \Delta t}{2} \sqrt{\frac{\pi}{2\ln 2}} e^{-\frac{\Delta t^2}{8\ln 2}(\omega - \omega_0)^2} e^{-\frac{i}{2}\phi''(\omega_0)(\omega - \omega_0)^2} \tag{4.18}$$

$$E^+_{out}(t) = \frac{E_0}{2\gamma^{\frac{1}{4}}} e^{-\frac{t^2}{4\beta\gamma}} e^{i\omega_0 t} e^{i(at^2 - \varepsilon)} \tag{4.19}$$

with

$$\beta = \frac{\Delta t_{in}^2}{8\ln 2}, \quad \gamma = 1 + \frac{\phi''^2}{4\beta^2}, \quad a = \frac{\phi''}{8\beta^2\gamma}, \quad \varepsilon = \frac{1}{2}\arctan\left(\frac{\phi''}{2\beta}\right) = -\Phi_0 \tag{4.20}$$

For the pulse duration Δt_{out} (FWHM) of the linearly chirped pulse (quadratic temporal phase function at^2) we obtain the convenient formula

$$\Delta t_{out} = \sqrt{\Delta t^2 + \left(4\ln 2 \frac{\phi''}{\Delta t}\right)^2}. \tag{4.21}$$

4.2 Experiment

In the experiment, we combine spectral phase shaping to produce chirped ultrashort laser pulses with the measurement of PADs resulting from REMPI of sodium atoms, employing the VMI technique. In this section, we first introduce the sodium excitation scheme with emphasis on the different accessible excitation and ionization pathways. Then we describe the experimental setup and layout of our photoelectron imaging spectrometer.

4.2.1 Excitation Scheme

Fig. 4.1 shows the excitation and ionization scheme of sodium atoms based on energy level information taken from the NIST-database [25]. Different multi-photon excitation pathways are accessible during the interaction of sodium atoms with intense ultrashort laser pulses (laser specifications are given in Sec. 4.2.2). The predominant excitation pathway is a 2+1+1 REMPI process via the two-photon transition $4s \leftarrow\leftarrow 3s$ (red arrows in Fig. 4.1) which is nearly resonant with our laser spectrum [26]. Consequential population of states $5p$, $6p$ and $7p$ gives rise to photoelectron wave packets in the ionization continuum having s or d-symmetry. The recorded PADs therefore exhibit a combined s and d-symmetry and are measured at the distinct kinetic energies 0.76 eV, 1.04 eV and 1.20 eV, corresponding to states $5p$, $6p$ and $7p$ respectively. Alternatively, a 3+1 REMPI process (green arrows in Fig. 4.1) based on three-photon absorption from the $3s$ ground state with no intermediate resonances is taken into account, contributing also to the population of states $5p$, $6p$ and $7p$ but, in addition, transferring population to states $5f$ and $6f$. One-photon ionization of the latter results in photoelectron wave packets with d and g-symmetry at kinetic energies 1.02 eV and 1.18 eV respectively. These photoelectrons are distinguished from the p state contributions (at 1.04 eV and 1.20 eV) by the symmetry of their angular distributions. In the following we will refer to the different photoelectron contributions as different *energy channels* at nominal kinetic energies of 0.8 eV, 1.0 eV and

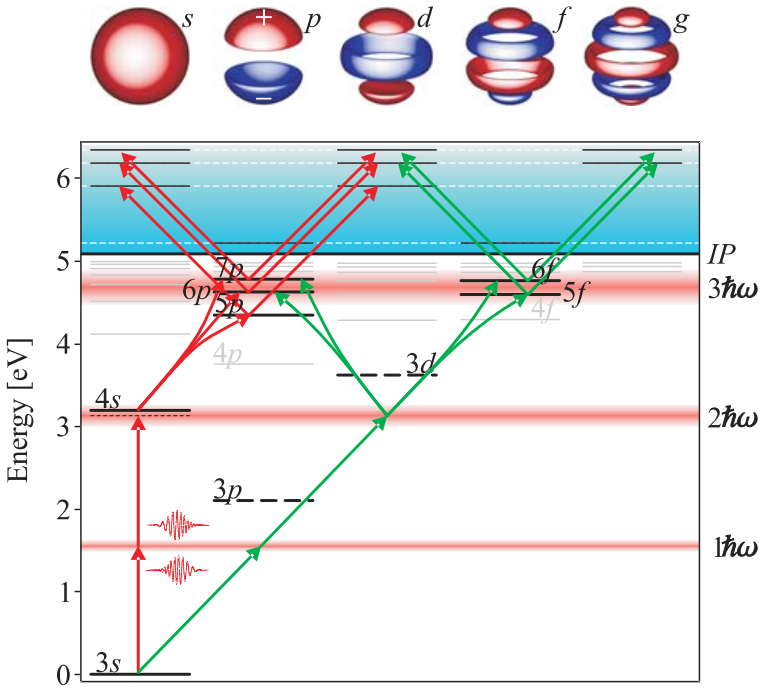

Figure 4.1: Excitation and ionization scheme of sodium atoms illustrating the excitation pathways that arise during the interaction with an intense 795 nm, 30 fs FWHM laser pulse. These pathways comprise a 2+1+1 REMPI (red arrows) and a 3+1 REMPI (green arrows) process from the $3s$ ground state as well as a two-photon ionization process from state $3p$ (blue arrows). Blurred red bars represent the one, two and three-photon spectrum of our laser respectively. Since state $4s$ lies within the bandwidth of the two-photon spectrum, the laser strongly drives the transition $4s \leftarrow\leftarrow 3s$. Once state $4s$ is populated, population flows to states $5p$, $6p$ and $7p$, giving rise to photoelectron wave packets with combined s and d-symmetry at characteristic kinetic energies 0.76 eV, 1.04 eV and 1.20 eV in the ionization continuum. A competing excitation pathway is opened up by three-photon absorption leading to population of states $5f$ and $6f$ in addition. Photoelectrons from this excitation channel are characterized by a combined d and g-symmetry of the measured PADs at kinetic energies 1.02 eV and 1.18 eV respectively. Two-photon ionization from the non-resonant, transiently populated state $3p$ results in photoelectron wave packets at about 0.2 eV, having combined p and f-symmetry. For illustrative purposes, the relevant symmetries of the released photoelectron wave packets are visualized on top of the figure in red and blue, encoding the positive and negative sign of the electron wave function respectively.

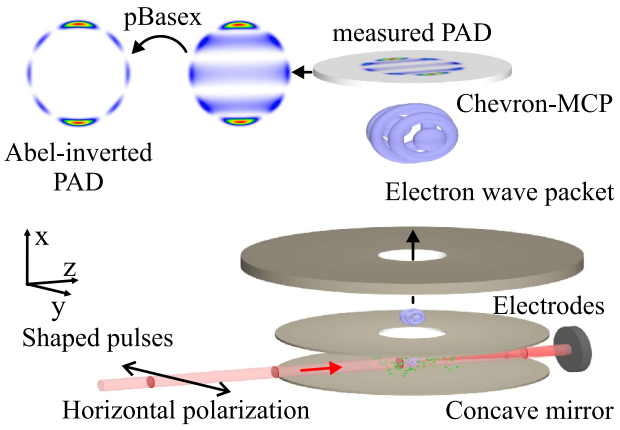

Figure 4.2: Experimental setup. Horizontally polarized femtosecond laser pulses are sent into a vacuum chamber and refocused by a 50 mm on-axis concave mirror into sodium vapor provided by an alkali metal dispenser source (not shown). Photoelectrons emitted by the light-atom interaction are projected towards a position sensitive MCP-detector using the VMI method. The amplified signal is recorded by a 1.4 million pixels camera-system and sent to a computer. An Abel-inversion is performed using the pBasex-algorithm.

1.2 eV, and infer their origin, i.e. the excitation pathway, from the *angular* distribution. Both multi-photon excitation pathways proceed via the intermediate, non-resonant state $3p$, which is only transiently populated. However, since ionization takes place *during* the excitation also photoelectrons from this state are detected at low kinetic energies around 0.2 eV (blue arrows in Fig. 4.1). For more details see caption of Fig. 4.1.

4.2.2 Setup

In this section the experimental setup comprising the laser system and the photoelectron imaging spectrometer is described. Intense 795 nm, 30 fs FWHM (Full Width at Half Maximum) laser pulses provided by an amplified 1 kHz Ti:sapphire laser system (*Femtolasers Femtopower Pro*) were phase modulated in frequency domain by a home-built pulse shaper [27], applying quadratic phase masks of the form $\varphi_{mod}(\omega) = \varphi_2/2 \cdot (\omega - \omega_0)^2$, where ω_0 is the central frequency of our laser spectrum [28]. The chirp parameter φ_2 was varied in the range from -2000 fs^2 to $+2000$ fs^2 in steps of $\Delta\varphi_2 = 100$ fs^2. The chirped output pulses of 12 μJ energy were sent into a vacuum chamber and refocussed by a concave mirror (5 cm focal length; we estimated a *peak* intensity of about 10^{13} W/cm^2 for the bandwidth-limited pulse) into sodium vapor supplied by an alkali metal dispenser source, as shown in Fig. 4.2. Photoelectrons released during the

strong-field interaction of the shaped pulses with single atoms were detected by a photoelectron imaging spectrometer using the VMI method. In order to compensate the residual chirp of the unmodulated pulse, we performed an *in situ* adaptive optimization of the multi-photon ionization of water vapor background (about 4×10^{-7} mbar) in the interaction region of the spectrometer. The resulting optimal compensation phase was additionally applied to the pulse shaper during the experiments, ensuring an error in the chirp parameter φ_2 of less than 150 fs^2. The energy calibration of the imaging spectrometer was performed using a 3+1 REMPI of xenon atoms excited by a Nd:YAG ns laser system at 355 nm, achieving a spectrometer resolution of 60 meV at 0.5 eV. Employing the energy calibrated photoelectron imaging spectrometer we studied angular and energy resolved photoelectron spectra as a function of the chirp parameter φ_2.

4.3 Experimental Results and Discussion

Figure 4.3 (upper row) shows measured PADs from REMPI of sodium atoms with chirped fs laser pulses for three exemplary values of the chirp parameter φ_2. The middle row displays the corresponding Abel-inverted (retrieved) PADs obtained by employing the pBasex-algorithm [29, 30]. When PADs arise from ionization with polarization shaped pulses [31], direct tomography methods have been developed for three-dimensional reconstruction of ultrashort free photoelectron wave packets [32]. Angular sections through the retrieved PADs at kinetic energies 0.8 eV, 1.0 eV and 1.2 eV, as plotted in the lower row, serve to identify the symmetry of the different energy channels observed in the PADs. The PAD measured for the unmodulated, i.e., bandwidth-limited pulse is depicted in the central column. Three major contributions are observed at kinetic energies 0.8 eV, 1.0 eV and 1.2 eV, related to the energy channels discussed above (cf. Sect. 4.2.1). The angular section taken at 1.2 eV exhibits two minor nodes between 0° and 180°, i.e. *d*-symmetry. This channel is attributed mainly to ionization via state $7p$ (red excitation pathway in Fig. 4.1), though our numerical simulations (inset of Fig. 4.4) indicate, that also ionization via state $6f$ (green excitation pathway in Fig. 4.1) delivers a minor contribution. The contribution of an *s*-wave to this channel, as expected from the excitation scheme Fig. 4.1, is reflected in the *weak* equatorial signal: At an angle of 90° *s* and *d*-wave have opposite sign and, thus, interfere destructively, whereas at the poles, i.e. at 0° and 180°, both waves add up constructively. The section taken at 1.0 eV exhibits 4 nodes between 0° and 180°, corresponding to *g*-symmetry. This contribution originates predominantly from ionization via state $5f$. The observation that the lobe at 90° (and 270° respectively) is

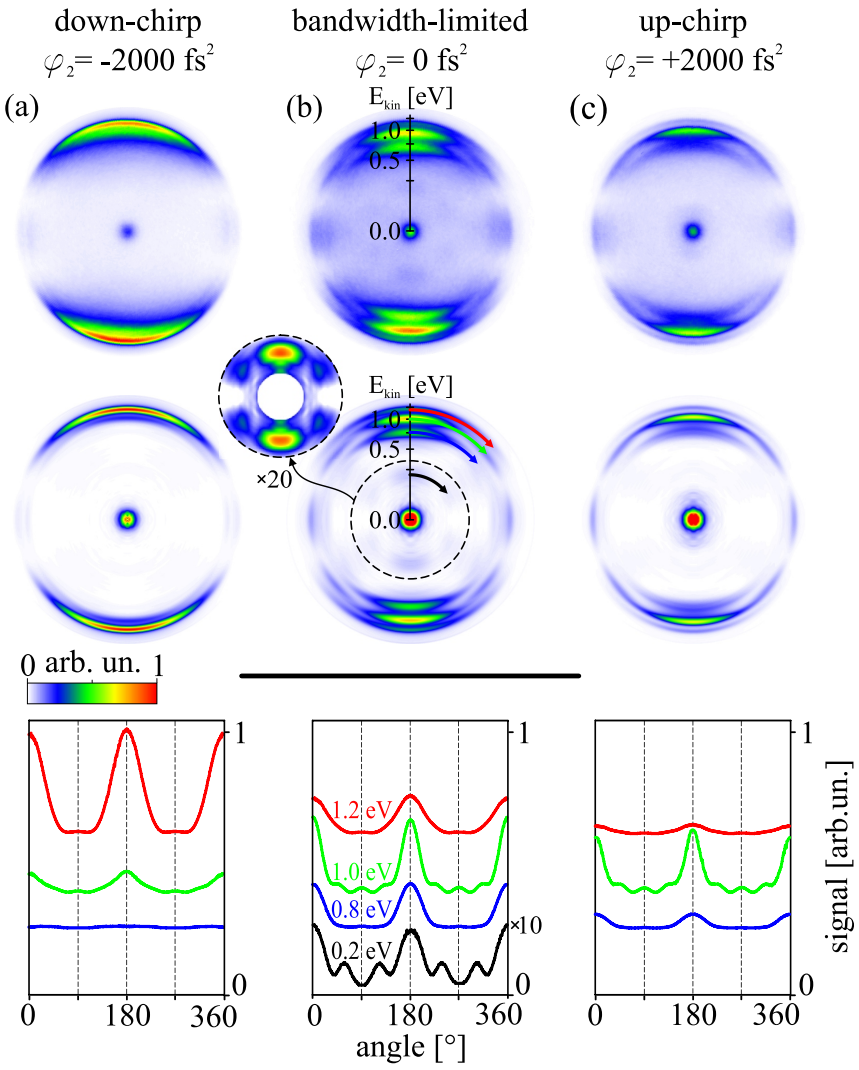

Figure 4.3: Measured PADs from excitation and ionization of sodium atoms using both chirped and bandwidth-limited fs laser pulses. In the upper row measured PADs for different values of the chirp parameter φ_2 are shown. (a) $\varphi_2 = -2000$ fs^2 (down-chirp). (b) $\varphi_2 = 0$ (bandwidth-limited). (c) $\varphi_2 = +2000$ fs^2 (up-chirp). All images are scaled to the same maximum value. The middle row contains the corresponding Abel-inverted PADs obtained using the pBasex-algorithm. Angular sections through the retrieved PADs at kinetic energies of about 0.2 eV, 0.8 eV, 1.0 eV and 1.2 eV (lower row) reveal the symmetries of the observed contributions and shed light on the underlying ionization pathways. The signal offsets are introduced for better visibility.

slightly lowered with respect to its two neighbors indicates a weak d-wave contribution interfering destructively with the g-wave in this angular segment. The contribution measured at 0.8 eV shows again combined s and d-symmetry and is ascribed to ionization via state $5p$.

Moreover, a weak contribution is observed at about 0.2 eV, a magnification of which is shown in the inset of Fig. 4.3(b). The nodal structure of this signal exhibits distinct f-symmetry. However, the pronounced poles of the PAD as well as the fact, that the nodes at 45° and 135° in the angular section are raised with respect to the node at 90° give a hint on a p-wave contribution to the photoelectron signal. Observation of photoelectron wave packets with combined p and f-symmetry close to the ionization threshold is consistent with two-photon ionization from state $3p$ (blue pathway in Fig. 4.1). Note, that state $3p$ is—although non-resonant—transiently populated during the interaction, mediating the multi-photon processes to the state $4s$ and the high lying f states.

For large negative values of φ_2 (left column in Fig. 4.3), i.e. strongly *down*-chirped laser pulses, the outer channel at kinetic energy 1.2 eV is considerably enhanced in comparison to the bandwidth-limited case, whereas the intermediate channel at 1.0 eV is strongly reduced and the two innermost contributions have essentially vanished. Note the change in symmetry of the intermediate channel which exhibits combined s and d-symmetry in this case, indicating more efficient ionization from state $6p$, while the $5f$ contribution is very small. Changing the sign of φ_2, i.e. using strongly *up*-chirped laser pulses (right column in Fig. 4.3), suppresses the high energy channel in favor of the intermediate channel at 1.0 eV which dominates the PAD in this case. From its angular section at 1.0 eV we find a combined d and g-symmetry, as in the bandwidth-limited case. This contribution is therefore traced back mainly to state $5f$. The finding that the symmetry of photoelectrons from the intermediate channel alters from d to g is rationalized by the change of the ordering of red and blue frequency components within the chirped pulse. For a down-chirped pulse, i.e. when the blue components arrive first, initially, the system is in resonance with the two-photon transition $4s \leftarrow\leftarrow 3s$ implying efficient ionization via the p states (red pathway in Fig. 4.1). On the other hand, up-chirped pulses favor ionization via state $5f$ since at early times the system is in resonance with the three-photon transition $5f \leftarrow\leftarrow\leftarrow 3s$ (green pathway in Fig. 4.1). Such processes have also been observed in [33] under different excitation conditions.

In order to provide the full picture of the chirp dependent population flow to the different energy channels, we performed an angular integration of all 41 measured PADs and present the resulting energy-resolved photoelectron spectra in terms of a two-dimensional map as a function of the kinetic energy and the chirp parameter φ_2. The result obtained upon variation

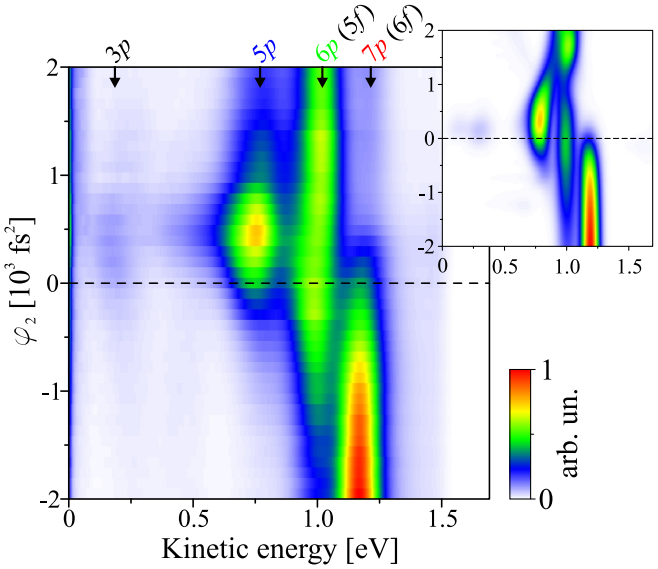

Figure 4.4: Measured photoelectron kinetic energy distributions as a function of the chirp parameter φ_2. The data were obtained by angular integration of the retrieved PADs. Three main energy channels are observed at 0.8 eV, 1.0 eV and 1.2 eV, each of which can be activated by appropriate choice of the chirp parameter. For $\varphi_2 \ll 0$, i.e. strongly down-chirped laser pulses, photoelectrons with high kinetic energies related to the high lying states $7p$ (and minor $6f$ contribution) are produced. The intermediate channel at 1.0 eV, related to states $6p$ and $5f$, is addressed by strongly up-chirped laser pulses with $\varphi_2 \gg 0$. Photoelectrons with kinetic energies around 0.8 eV, corresponding to state $5p$, are favored at small positive values of φ_2, i.e. high laser pulse peak intensities. The weak contribution at 0.2 eV in the same φ_2-region stems from ionization of the non-resonant state $3p$. The inset shows results from a numerical simulation of the multi-photon excitation and ionization process.

of φ_2 in the range from -2000 fs^2 to $+2000$ fs^2 is displayed in Fig. 4.4. The three major channels at 0.8 eV, 1.0 eV and 1.2 eV are clearly visible. Note, that for e.g. rare gas atoms under our experimental conditions ponderomotive shifts of more than 0.5 eV are calculated. No such shifts are observed in the experiment, since the high-frequency approximation [34, 35] (necessary condition for the application of the ponderomotive energy concept) is not valid for alkalis excited by near infrared laser radiation. An analysis of the neutral excitation dynamics behind the observed contributions will be given in Sec. 4.4. The map illustrates the above statements, that for large negative values of φ_2 the high energy channel at 1.2 eV is addressed with high efficiency, i.e. a down-chirped pulse steers the population predominantly towards the high lying state $7p$. For large positive chirps the intermediate channel is selectively addressed, corresponding to predominant population of states $6p$ and $5f$. The low energy channel is accessed most efficiently in the vicinity of $\varphi_2 = 500$ fs^2. In fact, in the regime $0 \leq \varphi_2 \leq 1000$ fs^2 the photoelectron spectrum is made up of contributions from states $5p$, $6p$ and $5f$. Because the excitation (and simultaneous ionization) takes place on an ultrashort time scale precluding decoherence processes, a *coherent* superposition of states $5p$, $6p$ and $5f$ is excited in this chirp regime. Upon changing the sign of φ_2, i.e. for -1000 fs$^2 \leq \varphi_2 \leq 0$, the laser pulse induces a coherent superposition of states $6p$, $5f$ and $7p$. Photoelectrons observed at about 0.2 eV for moderate positive chirps are attributed to two-photon ionization from state $3p$.

The inset to Fig. 4.4 shows results from a numerical simulation of the simultaneous multi-photon excitation and ionization process. The calculations are based on numerical integration of the time-dependent Schrödinger-equation for a neutral 20-state system (comprising those states labeled in Fig. 4.1 and taking the fine structure splitting into account) interacting with an intense chirped 795 nm, 30 fs FWHM Gaussian input pulse. One-photon ionization from the high lying p and f states is treated within a simplified model employing first order perturbation theory. We assume a flat continuum and unit coupling elements with no additional phases for all bound-free transitions. A more rigorous treatment of the ionization step involving the determination of radial coupling matrix elements also for the bound-free transitions is provided by, e.g., single-channel quantum defect theory [36] as reported for instance in [37, 38]. In order to model the two-photon ionization from state $3p$ proceeding, for example, via state $3d$ as indicated by the blue pathway in Fig. 4.1, we employed second order perturbation theory. For a more detailed description of our method see [28, 39, 40]. The simulation of photoelectron spectra reproduces the main features of the experimental results very well. This allows us to look into the underlying *neutral* excitation dynamics and follow the population flow within the bound atomic system. We find that for *large negative chirp* φ_2 state $7p$ is addressed almost

selectively, while for large positive φ_2 values both states $6p$ and $5f$ are populated efficiently in equal measure. The latter is in accordance with the experimental observation of the PAD with pronounced g-symmetry in the intermediate channel at 1.0 eV for *large positive chirp* (see Fig. 4.3(c)). The most efficient excitation of state $5p$ occurs for *moderate positive chirp*. However, in this chirp regime states $6p$ and $5f$ receive comparable population confirming the observation of a PAD with a contribution of g-symmetry at 1.0 eV and *zero chirp*. At *moderate negative chirp*, we obtain a coherent superposition of states $6p$, $5f$ and $7p$. Note that the weak contribution around 0.2 eV and small positive values of φ_2 observed in the experiment (shown in the inset to Fig. 4.3(b)) is also reproduced in the simulation. Within the framework of our simulation, these photoelectrons are ascribed to two-photon ionization from state $3p$ which receives non-perturbative *transient* population. We note, that in a perturbative regime, ionization from this transiently populated state could be interpreted as a transition from a *virtual* state.

In the next section, we will further investigate the neutral population dynamics by means of a reduced atomic system in order to rationalize the general features observed in the experiment in terms of physical mechanisms governing the excitation process.

4.4 Theoretical Model

In this section we provide a mainly qualitative description of the system at hand. To this end, we assume that the photoelectron signal arises most significantly through the 2+1+1 REMPI channel (red pathway in Fig. 4.1), involving the five states $3s$, $4s$, $5p$, $6p$ and $7p$. The idea of this reduction is to demonstrate the basic principles influencing the dynamics of the whole system, which become more transparent in this simplified model, involving the most significant states for our experiment. In this approach, we adiabatically eliminated state $3p$ [41–43] because it is off resonance and receives smaller transient population than the other coupled states. Its presence, though, affects the population dynamics significantly for it induces strong dynamic Stark-shifts in the energies of states $3s$ and $4s$, which substantially modify the energy diagram.

The quantum dynamics of this five-state system obeys the time-dependent Schrödinger equation

$$i\hbar\frac{d}{dt}\mathbf{c}(t) = \hat{H}(t)\mathbf{c}(t). \tag{4.22}$$

The Hamiltonian $\hat{H}(t)$ in the rotating-wave approximation, rotating with the instantaneous

laser frequency $\omega(t) = \omega_0 + 2at$ (see Eq. (4.33) in the appendix), is given by [41, 43]:

$$\hat{H}(t) = \hbar \begin{bmatrix} \Delta_1 - S_1 & \frac{1}{2}\Omega_{12} & 0 & 0 & 0 \\ \frac{1}{2}\Omega_{12} & \Delta_2 - S_2 & \frac{1}{2}\Omega_{23} & \frac{1}{2}\Omega_{24} & \frac{1}{2}\Omega_{25} \\ 0 & \frac{1}{2}\Omega_{23} & \Delta_3 & 0 & 0 \\ 0 & \frac{1}{2}\Omega_{24} & 0 & \Delta_4 & 0 \\ 0 & \frac{1}{2}\Omega_{25} & 0 & 0 & \Delta_5 \end{bmatrix}. \tag{4.23}$$

Here the explicit time dependence is dropped for ease of notation. The normalized vector $\mathbf{c}(t) = [c_1(t), c_2(t), \ldots, c_5(t)]^T$ consists of the amplitudes of the five states, ordered as shown above, which are obtained by numerical integration of the Schrödinger-equation (4.22), the respective populations are $P_n(t) = |c_n(t)|^2$, $\Delta_n(t) = \omega_n - k\,\omega(t)$ are the generally time-dependent atom-laser detunings, where ω_n are the atomic state eigenfrequencies, with ω_{3s} taken as zero, k is the transition order, $\Omega_{2n} = d_{2n}\Omega_0 f(t)$ represent the one-photon couplings of state 2 to state n ($n = 3, 4, 5$), $\Omega_{12} = q_{12}\Omega_0^2 f^2(t)$ is the two-photon coupling between states 1 and 2, with $f(t)$ being the chirped laser electric field envelope, d_{mn} are the relevant transition dipole moments in atomic units, q_{12} is the effective two-photon transition moment (cf. Eq. (4.25)) and S_1 and S_2 represent the DSS of states 1 and 2, respectively,

$$S_1 = \frac{\Omega_{3s3p}^2}{4\Delta_{3p}}, \quad S_2 = \frac{\Omega_{3p4s}^2}{4\Delta_{3p}}. \tag{4.24}$$

The effect of the DSS due to state $3d$ is neglected for it is very weakly coupled to the states whose energies it might influence: the p states are coupled about 10 times stronger to state $4s$ as compared to state $3d$; state $3d$ is not directly coupled to state $3s$, but rather through a two-photon transition. In the first two diagonal elements of the Hamiltonian (associated with the energies of states $3s$ and $4s$) the atom-laser detuning and the DSS add up to a time-dependent *effective* chirp: the former resulting from the time-dependent instantaneous laser frequency $\omega(t)$, and the latter deriving from the time-dependent shift of the level energies due to DSS.

4.4.1 Excitation Regimes

In Fig. 4.5 we distinguish five different regimes in regard to the value of the chirp φ_2. In all cases we plot the bare-state energies and analyze the dynamics by accounting for the presence of level crossings. Because it is the ionization signal that is observed in the experiment it is also important *when* a particular level crossing occurs: a level crossing at *early* time, and the ensuing adiabatic passage transition, would translate into a larger ionization signal than a *late*

crossing, where even a significant population transfer to a certain discrete state would not be reflected in the ionization signal.

Below we examine the dynamics of our system with particular interest in states $5p$, $6p$ and $7p$. In Fig. 4.5 we show the populations and the energies of the five bare states for the chirp φ_2 varied between -2000 fs^2 and 2000 fs^2 (from left to right) with the system initiated in state $3s$. For illustrative purposes we pick $\Omega_0 = 0.3$ fs^{-1}, corresponding to an intensity of 3.7×10^{12} W/cm^2 [42], and $\Delta t = 30$ fs.

Large Negative Chirp

For large negative chirp ($\varphi_2 = -2000$ fs^2, Fig. 4.5(a)) the laser field reaches resonances relative to the $7p \leftarrow 4s$ (one-photon) transition and the $4s \leftarrow\leftarrow 3s$ (two-photon) transition in nearly the same instant, thus creating a "bow-tie" level crossing pattern [41, 44–48] which is of particular significance because it involves three rather than two states. This crossing results in efficient population transfer to states $4s$ and $7p$ and depopulation of state $3s$. Because state $7p$ is populated at such early times, it is exposed to ionization for most of the interaction dynamics and hence has a dominant contribution in the photoelectron signal (see Fig. 4.4 at 1.2 eV and -2000 fs^2).

Later on we observe almost adiabatic evolution and the population is shared mainly between states $4s$ and $7p$ in the form of Rabi-oscillations with fading amplitude [49]. State $6p$ acquires only marginal population mainly due to its crossing with state $3s$ (which is, however, already depleted due to the preceding "bow-tie" crossing) via a three-photon excitation through state $4s$. The late crossings between states $3s$ and $5p$, and also between states $4s$ and $6p$ are of no importance because they occur after the pulse intensity has essentially vanished. State $5p$ remains unpopulated since it is far off-resonant throughout the entire dynamics.

Large Positive Chirp

For large positive chirps ($\varphi_2 = 2000$ fs^2, Fig. 4.5(e)) the energy diagram is mirrored compared to the one for large negative chirps φ_2 (Fig. 4.5(a)). Then initially the system evolves adiabatically, with minor (off-resonant) population transfer from state $3s$ to state $4s$ due to their strong mutual coupling. Around the time of the peak laser intensity, as state $3s$ sweeps across resonance with $6p$, the latter starts to effectively populate through the three-photon $3s - 6p$ crossing. Because this crossing occurs approximately in the middle of the laser pulse the population of state $6p$ is exposed to ionization for a considerable time interval, which results in significant photoelectron signal from $6p$ (see Fig. 4.4 at 1.0 eV and $+2000$ fs^2). For the same

reason—the $3s - 6p$ crossing occurring near the laser pulse maximum—the population transfer from state $3s$ to state $6p$ is relatively efficient and only about half of the population is left in states $3s$ and $4s$ thereafter; then only a part of this already reduced population is transferred to state $7p$ at the subsequent "bow-tie" crossing $3s - 4s - 7p$. Moreover, this crossing occurs at late times and hence state $7p$ is not visible in the photoelectron spectrum. State $5p$ remains unpopulated once again as it stays far off any resonance.

We now turn our attention to the regimes of a moderately large chirp φ_2, where the photoelectron spectrum changes from a single-state feature to one displaying double features.

Moderate Negative Chirp

For a moderate negative chirp ($\varphi_2 = -500$ fs^2, Fig. 4.5(b)) an early crossing occurs between states $3s$, $4s$ and $7p$ in the rising edge of the pulse, which leads to a partial population transfer from state $3s$ to states $4s$ and $7p$, because the laser intensity is not strong enough to enforce adiabatic evolution. The population in state $7p$ is exposed to ionization for the rest of the pulse, whereas the population in state $4s$ proceeds until the subsequent $4s - 6p$ crossing where it is partially transferred to state $6p$. The leftover temporary flows into state $5p$, which starts to emerge in the photoelectron spectrum, and is finally driven back into state $3s$. In result, all states $5p$, $6p$ and $7p$ are visible in the photoelectron signal, which is an indication for the creation of a coherent superposition of these (see Fig. 4.4 at about -500 fs^2).

Moderate Positive Chirp

For moderate positive chirps ($\varphi_2 = 500$ fs^2, Fig. 4.5(d)) state $3s$ first comes very close to state $5p$ at times of the laser pulse maximum; during this proximity the population undergoes Rabi-type oscillations between states $3s$ and $5p$ and is exposed to ionization from state $5p$. The signature of state $5p$ is clearly visible and indeed, this is the regime where this state indisputably dominates in the photoelectron signal (see Fig. 4.4 at 0.8 eV and $+500$ fs^2). In other words, it is the DSS induced by the two-photon transition $4s \leftarrow\leftarrow 3s$, which makes the population of the far-off-resonant state $5p$ possible [50]. If this Stark-shift were absent (e.g. if the two-photon transition $4s \leftarrow\leftarrow 3s$ were instead a single-photon one in a gedanken scenario) state $5p$ would never receive sizeable population. As we proceed beyond the pulse maximum state $3s$ crosses state $6p$ and the population is partially transferred to the latter. Hence state $6p$ emerges in the photoelectron signal due to the ensuing ionization, whereas state $7p$ is invisible in this regime because all population left flows into state $4s$.

Zero Chirp.

In this regime the laser pulse is unchirped, $\varphi_2 = 0$. Therefore, the *effective* chirp is entirely due to ac Stark-shift. The latter is symmetric to the pulse because it is induced by the same pulse. Moreover, because state $3s$ crosses states $6p$ and $5p$ (Fig. 4.5(c)), sizeable population will visit these two states through the respective first crossings $3s - 5p$ and $3s - 6p$. A second pair of crossings in the falling edge of the pulse will induce additional transitions $5p \leftarrow\leftarrow\leftarrow 3s$ and $6p \leftarrow\leftarrow\leftarrow 3s$. The implication is that states $5p$ and $6p$ will contribute significantly to the photoelectron signal (see Fig. 4.4 around $\varphi_2 = 0$). State $7p$, on the other hand, remains well off resonance throughout and receives only a small population due to (weak) non-resonant interaction. Its contribution to the photoelectron signal should be therefore more muted than these from states $5p$ and $6p$.

4.4.2 Discussion

Below we discuss the five excitation regimes in the dressed state (adiabatic) context. When adiabatic, which demands large couplings and low chirp rates for the avoided crossings in question, starting in state $3s$ we end up in state $7p$ for $\varphi_2 < 0$ or in state $6p$ for $\varphi_2 > 0$ (Fig. 4.5, middle frames; in the latter case a fully non-adiabatic passage across state $5p$ occurs, since the pulse intensity is negligible for the $3s - 5p$ resonance). Therefore, clearly from Fig. 4.5, our system exhibits a somewhat adiabatic behavior for chirp φ_2 away from the origin. As we get closer, the crossings shift towards the pulse wings, whereas the pulse gets narrower in time, which in combination results in breaking adiabaticity. The latter is further hindered by the increased DSS, which effectively enhances the chirp rate.

We expect adiabaticity to remain almost unaffected for large negative values of the chirp φ_2, since the chirp rate $a \propto 1/\varphi_2$ and $\Omega \propto 1/\sqrt{\varphi_2}$, and to break down for large positive values, for it relies on the three-photon transition $6p \leftarrow\leftarrow\leftarrow 3s$, which gets weaker, as the resonances relative to $3s - 4s$ and $4s - 6p$ further separate in time. Larger peak intensities Ω_0 strengthen adiabaticity for the transition $7p \leftarrow\leftarrow\leftarrow 3s$ and make complete population transfer possible, as also indicated in [51], whereas for the transition $6p \leftarrow\leftarrow\leftarrow 3s$ due to the unfavorable influence of the increased DSS we predict the contrary.

4.5 Summary and Conclusion

In this contribution we presented a joint experimental and theoretical study on strong-field Resonance Enhanced Multi-Photon Ionization (REMPI) of sodium atoms using chirped femtosecond laser pulses. Experimentally, Photoelectron Angular Distributions (PADs) have proven the essential tool to identify the different excitation and ionization pathways.

We observed three distinct ionization pathways contributing to the measured PADs. The predominant contribution with combined s and d-symmetry is due to a 2+1+1 REMPI processes involving the strongly driven two-photon transition $4s \leftarrow\leftarrow 3s$, and subsequent ionization from the states $5p$, $6p$ and $7p$. Photoelectrons with combined d and g-symmetry originated from 3+1 REMPI via states $5f$ and $6f$. A weak contribution with combined p and f-symmetry close to the ionization threshold is attributed to the third channel, that is two-photon ionization of the non-resonant transiently populated state $3p$.

Selective population of the highly excited states $5p$, $6p$, $7p$ and $5f$, $6f$ was achieved by controlling a single pulse parameter, i.e. the chirp parameter φ_2. In particular, we observed highly selective population of state $7p$ using strongly down-chirped laser pulses. For strongly up-chirped laser pulses states $6p$ and $5f$ were populated with high efficiency and a dominant signal from state $5p$ was obtained for moderately up-chirped laser pulses. Moreover, in the intermediate chirp regions coherent superpositions of neighboring states have been excited.

Simulations based on numerical integration of the time-dependent Schrödinger-equation for a neutral 20-state system are in agreement with our experimental findings. In addition, a five-state model was developed in order to provide insights into the physical mechanisms at play. Our analysis of the time-dependent populations showed that by tuning the chirp parameter distinct physical mechanisms have been addressed, involving adiabatic and non-adiabatic time evolution along with Dynamic Stark-Shifts (DSSs) and (multiple) level crossings. It was pointed out that the occurrence of an uncommon "bow-tie" level crossing is responsible for the excitation of coherent superposition states as observed in the experiment. The strong DSS of the two-photon transition $4s \leftarrow\leftarrow 3s$ turned out to be of particular significance for populating state $5p$ being inaccessible in weak laser fields.

Our results highlight the importance of studying model systems experimentally and theoretically to better understand the physical mechanisms of strong-field coherent control. Our findings demonstrate that, in general, in strong-field control multiple pathways involving different physical mechanisms are at play simultaneously.

4.6 Details of Calculations

Each p state consists of $p_{1/2}$ and $p_{3/2}$ substates, coupled by $\Omega_{1/2}$ and $\Omega_{3/2}$, respectively, to a relevant s state. Therefore initially our system comprises overall 10 states (prior to eliminating state $3p$). To simplify our approach we perform a transformation to a dark-bright basis for each of the p states and thus eliminate half of the p substates as dark (uncoupled) states, and keep the rest, which become coupled by the root mean square of the relevant $\Omega_{1/2}$ and $\Omega_{3/2}$ and are the ones to be referred to as p states throughout the theoretical part of the paper.

The effective two-photon transition moment between states $3s$ and $4s$ is

$$q_{12} = -\frac{d_a d_b + d_c d_d}{2\Delta_{3p}}, \tag{4.25}$$

where $d_{a,c}$ and $d_{b,d}$ are the dipole moments for the transitions $3p_{1/2,3/2} \leftarrow 3s_{1/2}$ and $4s_{1/2} \leftarrow 3p_{1/2,3/2}$, respectively.

The effect of a quadratic phase modulation in frequency domain of the form

$$\varphi(\omega) = \frac{\varphi_2}{2}(\omega - \omega_0)^2 \tag{4.26}$$

is described in time domain by a modulated linearly polarized laser electric field $E(t)$ given as [52]

$$E\left(t\right) = 2Re\left\{E^{+}\left(t\right)\right\}, \tag{4.27}$$

where for the positive-frequency part we have

$$E^{+}\left(t\right) = \frac{E_0}{2\gamma^{1/4}} e^{-\frac{t^2}{4\beta\gamma}} e^{i\omega_0 t} e^{i(at^2-\varepsilon)} \tag{4.28}$$

with

$$\varepsilon = \frac{1}{2}\arctan\frac{\varphi_2}{2\beta}, \tag{4.29}$$

$$\beta = \frac{\Delta t^2}{8\ln 2}, \tag{4.30}$$

$$\gamma = 1 + \left(\frac{\varphi_2}{2\beta}\right)^2, \tag{4.31}$$

$$a = \frac{\varphi_2}{8\beta^2\gamma} \tag{4.32}$$

resulting in the time-dependent instantaneous laser frequency

$$\omega(t) = \omega_0 + 2at. \tag{4.33}$$

Here Δt denotes the FWHM of the intensity $I(t)$ of the unmodulated pulse, ω_0 is the laser carrier frequency and φ_2 is the chirp parameter to be varied.

We define a reference Rabi-frequency $\Omega(t) = \Omega_0 f(t)$, where $f(t)$ is the laser electric field envelope

$$f(t) = \frac{\exp\left(-\frac{t^2}{4\beta\gamma}\right)}{\gamma^{1/4}}. \tag{4.34}$$

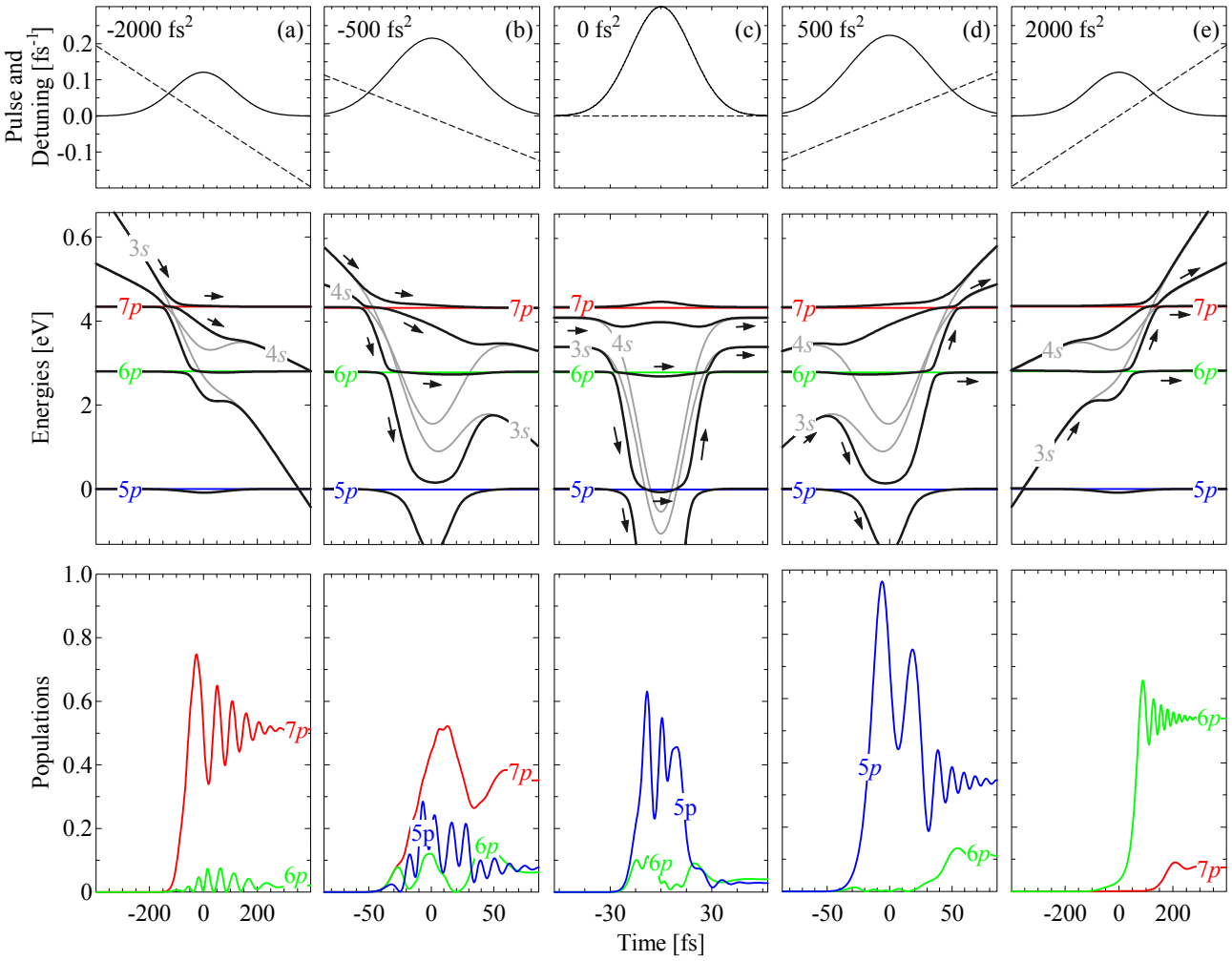

Figure 4.5: Populations (lower frames) and energies (middle frames) of the states of interest $5p$, $6p$ and $7p$ vs time for φ_2 varied (from left to right) between -2000 fs^2 (down-chirp) and 2000 fs^2 (up-chirp), $\Omega_0 = 0.3$ fs^{-1} and $\Delta t = 30$ fs. In the middle frames, colored and grey lines depict the bare state energies. The latter are related to states $3s$ and $4s$ and include the effective chirp, i.e. the chirp of the laser as well as the chirp due to ac Stark-shifts. Black lines represent the dressed state energies and the arrows are to show the population flow. The populations in the lower frames are consistent with the asymmetry in the experimental results presented in Fig. 4.4: for large chirps states $6p$ (positive chirp) and $7p$ (negative chirp) are predominantly populated, whereas around zero chirp the contribution comes mostly from state $5p$. The envelopes (straight lines) and detunings (dashed lines) of the modulated pulses are shown in the uppermost frames. Note that the energies are mirrored when changing the sign of the chirp φ_2.

Part II

Quantum Information Processing with Trapped Ions

Chapter 5

Trapped Ions

In this chapter we briefly consider the ion trapping, collective quantum motion of ions, and interaction with external laser fields.

5.1 Ion Trapping

The ion-trap system presents one of the most convenient systems for quantum information processing [60]. As its name implies, an ion trap confines charged particles to a confined region of space with magnetic and electric fields. We will consider specific realization of such trap, called a linear radio-frequency quadrupole trap, or a linear Paul trap [63], Fig. 5.1. The linear Paul trap consists of four conducting rods. Two opposing rods are connected to one pole of a radio-frequency (rf) voltage source, whereas the remaining two are grounded. The resulting electric potential along the trap axis (parallel with the z axis) is given by

$$\phi = \frac{U_0 + V_0 \cos \omega_{rf} t}{2 r_0^2} \left(x^2 - y^2 \right), \tag{5.1}$$

where ω_{rf} is the radio-frequency between two opposite rod electrodes, r_0 is the distance between the center and the electrode surface. The classical equations of motion of a particle with mass m and charge $Z\,|e|$ in the potential (5.1) read

$$\ddot{\mathbf{r}} = -\frac{Z\,|e|}{m} \nabla \phi \quad \mathbf{r} = (x, y, z)\,. \tag{5.2}$$

In spatial coordinates Eq. (5.2) are decoupled

$$\ddot{x} = -\frac{Z\,|e|}{m} \frac{U_0 + V_0 \cos \omega_{rf} t}{r_0^2} x, \tag{5.3a}$$

$$\ddot{y} = \frac{Z\,|e|}{m} \frac{U_0 + V_0 \cos \omega_{rf} t}{r_0^2} y, \tag{5.3b}$$

$$\ddot{z} = 0, \tag{5.3c}$$

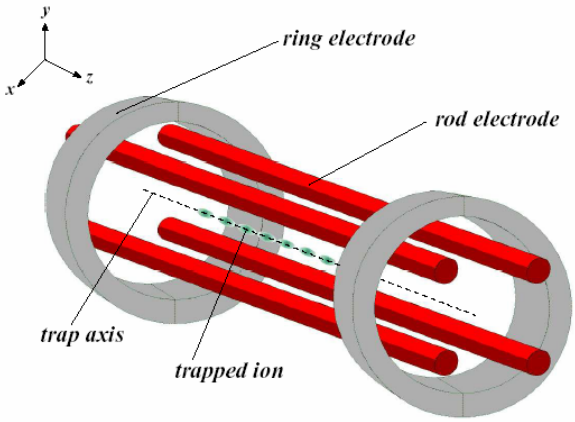

Figure 5.1: The linear Paul trap consists of four conducting rods. Two opposing rods are connected to one pole of a radio-frequency (rf) voltage source, whereas the remaining two are connected to the other pole. The axis of symmetry between the rods is the trap axis.

and after the substitutions

$$\begin{aligned} \zeta &= \omega_{rf} t/2, \\ a &= \frac{4Z\,|e|\,U_0}{m r_0^2 \omega_{rf}^2}, \\ q &= \frac{2Z\,|e|\,V_0}{m r_0^2 \omega_{rf}^2}, \end{aligned}$$

Eqs. (5.5) is transformed into the standard form of the *Mathieu* differential equation

$$\frac{d^2x}{d\zeta^2} + [a + 2q\cos(2\zeta)]\,x = 0, \tag{5.4a}$$

$$\frac{d^2y}{d\zeta^2} - [a + 2q\cos(2\zeta)]\,y = 0. \tag{5.4b}$$

The Mathieu equation belongs to the general class of differential equations with periodic coefficients [64]. Using the Floquet solution, the Mathieu equation can be solved exactly. With the assumption that $(|a|, q^2 \ll 1)$ the approximate stable solutions of Eq. (5.4) are given by

$$x(t) \approx x_0 \left[1 + \frac{q}{2}\cos(\omega_{rf} t)\right] \cos(\omega_x t + \varphi_x), \tag{5.5a}$$

$$y(t) \approx y_0 \left[1 - \frac{q}{2}\cos(\omega_{rf} t)\right] \cos(\omega_y t + \varphi_y), \tag{5.5b}$$

with

$$\omega_x = \frac{\omega_{rf}}{2}\sqrt{\frac{q^2}{2} + a}, \tag{5.6a}$$

$$\omega_y = \frac{\omega_{rf}}{2}\sqrt{\frac{q^2}{2} - a}, \tag{5.6b}$$

where x_0, y_0, φ_x, and φ_y are constants determined by the initial conditions. The motion of the single trapped ion consists of harmonic oscillations in the radial direction with frequencies ω_x and ω_y, called *secular motion*, and small contribution, oscillating at frequency ω_{rf}, called *micromotion*. The micromotion can be neglected under certain conditions, then the secular motion of the ion in the radial direction can be approximated by that of harmonic oscillators with frequencies ω_x and ω_y. The ion behaves as if it is confined in two dimensional harmonic pseudopotential ϕ_{2D} in the radial direction:

$$Z\left|e\right|\phi_{2D}=\frac{m}{2}\left(\omega_x^2x^2+\omega_y^2y^2\right). \tag{5.7}$$

If $U_0=0$, then $a=0$ and the frequencies ω_x and ω_y are equal

$$\omega_x = \omega_y=\omega_r=\frac{Z\left|e\right|}{\sqrt{2}mr_0^2\omega_{rf}}, \tag{5.8a}$$

$$Z\left|e\right|\phi_{2D} = \frac{m\omega_r^2}{2}\left(x^2+y^2\right). \tag{5.8b}$$

The ion can be confined along the z direction by static potentials U, applied in the ring electrodes at each end of the rods. The motion of the ion along the z axis is nearly harmonic with axial trapping frequency ω_z:

$$\frac{m\omega_z^2z_0^2}{2}\approx\xi Z\left|e\right|U, \tag{5.9}$$

where z_0 is the distance between the trap center and the ring electrode and ξ is a geometric factor. The ion becomes trapped in three dimensions and the resulting pseudopotential in all three directions is given by

$$Z\left|e\right|\phi_{2D}=\frac{m\omega_r^2}{2}\left(x^2+y^2\right)+\frac{m\omega_z^2z^2}{2}. \tag{5.10}$$

Typically, the ion is strongly bound in the radial direction and weakly bound in the axial direction, so we can neglect the radial oscillations of the ions.

5.2 Collective Motion of the Ions

We will consider a string of N ions in a linear Paul trap confined along the trap axis z with oscillation frequency ω_z. The total potential energy of the ion chain is given by

$$V=\sum_{n=1}^{N}\frac{1}{2}m\omega_z^2z_n^2\left(t\right)+\sum_{\substack{n,m=1\\n\neq m}}^{N}\frac{Z^2e^2}{8\pi\epsilon_0}\frac{1}{\left|z_n\left(t\right)-z_m\left(t\right)\right|}, \tag{5.11}$$

where $z_n(t)$ denote the position of the nth ion along the z axis. For sufficiently low temperatures [65], one can approximate the position of the nth ion by the equation

$$z_n(t) \approx z_n^0 + r_n(t), \tag{5.12}$$

where z_n^0 is the equilibrium position of the ion, and $r_n(t)$ is a small displacement. Solving the equation

$$\left[\frac{\partial V}{\partial z_n}\right]_{z_n=z_n^0} = 0, \tag{5.13}$$

one obtains the equilibrium positions of the ions. The Eq. (5.13) can be rewritten as a set of N coupled algebraic equations for the dimensionless equilibrium positions $u_n = z_n^0/l$:

$$u_n - \sum_{m=1}^{N} \frac{1}{(u_n - u_m)^2} + \sum_{m=n+1}^{N} \frac{1}{(u_n - u_m)^2} = 0, \tag{5.14}$$

where the length scale l is defined by the formula

$$l^3 = \frac{Z^2 e^2}{4\pi\epsilon_0 m\omega_z^2}. \tag{5.15}$$

The system (5.14) can be solved exactly for $N = 2$ and 3. In general, for arbitrary number of ions N, the equilibrium positions u_n can be determined numerically [66]. The minimum value of the separation of the central ions for different number of ions is approximated by the expression:

$$z_{\min}(N) \approx \left(\frac{Z^2 e^2}{4\pi\epsilon_0 m\omega_z^2}\right) \frac{2.018}{N^{0.559}}. \tag{5.16}$$

It is important to note that the zero point wavefunction of the individual ion in the trap is $\Delta z_{cm} = \sqrt{\hbar/2Nm\omega_z}$ and is of the order of $10nm$. The separation between the ions is typically 10 to $100\mu m$, so the wavefunction overlap is negligible. Increasing the number of ions introduces instabilities because they approach sufficiently close together [67]. The Coulomb repulsion between neighboring ions becomes stronger than the radial restoring force, and the linear configuration is replaced by the zigzag configuration. To prevent zigzag modes, the following condition have to be satisfied [68]:

$$\frac{\omega_r}{\omega_z} > 0.73N^{0.86}. \tag{5.17}$$

5.3 Normal Modes

The classical Lagrangian describing the motion of the ion string is given by

$$L = \frac{m}{2}\sum_{n=1}^{N} \dot{r}_n^2 - \frac{1}{2}\sum_{n,k=1}^{N} r_n r_k \left[\frac{\partial^2 V}{\partial z_n \partial z_k}\right]_{r_n=r_k=0}, \tag{5.18}$$

where we have neglected terms $O\left(r_n^3\right)$. The partial derivatives in Eq. (5.18) can be calculated explicitly and we obtain the following expression

$$L = \frac{m}{2}\left[\sum_{n=1}^{N}\dot{r}_n^2 - \omega_z^2\sum_{n,k=1}^{N}A_{nk}r_n r_k\right], \tag{5.19}$$

where the elements of the N-dimensional real symmetric matrix A_{nk} are determined by the external trapping potential and the Coulomb interaction between the ions and are given by [66]

$$A_{nk} = \begin{cases} 1 + 2\sum_{p=1,\ p\neq k}^{N}\frac{1}{|u_k - u_p|^3} \text{ if } n = k, \\ \frac{-2}{|u_k - u_n|^3} \text{ if } n \neq k. \end{cases} \tag{5.20}$$

The dynamics of the trapped ions is governed by the Lagrange equations

$$\frac{d}{dt}\frac{\partial L}{\partial \dot{r}_k} - \frac{\partial L}{\partial r_k} = 0, \quad k = 1, \ldots, N, \tag{5.21}$$

with Lagrangian (5.19). The general solutions of Eq. (5.21) can be written as follows

$$r_k\left(t\right) = \sum_{p=1}^{N}\mathbf{b}_k^{(p)}Q_p\left(t\right), \tag{5.22}$$

where $\mathbf{b}_k^{(p)}$ $(p = 1, 2, \ldots, N)$ are the eigenvectors of the matrix A_{nk} (5.20)

$$\sum_{n=1}^{N}A_{nk}\mathbf{b}_n^{(p)} = \mu_p\mathbf{b}_k^{(p)}, \tag{5.23}$$

with eigenvalues μ_p. The *normal modes* $Q_p\left(t\right)$ and *normal frequencies* ω_p of the ion motion are given by

$$Q_p\left(t\right) = C_p e^{-i\omega_p t}, \tag{5.24a}$$

$$\omega_p = \sqrt{\mu_p}\omega_z, \tag{5.24b}$$

where C_p are constants determined by the initial conditions. So, for N ions in a trap, there are N axial vibrational modes with frequencies ω_p and additional $2N$ modes, for motions transverse to the axis. The position of the kth ion can be written as

$$z_k\left(t\right) = z_k^0 + Re\left[\sum_{p=1}^{N}\mathbf{b}_k^{(p)}C_p e^{-i\omega_p t}\right]. \tag{5.25}$$

The lowest-energy vibration is the so-called *center-of-mass mode*, in which the ions oscillate back and forth in unison along the trap axis with frequency $\omega_1 = \omega_z$. The next vibrational mode is the *breathing mode*, where each ion oscillates with frequency $\omega_2 = \sqrt{3}\omega_z$ and amplitude proportional to its equilibrium distance to the trap center, Fig. 5.2. Remarkably, the frequencies of these two modes of oscillation are independent of N, and those of higher vibrational mode are nearly independent of N.

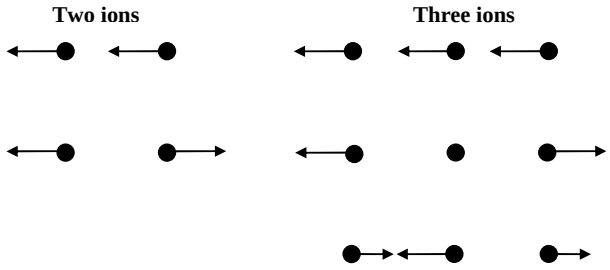

Figure 5.2: Eigenmodes for two and three ions. The first vibrational mode is the center-of-mass mode, the next is the breathing mode.

5.4 Quantized Vibrational Motion

The Lagrangian for the ionic oscillations (5.19) may be written in terms of normal modes Q_p as follows:

$$L = \frac{m}{2}\sum_{p=1}^{N}\left[\dot{Q}_p^2 - \omega_p^2 Q_p^2\right]. \tag{5.26}$$

The modes Q_p are uncoupled, so the corresponding canonical momentum conjugate to Q_p is $P_p = m\dot{Q}_p$ and one may write the Hamiltonian as

$$\hat{H} = \frac{1}{2m}\sum_{m=1}^{N} P_p^2 + \frac{m}{2}\sum_{m=1}^{N}\omega_p^2 Q_p^2. \tag{5.27}$$

The vibrational motion is quantized by introducing the operators

$$Q_p \;\rightarrow\; \hat{Q}_p = \sqrt{\frac{\hbar}{2m\omega_p}}\left(\hat{a}_p^\dagger + \hat{a}_p\right), \tag{5.28a}$$

$$P_p \;\rightarrow\; \hat{P}_p = i\sqrt{\frac{\hbar m\omega_p}{2}}\left(\hat{a}_p^\dagger - \hat{a}_p\right), \tag{5.28b}$$

where $\hat{Q}_p$ and $\hat{P}_p$ obey the canonical commutation relation $\left[\hat{Q}_p, \hat{P}_s\right] = i\hbar\delta_{ps}$ and the creation and annihilation operators $\hat{a}_p^\dagger$ and $\hat{a}_p$ satisfy the commutation relation $\left[\hat{a}_p^\dagger, \hat{a}_s\right] = \delta_{ps}$. In terms of creation and annihilation operators, the Hamiltonian (5.27) can be written as

$$\hat{H} = \sum_{n=1}^{N}\hbar\omega_n\left(\hat{a}_n^\dagger\hat{a}_n + \frac{1}{2}\right). \tag{5.29}$$

In the interaction picture the displacement operator of the kth ion from its equilibrium position is given by

$$\hat{r}_k(t) = \sqrt{\frac{\hbar}{2m\omega_z N}}\sum_{p=1}^{N} s_k^{(p)}\left(\hat{a}_p^\dagger e^{i\omega_p t} + \hat{a}_p e^{-i\omega_p t}\right), \tag{5.30}$$

where the coupling constant is defined by

$$s_k^{(p)} = \frac{\sqrt{N}\mathbf{b}_k^{(p)}}{\mu_p^{1/4}}. \tag{5.31}$$

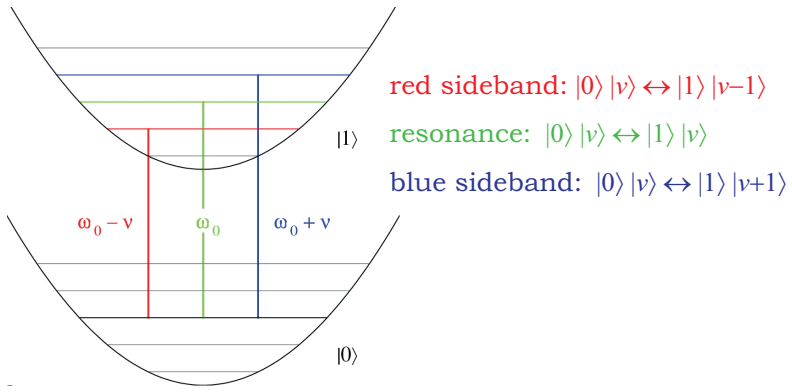

Figure 5.3: Energy levels of a two-level ion with Bohr frequency ω_0, trapped in a linear Paul trap with trap frequency ν.

5.5 Laser-Ion Interactions

We shall consider the situation where a periodically varying (classical) electromagnetic field propagating along the trap axis z is applied to a single two-level ion trapped in linear Paul trap [69]. The time-independent Hamiltonian associated with the internal ionic and collective vibrational degrees of freedom is

$$\hat{H}_0 = \hbar\frac{\omega_0}{2}\sigma_z + \hbar\omega_z\hat{a}^\dagger\hat{a}, \tag{5.32}$$

where the Pauli matrix describes internal atomic transitions, ω_0 is the Bohr frequency of the two-level ion, ω_z is the center-of-mass frequency, $\hat{a}^\dagger$ and $\hat{a}$ are the creation and annihilation operators of center-of-mass vibrational excitations (phonons). We assume that the internal levels of the ion are coupled by electric field propagating along the z direction, $\mathbf{E}(z,t) = E_0\epsilon\cos(kz - \omega_L t + \phi)$, where E_0 is the real amplitude, ϵ is the polarization vector, ω_L is the laser frequency, k is the wavevector, and ϕ is the phase factor. In the *dipole approximation* the the interaction Hamiltonian is given by

$$\begin{aligned}\hat{H}_I &= -\mathbf{d}\cdot\mathbf{E}(z,t) \\ &= \hbar\Omega\left(\sigma^+ + \sigma^-\right)\left(e^{i(kz-\omega_L t+\phi)} + e^{-i(kz-\omega_L t+\phi)}\right),\end{aligned} \tag{5.33}$$

where $\mathbf{d}$ is the electric dipole operator $\mathbf{d} = e\mathbf{r}$, with $\mathbf{r}$ – the position operator of the valence electron of the ion, and $\Omega \equiv -\frac{eE_0}{\hbar}|\langle 0|\mathbf{r}|1\rangle\cdot\epsilon|$ is the Rabi frequency. Here $\sigma^+ = |1\rangle\langle 0|$ and $\sigma^- = |0\rangle\langle 1|$ are Pauli spin-flip operators, $|0\rangle$ and $|1\rangle$ are the two level (qubit) states of the ion. The total Hamiltonian is

$$\hat{H} = \hat{H}_0 + \hat{H}_I. \tag{5.34}$$

It will be useful to transform the Hamiltonian (5.34) into the interaction picture, where we have $\hat{H}_I(t) = e^{\frac{i}{\hbar}\hat{H}_0 t}\hat{H}_I\, e^{-\frac{i}{\hbar}\hat{H}_0 t}$. The resulting interaction Hamiltonian after making the rotating-wave approximation (neglect $exp(\pm i(\omega_L + \omega_0))$ terms) is given by

$$\hat{H}_I(t) = \hbar\Omega\sigma^+ \exp\left\{i\left[\eta\left(\hat{a}^\dagger e^{i\omega_z t} + \hat{a}e^{-i\omega_z t}\right) - \Delta t + \phi\right]\right\} + \text{h.c.}, \tag{5.35}$$

where $\eta = \sqrt{\hbar k^2/2m\omega_z}$ is the Lamb-Dicke parameter and $\Delta = \omega_L - \omega_0$ is the laser detuning. The wave vector of the whole system is

$$|\Psi\rangle = \sum_{n=1}^{\infty}\left(C_{0,n}|0\rangle + C_{1,n}|1\rangle\right)|n\rangle, \tag{5.36}$$

where $|n\rangle$ is the vibrational state (Fock state) with n ($n = 0, 1, \ldots$) phonons. We assume that the detuning Δ has the following form

$$\Delta = (n' - n)\,\omega_z + \delta, \tag{5.37}$$

where n' and n are integers and δ is small detuning $|\delta| \ll \omega_z$, Ω. If the Rabi frequency Ω is sufficiently small, then the level structure of the ion can be considered as a series of isolated two levels $|0, n\rangle$ and $|1, n'\rangle$, and the coefficients in Eq. (5.36) obey the time-dependent Schrödinger equation

$$\frac{d}{dt}C_{1,n'} = -i^{(1+|n'-n|)}e^{-i(\delta t-\phi)}\Omega_{n',n}C_{0,n}, \tag{5.38a}$$

$$\frac{d}{dt}C_{0,n} = -i^{(1-|n'-n|)}e^{i(\delta t-\phi)}\Omega_{n',n}C_{1,n'}, \tag{5.38b}$$

where $\Omega_{n',n}$ is given by [70]

$$\Omega_{n',n} = \Omega e^{-\eta^2/2}\eta^{|n'-n|}\sqrt{\frac{n_<!}{n_>!}}L_{n_<}^{|n'-n|}\left(\eta^2\right), \tag{5.39}$$

and $n_<$ ($n_>$) is the lesser (greater) of n' and n, and $L_n^\alpha(x)$ is the generalized Laguerre polynomial [64]

$$L_n^\alpha(x) = \sum_{m=0}^{n}(-1)^m\begin{pmatrix} n+\alpha \\ n-m \end{pmatrix}\frac{x^m}{m!}. \tag{5.40}$$

If the laser frequency is tuned such that $\Delta n = n' - n = 0$, then the transition is called *carrier* transition. Transitions with $\Delta n > 1$ are called *blue-sideband* transitions, and transitions with $\Delta n < 1$ are called *red-sideband* transitions, Fig. 5.4.

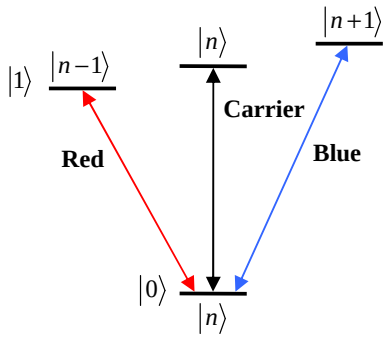

Figure 5.4: An ion trap naturally couples an ion's electronic excitations to its vibrational states. Ion interacting with a sufficiently narrow linewidth laser will change its internal state increasing the number of phonons in the common mode by one, $\Delta = \omega_z$, (blue-sideband transition), or decreasing the number by one, $\Delta = -\omega_z$, (red-sideband transition). Transitions, which change only internal ion levels, without affecting the vibrational states are carrier transitions, $\Delta = 0$.

5.5.1 Lamb-Dicke Limit

A special case of interest is when the Lamb-Dicke limit is satisfied. In that limit, the amplitude of the ion's motion in the direction of the radiation is much less than $\lambda/2\pi$ which corresponds to the condition

$$\sqrt{\langle \Psi_{motion} | \, k^2 z^2 \, | \Psi_{motion} \rangle} \ll 1. \tag{5.41}$$

Usually, the Lamb-Dicke limit is written with the less restriction η to be much smaller than one, $\eta \ll 1$. In that limit, we can evaluate $\Omega_{n',n}$ to lowest order of η to obtain

$$\Omega_{n',n} = \Omega \eta^{|n'-n|} \sqrt{\frac{n_>!}{n_<!}} \, |n' - n|^{-1} \, . \tag{5.42}$$

For a carrier transition $n' = n$, a red-sideband transition $n' = n - 1$, and a blue-sideband transition $n' = n+1$, the Rabi frequencies in the Lamb-Dicke limit are Ω, $\Omega\eta\sqrt{n}$, and $\Omega\eta\sqrt{n+1}$ respectively.

5.5.2 Jaynes-Cummings Hamiltonian

In the Lamb-Dicke limit, when the radiation is tuned near the center-of-mass red-sideband transition $\Delta = -\omega_z + \delta$, then the Hamiltonian (5.35) is given by

$$\hat{H}_{JC}(t) = \frac{\hbar\eta\Omega}{2} \left[\sigma^+ a e^{-i(\delta t - \phi)} + \sigma^- a^\dagger e^{i(\delta t - \phi)} \right] . \tag{5.43}$$

The Hamiltonian (5.43) is called Jaynes-Cummings Hamiltonian [71] in cavity quantum electrodynamics. It describes the coupling of a two-level atom to a single mode of the (quantized)

radiation field. It is straightforward to generalize Hamiltonian (5.43) for N ions, confined in linear Paul trap

$$\hat{H}_{JC}(t) = \sum_{k=1}^{N} \frac{\hbar\eta\Omega_k}{2\sqrt{N}} \left[\sigma_k^+ a e^{-i(\delta t-\phi)} + \sigma_k^- a^\dagger e^{i(\delta t-\phi)}\right]. \tag{5.44}$$

The important property of Jaynes-Cummings Hamiltonian is that it commutes with the excitation number operator $\hat{N} = a^\dagger a + \sum_{k=1}^{N} \sigma_k^+ \sigma_k^-$, i.e., $\left[\hat{H}_{JC}, \hat{N}\right] = 0$, hence the vast Hilbert space is decomposed into subspaces with definite number of excitations.

5.5.3 Anti-Jaynes-Cummings Hamiltonian

If the laser frequency is tuned to the center-of-mass blue-sideband transition, so that $\Delta = \omega_z - \delta$, then the Hamiltonian describing the interaction between the ions and the laser field has the following form

$$\hat{H}_{AJC}(t) = \sum_{k=1}^{N} \frac{\hbar\eta\Omega_k}{2\sqrt{N}} \left[\sigma_k^+ a^\dagger e^{i(\delta t+\phi)} + \sigma_k^- a e^{-i(\delta t+\phi)}\right]. \tag{5.45}$$

The Hamiltonian (5.45) describes the anti-Jaynes-Cummings model, which conserves the difference between the number of ionic and vibrational excitations – a feature characteristic of blue-sideband excitation.

Chapter 6

Simple Quantum Search

In the following two chapters we propose a simple implementation of Grover's quantum search algorithm. Utilizing the physical symmetries of the trapped-ion linear crystal, the physical realization of the algorithm represents a dramatic simplification: each logical iteration (oracle and inversion about average) requires only *two* physical interaction steps, in contrast to the large number of concatenated gates required by previous approaches. This does not only facilitate the implementation, but also increases the overall fidelity of the algorithm.

6.1 Introduction to Grover's Quantum Search Algorithm

One of the most celebrated applications of quantum information processing is Grover's quantum search algorithm, which allows an initially unknown element to be determined from $\mathcal{N}$ equally likely possibilities in $\mathcal{O}(\sqrt{\mathcal{N}})$ queries [2]. This outperforms the optimum classical strategy (a random 'trial and error' of elements), which requires $\mathcal{O}(\mathcal{N})$ steps on average.

Proof-of-principle quantum search has been successfully demonstrated in nuclear magnetic resonance, linear optical and trapped-ion systems, as well as with individual Rydberg atoms and in classical optics. Of these, only the trapped-ion platform possesses a fully scalable Hilbert space and in this sense it is realistically the only candidate for performing a practically useful quantum search. We note, however, that while the trapped-ion system is scalable, the largest dimensional quantum search so far performed with trapped ions was for a database size of $\mathcal{N} = 4$ [3]. Extending the approach of Ref. [3] to a large number of ions is highly demanding, since it requires the ability to construct, with very high fidelity, a great number of multiply-conditional gates. For two ions, as in Ref. [3], we need a controlled phase gate between the ions. When N ions are involved, however, we need a gate which is multiply-conditional upon

the internal state of *all N ions*. Although such a multiply-conditional gate may be decomposed efficiently using a series of one- and two-ion gates [74], in practice such a synthesis becomes a daunting task, even for a moderate number of ions. For example, for a four-qubit register, the oracle may be constructed using 13 two-qubit conditional gates [74], each of these requiring 5 consecutive physical interactions on average, which is beyond the capabilities of current experiments. The above example makes it apparent that there is a clear distinction between an approach, which is only *formally scalable*, and an approach, which is *realistically scalable* using current technology.

It is highly desirable, therefore, to find new ways of performing quantum search in a scalable system, which does not require an exorbitant number of elementary physical interactions. With the following two papers we propose a novel approach to perform Grover's search algorithm, which represents a dramatic simplification – the total number of *physical* steps is the same as the number of algorithmic steps.

Grover's algorithm provides a method for solving the unstructured search problem, which can be stated as follows: given a collection of database elements $x = 1, 2, \ldots, \mathcal{N}$, and an *oracle function* $f(x)$ that acts differently on one *marked* element s to all others,

$$f(x) = \begin{cases} 1, & x = s, \\ 0, & x \neq s, \end{cases} \tag{6.1}$$

find the marked element in as few calls to $f(x)$ as possible [2]. If the database is encoded in a physical system that behaves classically, then each oracle query can only act on a single database element. In this case, the optimal search strategy is simply a random selection of elements; on average, it will be necessary to make approximately $\mathcal{N}/2$ calls to the oracle before the marked element s is located. The idea underlying Grover's algorithm is to encode the database in a physical system that behaves quantum mechanically. Therefore, each possible search outcome is represented as a basis vector $|x\rangle$ in an $\mathcal{N}$-dimensional Hilbert space; correspondingly, the marked element is encoded by a *marked state* $|s\rangle$. Hence one can apply unitary operations (involving the oracle function) to *superpositions* of the different search outcomes. It is thus possible to amplify the amplitude of the marked state $|s\rangle$ using constructive interference, while attenuating all other amplitudes, and locate the marked element in $O(\sqrt{\mathcal{N}})$ steps. Before the execution of the algorithm, the quantum register is prepared in an *equal* superposition of all basis elements,

$$|W\rangle = \frac{1}{\sqrt{\mathcal{N}}} \sum_{x=1}^{\mathcal{N}} |x\rangle \,. \tag{6.2}$$

Central to the operation of the quantum search algorithm is the idea of generalized complex reflections, known in the computer science literature as *Householder reflections* (HR) [75]:

$$\hat{M}_{\psi}(\phi) = \mathbf{1} + (e^{i\phi} - 1)\,|\psi\rangle\,\langle\psi|\,. \tag{6.3}$$

When the phase ϕ is set equal to π, the effect of $\hat{M}_{\psi}(\phi)$ on any vector is to invert the sign of the component of this vector along $|\psi\rangle$, while leaving all other components unchanged, which amounts to a reflection with respect to an $(\mathcal{N}-1)$-dimensional plane orthogonal to $|\psi\rangle$. Allowing ϕ to take arbitrary values extends the concept of reflection, by imprinting an arbitrary phase onto the component along $|\psi\rangle$, rather than a simple sign inversion. Householder reflections are widely used in classical data analysis and also constitute a powerful tool for coherent manipulation of quantum systems [54, 76–79]. The core component of Grover's algorithm is a pair of coupled Householder reflections, which together form a single *Grover operator* $\hat{G}$:

$$\hat{G} = \hat{M}_{W}\,(\varphi_{W})\,\hat{M}_{s}(\varphi_{s}). \tag{6.4}$$

According to standard nomenclature, the operator $\hat{M}_{s}(\varphi_{s})$ is referred to as the oracle query, while $\hat{M}_{W}(\varphi_{W})$ is known as the inversion-about-average operator.

We note that with the initial state given in Eq. (6.2), and during successive applications of the operator $\hat{G}$, the state vector for the system begins and remains in the two-dimensional subspace defined by the non-orthogonal states $|s\rangle$ and $|W\rangle$. Each application of $\hat{G}$ amplifies the marked state population until it reaches a maximum value close to unity after n_{G} iterations, at which point the search result can be read out by a measurement in the computational basis.

The problem of how to optimize the quantum search routine by allowing arbitrary φ_{W} and φ_{s} has been studied extensively [80–82]. It is found that the maximum possible amplitude amplification per step of the marked state arises when the phases φ_{W} and φ_{s} are both set to π (as in Grover's original proposal [2]). The corresponding minimum number of search steps $n_{G}^{\min}$ is given by:

$$n_{G}^{\min} = \left[\frac{\pi}{2\arcsin\left(2\sqrt{\mathcal{N}-1}/\mathcal{N}\right)}\right] \overset{\mathcal{N}\gg 1}{\sim} \left[\frac{\pi\sqrt{\mathcal{N}}}{4}\right], \tag{6.5}$$

where $[n]$ denotes the integer part of n. However, this choice of phases is not unique. For large $\mathcal{N}$, as long as the *phase matching* condition $\varphi_{W} = \varphi_{s} = \varphi$ is satisfied [81], a high fidelity search can be performed for any value of φ in the range $0 < \varphi \leqq \pi$ and for certain values of φ, a deterministic quantum search is possible [80].

6.2 Simple Implementation in a Linear Database

We consider N ions confined and laser cooled in a linear Paul trap, each with two relevant internal states $|0\rangle$ and $|1\rangle$, with respective transition frequency ω_0. The radial trap frequencies are much larger than the axial frequency ω_{tr}, so that the ions form a linear string along the z axis [66]. The ions are cooled into their motional zero-phonon ground state $|0\rangle$ [83] and interact with a laser pulse with frequency $\omega_{\mathrm{L}} = \omega_0 - \omega_{\mathrm{tr}} - \delta$, where δ is the laser detuning from the first red-sideband resonance. We assume that the phonon spectrum can be resolved sufficiently well that only the center-of-mass mode is excited by this interaction and that other vibrational modes can safely be neglected. In the Lamb-Dicke limit, and after making the optical and vibrational rotating-wave approximations, the interaction Hamiltonian is [69]:

$$\hat{H}_I(t) = \hbar \sum_{k=1}^{N} \left[g\left(t\right) \left(\sigma_k^+ \hat{a} + \sigma_k^- \hat{a}^\dagger \right) + \frac{\delta}{2} \sigma_k^{(z)} \right]. \tag{6.6}$$

Here $\sigma_k^+ = |1_k\rangle\langle 0_k|$ and $\sigma_k^- = |0_k\rangle\langle 1_k|$ are the raising and lowering operators for the internal states of the kth ion, $\sigma_k^{(z)}$ is the Pauli spin matrix and $\hat{a}^\dagger$ and $\hat{a}$ are respectively the creation and annihilation operators of center-of-mass phonons. The coupling between the internal and motional degrees of freedom is $g(t) = \eta\Omega(t)/2\sqrt{N} = gf(t)$, where $\eta = \sqrt{\hbar|\mathbf{k}|^2/2M\omega_{\mathrm{tr}}}$ is the single-ion Lamb-Dicke parameter, with $\mathbf{k}$ being the laser wave vector and M is the mass of the ion. The function $\Omega(t)$ is the real-valued time-dependent Rabi frequency.

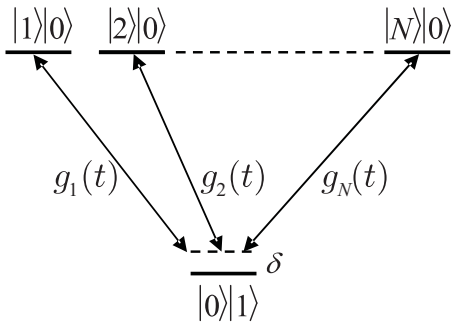

Figure 6.1: Linkage pattern of the collective states of N trapped ions driven by a red-sideband laser pulse. The lower state $|0\rangle\,|1\rangle$ involves one vibrational phonon and no ionic excitations, whereas the upper set of states $\{|k\rangle\,|0\rangle\}_{k=1}^{N}$ involves zero phonons and a single ionic excitation of the kth ion.

Since the Hamiltonian (6.6) is of Jaynes-Cummings type, it conserves the sum of ionic and vibronic excitations; hence the Hilbert space decomposes into subspaces with a definite number

of excitations. The *single-excitation subspace* is spanned by the $N+1$ basis states,

$$|k\rangle|0\rangle = |0_1 \ldots 0_{k-1}, 1_k, 0_{k+1} \ldots 0_N\rangle|0\rangle, \tag{6.7a}$$

$$|0\rangle|1\rangle = |0_1 \ldots 0_N\rangle|1\rangle, \tag{6.7b}$$

where $|\mu\rangle$ is the vibrational state with μ phonons ($\mu = 0, 1$), and $|0_1 \ldots 0_{k-1}, 1_k, 0_{k+1} \ldots 0_N\rangle$ is a collective ionic state ($k = 1, 2, \ldots N$), in which the kth ion is in state $|1\rangle$ and all other ions are in state $|0\rangle$. Our quantum memory register will be the set of states (6.7a): $\{|k\rangle\}_{k=1}^{N}$; throughout the algorithm operation the population remains in vibronic state $|0\rangle$; it will be omitted hereafter.

Householder Reflection

The Hamiltonian (6.6) can be written as [84]

$$\hat{H}_I(t) = \frac{\hbar}{2}\sum_{n=1}^{N} g(t)|0\rangle\langle n| + \frac{\hbar}{2}\delta|0\rangle\langle 0| + \text{h.c.}, \tag{6.8}$$

The linkage pattern for this Hamiltonian is an N-pod, wherein state $|0\rangle$ is coupled to each state in the manifold $\{|k\rangle\}_{k=1}^{N}$, as shown in Fig. 6.1. It has been shown very recently that the propagator within the single-excitation manifold $\{|k\rangle\}_{k=1}^{N}$ for exact resonance ($\delta = 0$) and for root-mean-square (rms) pulse area $A = g\int_{-\infty}^{\infty} f(t)\mathrm{d}t = 2(2l+1)\pi$ (with $l = 0, 1, 2, \ldots$), is given by a *standard HR* [84–86],

$$\hat{M}_\psi = \mathbf{1} - 2|\psi\rangle\langle\psi|, \tag{6.9}$$

where the components of the N-dimensional normalized vector $|\psi\rangle$ are the normalized couplings,

$$|\psi\rangle = \frac{1}{g}[g_1, g_2, \ldots, g_N]^T. \tag{6.10}$$

The *generalized HR* (6.3) within the manifold $\{|k\rangle\}_{k=1}^{N}$ is realized at suitably chosen detunings. For example, for a hyperbolic-secant pulse, $g(t) = g\,\mathrm{sech}\,(t/T)$, with rms area $A = 2\pi l$ ($l = 1, 2, \ldots$), the HR phase ϕ is produced by detunings, obeying the equation $2\arg\prod_{j=1}^{l-1}[\delta T + i(2j+1)] = \phi$ [87]. The generalized HR can be created also for other pulse shapes, e.g. Gaussian, but the required pulse area and detuning have to be evaluated numerically.

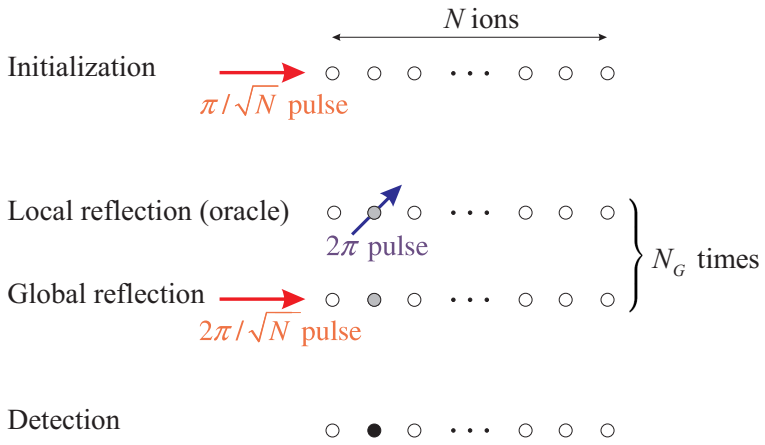

Figure 6.2: Implementation of Grover's search with N trapped ions. The ion chain is initialized in an entangled W-state by preparing it initially in state $|0\rangle|1\rangle$, and then apply a red-sideband pulse with a temporal area of $\pi/\sqrt{N}$ uniformly at all ions. Then we perform repeatedly, N_G times, a local reflection of the marked ion by applying a 2π pulse on it, followed by a global reflection, inflicted by a $2\pi/\sqrt{N}$ pulse applied to the entire ion string. Finally, the marked ion is identified for it is the only one in state $|1\rangle$.

Implementation

The implementation of the Grover algorithm is depicted in Fig. 6.2.

1. *Initialization* We first prepare the register (6.7a) in an equally weighted superposition of all N states (6.2); this is the well-known entangled W-state, which has been demonstrated experimentally with eight ions [88]. For this, one can choose between the latter technique [88], adiabatic-passage techniques [89, 90], or a HR-based technique [84]. For Grover's search it is most convenient to use the following alternative [87]: prepare the ion chain initially in state $|0\rangle|1\rangle$, and then apply, uniformly at all ions, a red-sideband pulse with a temporal area of $\pi/\sqrt{N}$ experienced by each ion (hence rms area of π).

2. *Grover iteration* Each Grover logical step consists of two operators, an oracle call and a global HR [2]. Firstly, the oracle marks the searched state $|s\rangle$ by inverting its phase, which in our implementation is achieved by individual addressing of only the sth ion by a local 2π pulse; in fact, this is a HR operation $\hat{M}_s$ with an interaction vector $|s\rangle$ identical to the basis vector $|s\rangle$ of Eq. (6.7a). The second HR $\hat{M}_W$ inverts the amplitude of all states $|k\rangle$ about the mean. In our implementation this HR is produced by applying a single laser pulse, uniformly at all N ions in the register, with a temporal area of $2\pi/\sqrt{N}$ (which amounts to rms-area of 2π), as shown in Fig. 6.2. After the execution of the Grover operator N_G times, the system is

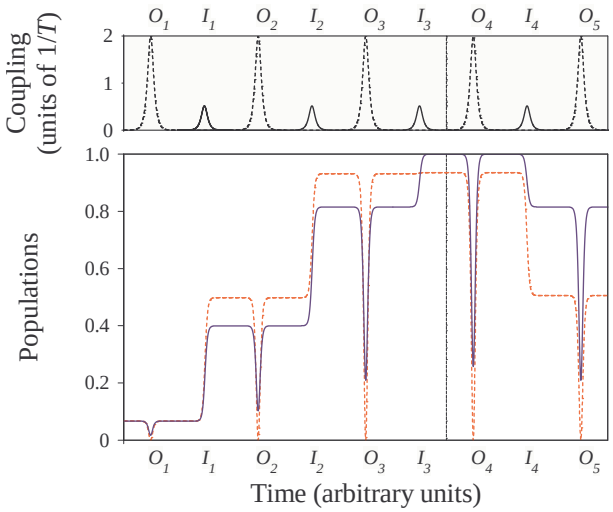

Figure 6.3: Numerically calculated population of the marked state vs time for $N = 15$ ions for probabilistic (dashed line) and deterministic (solid line) Grover search. The upper frame depicts the sequence of local (dashed, O_k, area 2π) and global (solid, I_k, area $2\pi/\sqrt{N}$) pulses, both with sech shapes. The detuning in the deterministic search is $\delta T \approx 0.589$, which produces the required phase $\phi \approx 0.661\pi$. Maximum probabilities occur after the completion of I_3, when the dashed curve reaches 0.92 and the solid line unity.

driven into the marked state, $\left[\hat{M}_W \hat{M}_s\right]^{N_G} |W\rangle \approx |s\rangle$.

3. *Detection* The marked ion is identified for it is the only one in state $|1\rangle$.

In Fig. 6.3 the probability to find the searched state for $N = 15$ ions is plotted as a function of time. In three interaction steps, which amount to 3 local (oracle) pulses and 3 global (reflection) pulses, this probability increases to about 0.92, after which it decreases (as a part of oscillations between zero and unity in a long run).

The original Grover algorithm is probabilistic (except for $N = 4$): it finds the marked state with a probability (fidelity) close to, but less than unity. A slight modification of the original Grover algorithm, with the supplement of the (real) reflection operators by complex phase factors, makes the search fully deterministic, with a unit fidelity for any N, with N_G or $N_G + 1$ roundtrips [91].

The deterministic search can be implemented with the same strategy as the original Grover search described above, by replacing the HRs $\hat{M}_s$ and $\hat{M}_W$ with the generalized HRs $\hat{M}_s(\phi)$ and $\hat{M}_W(\phi)$: $\left[\hat{M}_W(\phi)\hat{M}_s(\phi)\right]^{N_G} |W\rangle = |s\rangle$. The HR phase reads $\phi = 2\sin^{-1}[\sqrt{N}\sin(\pi/(4N_G + 6))]$ [91]; it can be produced by a suitable detuning δ, as explained above.

In Fig. 6.3 the population of the marked state is plotted for deterministic Grover search with $N = 15$. After just three iterations, the occupation probability for the marked state

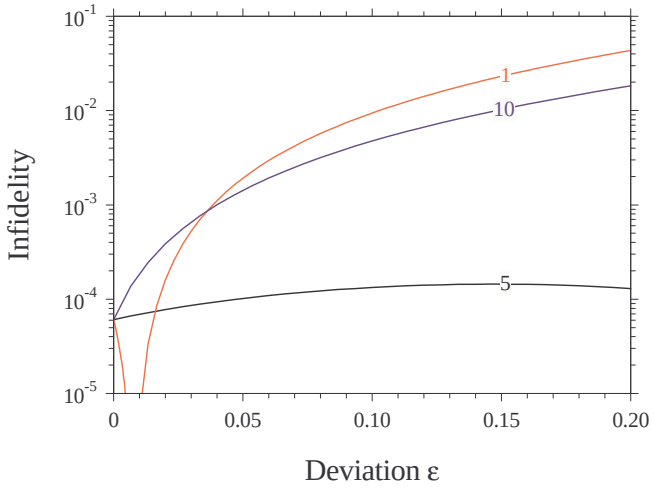

Figure 6.4: Infidelity of finding ions 1, 5 and 10 after 3 steps for $N = 20$ for a Gaussian spatial laser beam profile of the global pulse (rms area 2π, detuning $\delta = 0$), where the outside ions experience only a fraction $1 - \varepsilon$ of the laser intensity in the middle of the ion chain.

approaches unity, whereas it is only 0.92 for the standard Grover search.

6.3 Practical Considerations

Now we discuss briefly various issues that may arise in a real experiment. An obvious deviation from the idealized theory can be the imperfect initialization of the search register (the W-state), due to an inhomogeneous spatial profile of the driving laser(s), for example, if the laser beam for the global reflection is tilted from being collinear with the trap axis. Then the initial state will not be an equal superposition, but the more general state $|a\rangle = \sum_{n=1}^{N} a_n |n\rangle$, where the probability amplitudes a_n may deviate from $1/\sqrt{N}$, and they may also be complex, due to possible phase differences between the ions. It has been shown that the register $|a\rangle$ can still be used for Grover's search if the amplitudes a_n do not deviate too much from $1/\sqrt{N}$ [92, 93]. Biham *et al.* [93] have shown that the application of the same Grover operator, as for an equally weighted initial superposition, to the initial state $|a\rangle$ still produces the marked item with a reasonable probability. However, it is readily shown that a HR with respect to the vector $|a\rangle = [a_1, a_2, \ldots, a_N]^T$ allows for a higher probability. Using the approach of Hsieh and Li [94] one can show that the optimum number of steps N_G is replaced by $N_a = [\pi/(4|a_s|)]$ (for small a_s), where a_s is the initial amplitude of the marked state $|s\rangle$.

Figure 6.4 shows the infidelity to detect the marked states $|1\rangle$, $|5\rangle$ and $|10\rangle$ for $N = 20$ ions after $N_G = 3$ steps for a Gaussian laser beam profile of the global pulse, where the outside

ions experience only a fraction $1-\varepsilon$ of the laser intensity in the middle of the ion string. The proposed technique proves to be very robust with respect to the imperfectness of the laser profile.

In the proposed implementation the interaction needed can be produced very simply: by using the same laser beam as in the initialization step (which has produced the possible inhomogeneities in the register), but with twice as high Rabi frequency, cf. Fig. 6.2. This robustness to imperfections in the initial register, caused by unequal individual laser-ion couplings, also implies that the proposed implementation of Grover's search can utilize higher vibrational modes, e.g., the breathing mode, for which the laser-ion couplings depend on the position of the ion in the string [66]; using higher phonon modes greatly reduces deleterious heating effects.

6.4 Discussion and Conclusions

In this Letter, we have proposed a very simple and concise implementation of Grover's search algorithm in a linear chain of N trapped ions. Unlike earlier proposals, which, in addition to the $\mathcal{O}(\sqrt{N})$ queries, require many more physical nonquery steps, the proposed implementation requires only $\mathcal{O}(\sqrt{N})$ such steps, one for each of the $\mathcal{O}(\sqrt{N})$ queries; hence each Grover iteration is performed by one local HR (query) and one global HR (nonquery). The speed-up in regard to physical steps derive from the natural emergence of the HR operator as the propagator in a red-sideband laser-driven linear string of trapped ions.

We point out that the proposed implementation, while using an entangled W-state as a quantum register, does not utilize the full power of a quantum register, which can contain 2^N states. Work in this direction is presented in the following chapter.

Chapter 7

Scalable Quantum Search

In the previous proposal the database size $\mathcal{N}$ grows linearly with the number of ions N. The implementation is remarkably simple and robust, but one needs an exorbitant number of ions to encode a database of moderate size, e.g. a couple of hundreds. The approach below is slightly more complicated, as the interaction parameters (coupling and detuning) must be calculated numerically, but the database is now exponential in the number of ions, i.e. we need a few ions to store hundreds of database elements. Our analytical approach is based on a factorization of the Hilbert space into a set of independent (noninteracting) chains of quantum states.

7.1 Hilbert Space Factorization

The Hamiltonian (6.6) conserves the total number of excitations (n_i ionic plus n_p motional), which in the scheme we propose, is half the number of ions, i.e. $N/2$ (with N even), $n_i + n_p = N/2$. The energy pattern splits into manifolds corresponding to n_i ionic and $n_p = N/2 - n_i$ motional excitations. Each manifold is $C_{n_i}^N$-fold degenerate, where $C_{n_i}^N = N!/n_i!\,(N-n_i)!$. It is readily verified that the dimension of the $n_i = N/2$ manifold, $\mathcal{D}$, grows *exponentially* with N; indeed, for large N we have

$$\mathcal{N} \equiv C_{N/2}^N \sim \frac{2^N}{\sqrt{\pi N/2}} \left[1 - \frac{1}{4N} + \mathcal{O}\left(N^{-2}\right)\right]. \tag{7.1}$$

The subspace of the overall Hilbert space, which spans the manifold $\mathcal{D}$, we shall use to represent the state of the register in Sec. 7.2; $\mathcal{D}$ is the set of states, which encode the database of $\mathcal{N}$ elements.

It is possible to move to a new basis in which the Hilbert space is factorized into a collection of noninteracting chains of states. The new states we shall call MS states, since they can be obtained by the multilevel Morris-Shore (MS) factorization [96].

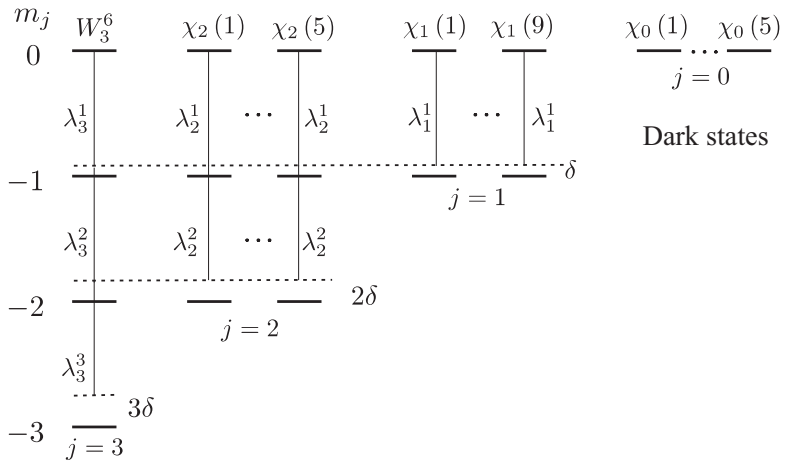

Figure 7.1: The MS basis states for $N = 6$ ions with 3 excitations consists of a series of independent chainwise linkages. Since the total number of excitations is half the number of ions, then from Eq. (7.3) follows that states with $m_j > 0$ are inaccessible and are therefore not shown. The states that make up the longest ladder are all symmetric Dicke states [95]. The number of motional n_p and ionic n_i excitations for each level can be inferred from m_j, Eq. (7.3).

To determine the MS states first we rewrite the Hamiltonian (6.6) in terms of the total ionic pseudospin:

$$\hat{H}_I(t) = \hbar g\,(t)\left(\hat{a}\hat{J}_+ + \hat{a}^\dagger \hat{J}_-\right) + \hbar\delta\hat{J}_z, \tag{7.2}$$

where $\hat{J}_\pm = \sum_{k=1}^N \sigma_k^\pm$ and $\hat{J}_z = \frac{1}{2}\sum_{k=1}^N \sigma_k^{(z)}$. The MS basis consists of the set of the eigenvectors of the two commuting operators $\hat{J}^2$ and $\hat{J}_z$, where $\hat{J}^2 = \frac{1}{2}(\hat{J}_+\hat{J}_- + \hat{J}_-\hat{J}_+) + \hat{J}_z^2$. Therefore each MS state is assigned two quantum numbers, respectively j and m_j. Since $\hat{J}^2$ commutes also with the Hamiltonian (7.2), the Hilbert space factorizes into a set of decoupled chains with different values of j.

The MS states are sketched in Fig. 7.1 for 6 ions with 3 excitations. Because the laser pulse couples equally to every ion in the trap, the longest chain is comprised of the symmetric Dicke states $\left|W_{n_i}^N\right\rangle$, wherein a given number of ionic excitations n_i is shared evenly amongst all the ions in the trap [95]. Each chain is assigned different j and is comprised of states with different m_j, which varies from 0 to j, corresponding to the number of excited ions. If n_i of the ions are excited, then

$$m_j = n_i - \frac{N}{2} = -n_p. \tag{7.3}$$

Since the total number of excitations is half the number of ions, then from Eq. (7.3) it follows that for each chain m_j has a maximum value of 0, i.e. states with $m_j > 0$ are inaccessible. By

analogy with the traditional angular momentum operators, it follows that the number of states in a chain is equal to $j+1$ (j of the states are not accessible), from which j can be inferred. The longest chain corresponds to $j = N/2$, the next longest to $j = N/2-1$ and so on, and overall, there are $[N/2+1]$ chains of different length in the factorized coupling scheme.

For the following analysis, it will be necessary to go further and calculate the couplings in the MS basis. The coupling between the neighbors $|j, m_j\rangle$ and $|j, m_j - 1\rangle$ follows immediately from the matrix elements of the operators $\hat{a}^\dagger$ and $\hat{J}_-$, i.e.

$$\begin{aligned}\lambda_j^{m_j}(t) &= g(t)\sqrt{n_p(j+m_j)(j-m_j+1)} \\ &= g(t)\sqrt{n_p(j+n_i-N/2)(j+N/2+1-n_i)}\,. \end{aligned} \tag{7.4}$$

As illustrated in Fig. 7.1, there can be many different degenerate MS states with the same values of j and m_j. We label the states with a given $j \neq N/2$ and $m_j = 0$ with $|\chi_j(k)\rangle$, where $k = 1, \ldots, N_j$, with $N_j = C^N_{N/2-j} - C^N_{N/2-j-1}$.

7.2 Implementation of Grover's Algorithm

The manifold $\mathcal{D}$, which encodes the database elements, consists of the states, for which the pseudo-angular momentum projection is $m_j = 0$, Eq. (7.3). This requires that the total number of ions N is even. Half of these are in state $|1\rangle$, while the other half are in state $|0\rangle$ ($n_i = N/2$). The number of elements $\mathcal{N}$ in the database therefore scales exponentially with the number of ions N, Eq. (7.1). The elements $|x\rangle$ in Eq. (6.2), which belong to $\mathcal{D}$, can now be written as

$$|x\rangle = P_x \left|1_1 \ldots 1_{N/2} 0_{N/2+1} \ldots 0_N\right\rangle, \tag{7.5}$$

where the subscript x runs over all distinct permutations P_x of the ions' internal states. The initial state $|W\rangle$ is thus a symmetric Dicke state $\left|W^N_{N/2}\right\rangle$ of N ions sharing $N/2$ excitations,

$$\left|W^N_{N/2}\right\rangle = \frac{1}{\sqrt{C^N_{N/2}}} \sum_x P_x \left|1_1 \ldots 1_{N/2} 0_{N/2+1} \ldots 0_N\right\rangle. \tag{7.6}$$

Our proposed experimental procedure consists of four simple operations. (i) The ions are firstly initialized in the entangled Dicke state (7.6). This may be achieved using very simple adiabatic passage techniques, involving either a pair of chirped laser pulses [95,97] or two pairs of delayed but overlapping laser pulses [98], and using global addressing. (ii) Synthesis of the inversion-about-average operator is appealingly simple: $\hat{M}_W$ is a single red-sideband off-resonant laser

pulse addressing all ions in the linear chain. (iii) The oracle query $\hat{M}_s$ is also a single red-sideband laser pulse, applied on half of the ions. After an appropriate number of iterations (6.5), the system evolves into the marked state $|s\rangle$, which can be identified by performing (iv) a fluorescence measurement on the entire chain.

7.2.1 Synthesis of the Inversion-about-Average Operator

In most existing proposals for implementing Grover's search algorithm using trapped ions the generation of $\hat{M}_W$ requires a large number of concatenated physical interaction steps, even for moderate register size $\mathcal{N}$. However, by restricting the dynamics to the subspace of the overall Hilbert space in which only half of the ions are excited, this operator becomes possible to synthesize in only a *single* interaction step. This simplification is achieved by taking advantage of the fact that both the Hamiltonian (7.2) and the state $\left|W^N_{N/2}\right\rangle$ are symmetric under exchange of any two ions.

The energies of the MS states do not cross in time so that in the limit $\delta \gg 1/T$ the transitions between the MS states vanish due to the effect of adiabatic complete population return [99]. Each of the MS states acquires a phase shift φ_j (the index j corresponds to the eigenvalue of $\hat{J}^2$) and the unitary propagator within the Dicke manifold $\mathcal{D}$ is a product of $C^N_{N/2-1}$ coupled reflections [100]

$$\hat{U}_W = \hat{M}_W(\varphi_W) \prod_{j=1}^{N/2-1} \prod_{k=1}^{N_j} \hat{M}_{\chi_j(k)}(\varphi_j), \tag{7.7}$$

with $N_j = C^N_{N/2-j} - C^N_{N/2-j-1}$ and $\varphi_W = \varphi_{N/2}$. For a given value of the coupling, the detuning may be adjusted in order to control the phases φ_j. Ideally, these interaction parameters would be chosen such that $\varphi_W \neq 0$ (e.g., $\varphi_W = \pi$), while $\varphi_{j\neq N/2} = 0$ as this would result in $\hat{U}_W$ being identical to the inversion-about-average operator $\hat{M}_W(\varphi_W)$.

7.2.2 Synthesis of the Oracle Operator

The effect of each oracle query $\hat{M}_s(\phi_s)$ is to imprint a phase shift ϕ_s on the marked state $|s\rangle$, whilst leaving all other computational basis states unchanged. In general this can be achieved by a multiply-conditional phase gate upon the internal state of all N ions in the trap. When more than a few ions are involved, this becomes a prohibitively complicated operation, which generally requires an immense number of one- and two-qubit gates [74]. However, since we do not work in the whole Hilbert space, but rather in the manifold $\mathcal{D}$, the oracle operator can be implemented in a much simpler fashion – by a *single* red-sideband laser pulse, addressing

uniformly those $N/2$ ions in the trap, which share the excitation of the marked state.

Let's consider an example, when the marked state is $|s\rangle = |111000\rangle$. Then we address the first three ions. Since the initial state $\left|W^N_{N/2}\right\rangle$ and the interactions with the laser are symmetric under exchange of the first three ions, and the last three, as well, during the execution of the algorithm the state of the system is a linear combination of the states $|\Phi_k\rangle = \left|W^{N/2}_{N/2-k}\right\rangle \left|W^{N/2}_{k}\right\rangle$, $k = 0, \ldots, N/2$; the marked state is $|s\rangle = |\Phi_0\rangle$. Because the Hamiltonian, which describes the oracle call, does not change the total number of excitations of the first (and the last) three ions, i.e. it does not drive the system between $|\Phi_{k_1}\rangle$ and $|\Phi_{k_2}\rangle$ for $k_1 \neq k_2$, in the adiabatic limit the states $|\Phi_k\rangle$ acquire only phase shifts ϕ_k. Therefore the propagator in the manifold $\mathcal{D}$ is formally described by the action of $N/2$ coupled reflections,

$$\hat{U}_s = \hat{M}_s(\phi_s) \prod_{k=1}^{N/2-1} \hat{M}_{\Phi_k}(\phi_k). \tag{7.8}$$

Hence, as in the case of the inversion-about-average operator, we need to control $N/2$ phases. The interaction parameters should be chosen such that $\phi_s = \varphi_W$, while $\phi_{k\neq N/2} = 0$, as this would result in $\hat{U}_s$ being identical to the oracle operator $\hat{M}_s(\phi_s)$.

7.3 Phase Conditions

The phase conditions for the propagators $\hat{U}_W$ and $\hat{U}_s$, derived above, cannot be satisfied exactly, since the phases φ_k and ϕ_k are overly commensurate. However one can still perform the algorithm with sufficiently high fidelity

$$P = 1 - 2\left|\mathrm{Re}\langle f|\Delta f\rangle\right|. \tag{7.9}$$

Here $|f\rangle$ is the state of the system after the completion of the algorithm and $|\Delta f\rangle$ is its deviation due to the phases deviation. Fortunately, a Fourier expansion reveals that phase deviation of all odd orders leads to the purely imaginary bracket $\langle f|\Delta f\rangle$ and hence do not contribute to Eq. (7.9). As a result, the algorithm is less sensitive to phase deviations since only those of second order have a leading affect on the final state populations.

7.4 Numerical Demonstration

As a demonstration, we have solved the Schrödinger equation numerically for a Gaussian pulse shape and a constant detuning δ. Sample results are shown in Fig. 7.2 for $N = 6$, 8 and

10 ions with 3, 4 and 5 excitations, respectively, which imply databases of $\mathcal{N} = 20$, 70 and 252 elements. The fidelity plotted on the vertical axis is the time-dependent population of the marked state. The system of ions is assumed to be prepared initially in the Dicke superposition $\left|W^N_{N/2}\right\rangle$ of ionic collective states, each of which contains exactly $N/2$ ion qubits in state $|1\rangle$ and $N/2$ in state $|0\rangle$. Each Grover iteration consists of a phase shift for the marked state (oracle call), which amounts a single red-sideband laser pulse, addressing uniformly those $N/2$ ions in the chain, which share the excitation of the marked state, followed by a single red-sideband pulse, which addresses uniformly the entire ion chain (the inversion-about-average operator).

7.5 Conclusions

Despite the intense flurry of theoretical and experimental activity in the decade following Grover's original proposal for a quantum speed-up of unstructured search, a large discrepancy still remains between the current experimental state-of-the-art and what is required for a practically useful quantum search. To highlight this incongruence, we note that the only physical system in which a scalable quantum search has been performed is in a chain of trapped ions, and in that experiment, the search-space totalled just four elements. An important intermediate goal on the long road to performing a practically useful quantum search is to demonstrate Grover's algorithm in a moderately-sized trapped-ion quantum register. The standard approach of building up the many-ion Grover operator using a network of single- and two-qubit gates is inappropriate for this task, since the required physical resources far exceed those available in today's experiments. By contrast, in this article, we have proposed to construct the many-ion Grover operator using only two single off-resonant laser pulses, with a suitably chosen peak Rabi frequencies and detunings, which synthesize the inversion-about-average and oracle operators, each in a single shot.

A simple recipe for synthesizing the inversion-about-average operator was derived by factorizing the overall Hilbert space into a series of independent ladders. The coupling strengths between the MS states were determined solely through a consideration of the angular-momentum structure of the combined ionic pseudospin. The technique proposed in this paper raises the prospect of demonstrating Grover's algorithm in a moderately sized trapped-ion database comprising up to several hundred elements, and which scales exponentially with the number of ions; this is a necessary step on the path to demonstrating a practically useful quantum search, which remains a long-term goal.

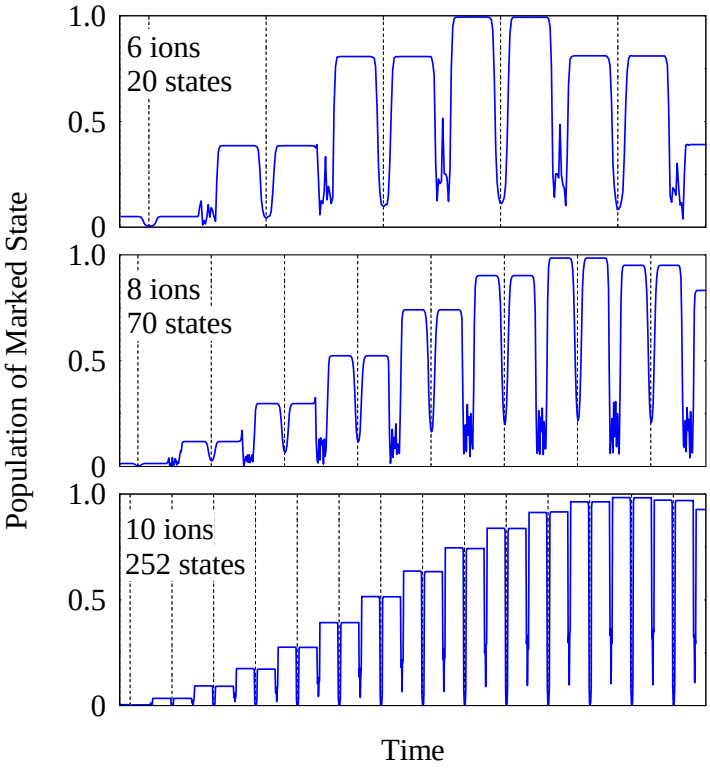

Figure 7.2: Simulation of the Grover search algorithm with N ions and $N/2$ excitations (register dimension $C^N_{N/2}$), for $N = 6$ (upper frame), $N = 8$ (middle frame) and $N = 10$ (lower frame). The system of ions is assumed to be initialized in the symmetric Dicke state $\left|W^N_{N/2}\right\rangle$. The laser pulses have a Gaussian shape, $g(t) = g_0 e^{-t^2/T^2}$. The thin vertical lines display the timing of the oracle call. The computed numerically scaled detunings and peak Rabi frequencies for the oracle and the inversion-about-average operator, respectively, are given in the table below. The marked-state population (the fidelity) of around 99% is obtained after $n_g = 3$, 6 and 12 steps, respectively, in exact agreement with Grover's value (6.5). The numerical simulation includes all off-resonant transitions to states with $m_j \neq 0$.

#ions	#elements	#steps	oracle		reflection	
N	$\mathcal{N}$	n_G	δT	$g_0 T$	δT	$g_0 T$
6	20	3	19.47	28.61	10.32	25.83
8	70	6	21.40	10.80	21.05	24.40
10	252	12	88.565	87.142	15.687	70.322

Chapter 8

Simulation of a quantum phase transition of polaritons with trapped ions

In this chapter a physical implementation of the Jaynes-Cummings-Hubbard (JCH) model using trapped ions is presented. The JCH model was proposed in the context of an array of coupled cavities, each containing a single two-state atom and a photon [101]. Such a system is described by the combination of two well-known physical models: the Hubbard model [102, 103], which describes the interaction and hopping of bosons in a lattice, and the Jaynes-Cummings model, which describes the interaction of an atom with a quantum field. The JCH model predicts a quantum phase transition of polaritons, which are collective photonic and atomic excitations. We shall show that the laser-driven ion chain in a linear Paul trap is described by a JCH Hamiltonian, wherein the ions and the phonons correspond, respectively, to the atoms and the photons in a coupled cavity array. As in [104], the position-dependent energy and the non-local hopping frequency of the phonons is controlled by the trapping frequencies, while the effective on-site repulsion is provided by the interaction of the phonons with the internal states of the ions and can be adjusted by the parameters of an external laser field, namely the Rabi frequency and the detuning. We shall show that many-body effects appear as a quantum phase transition between a localized Mott insulator (MI) and delocalized superfluid state (SF) of the composite phononic and internal (qubit) states of the ions. Due to the collective nature of the excitations we distinguish between collective qubit and phononic SF and MI phases, and the pure phononic SF phase, similar to the effects predicted in [106] for coupled cavity arrays.

8.1 Derivation of the Hamiltonian

Consider a chain of N ions confined in a linear Paul trap along the z axis with trap frequencies ω_q ($q = x, y, z$), where the radial trap frequencies are much larger than the axial trap frequency ($\omega_{x,y} \gg \omega_z$), so that the ions are arranged in a linear configuration and occupy equilibrium positions z_i^0 along the z axis. Making a Taylor expansion around the equilibrium position, and neglecting x^3, y^3, zx^2, zy^2 and higher order terms, the Hamiltonian in the radial direction x reads [66]

$$\hat{H}_x = \frac{1}{2M}\sum_{k=1}^{N}\hat{p}_k^2 + \frac{M\omega_x^2}{2}\sum_{k=1}^{N}\hat{x}_k^2 - \frac{M\omega_z^2}{2}\sum_{\substack{k,m=1\\k>m}}^{N}\frac{(\hat{x}_k-\hat{x}_m)^2}{|u_k-u_m|^3}. \tag{8.1}$$

Here $\hat{p}_k$ is the momentum operator, M is the ion mass, $\hat{x}_k$ is the position operator of the kth ion about its dimensionless equilibrium position u_k. In the Hamiltonian (8.1) the motion in the radial direction is decoupled from the axial motion. In terms of the normal modes ω_p, the Hamiltonian (8.1) reads $\hat{H}_x = \hbar\sum_{p=1}^{N}\omega_p(\hat{\tilde{a}}_p^\dagger\hat{\tilde{a}}_p + \frac{1}{2})$. Here $\hat{\tilde{a}}_p^\dagger$ and $\hat{\tilde{a}}_p$ are the phonon creation and annihilation operators of the pth *collective* phonon mode. However, if $\hat{x}_k$ and $\hat{p}_k$ are written in terms of *local* creation $\hat{a}_k^\dagger$ and annihilation $\hat{a}_k$ phonon operators, so that $\hat{x}_k = \sqrt{\hbar/2M\omega_x}\,(\hat{a}_k^\dagger + \hat{a}_k)$ and $\hat{p}_k = i\sqrt{\hbar M\omega_x/2}\,(\hat{a}_k^\dagger - \hat{a}_k)$, the Hamiltonian (8.1) reads

$$\hat{H}_x = \hbar\sum_{k=1}^{N}(\omega_x+\omega_k)\hat{a}_k^\dagger\hat{a}_k + \hbar\sum_{\substack{k,m=1\\k>m}}^{N}\kappa_{km}(\hat{a}_k^\dagger\hat{a}_m + \hat{a}_k\hat{a}_m^\dagger), \tag{8.2}$$

where we have neglected higher-order (energy non-conserving) terms. The phonons are trapped with a position-dependent frequency

$$\omega_k = -\frac{\alpha\omega_z}{2}\sum_{\substack{s=1\\s\neq k}}^{N}\frac{1}{|u_k-u_s|^3}, \tag{8.3}$$

where $\alpha = \omega_z/\omega_x$ ($\alpha \ll 1$), and they may hop between different ions, with non-local hopping strengths

$$\kappa_{km} = \frac{\alpha\omega_z}{2}\frac{1}{|u_k-u_m|^3} \tag{8.4}$$

derived from the long-range Coulomb interaction [104].

The collective and local creation and annihilation operators are connected by the Bogoliubov transformation,

$$\hat{\tilde{a}}_p^\dagger = \sum_{k=1}^{N} b_k^{(p)}(\hat{a}_k^\dagger\cosh\theta_p - \hat{a}_k\sinh\theta_p), \tag{8.5}$$

which preserves the commutation relation, $[\hat{a}_k, \hat{a}_m^\dagger] = \delta_{km}$. Here $\theta_p = -\frac{1}{4}\ln\gamma_p$, with $\gamma_p = 1+\alpha^2(1-\lambda_p)/2$ and λ_p are the eigenvalues, with eigenvectors $\mathbf{b}^{(p)}$, of the matrix $A_{km} = \delta_{km} +$

$2\sum_{s=1,s\neq k}(\delta_{km}-\delta_{sm})/|u_k-u_s|^3$ [66]. Using Eq. (8.5) one finds that the pth collective phonon state with zero phonons $|\widetilde{0}_p\rangle$ is a product of N local squeezed states, $|\widetilde{0}_p\rangle = |\zeta_1^{(p)}\rangle \ldots |\zeta_N^{(p)}\rangle$, where

$$|\zeta_k^{(p)}\rangle = \sum_{n_k=0}^{\infty} \sqrt{\frac{(2n_k-1)!!}{(2n_k)!!}} \frac{(\tanh\theta_p)^{n_k}}{\sqrt{\cosh\theta_p}} |2n_k\rangle. \tag{8.6}$$

Here $|2n_k\rangle$ $(k = 1, 2 \ldots N)$ is the local Fock state with $2n_k$ phonons. For the center-of-mass phonon mode we have $p = 1$ and $\cosh\theta_p = 1$; hence the collective ground state $|\widetilde{0}_1\rangle$ is a product of local ground states, $|\widetilde{0}_1\rangle = |0_1\rangle \ldots |0_N\rangle$. For a sufficiently small number of ions, we have $\cosh\theta_p \approx 1$ and $|\zeta_k^{(p)}\rangle \approx |0_k\rangle$. Since the lowest-energy collective vibrational mode in the radial direction is the highest mode $p = N$, we find that the SF ground state of the Hamiltonian (8.2) is

$$|\Psi_{\mathrm{SF}}\rangle = \frac{1}{\sqrt{N!}} \left(\sum_{k=1}^{N} b_k^{(N)} \hat{a}_k^{\dagger} \right)^N |0_1\rangle|0_2\rangle \ldots |0_N\rangle. \tag{8.7}$$

Here we have assumed the commensurate case where the number of ions is equal to the number of phonons. We find that the ratio between the average number of local phonons in the ground state is given by the square of the oscillation amplitudes: $\langle\hat{n}_k\rangle/\langle\hat{n}_m\rangle = (b_k^{(N)}/b_m^{(N)})^2$, where $\hat{n}_k = \hat{a}_k^{\dagger}\hat{a}_k$ is the local phonon number operator.

We shall show that the laser-ion interaction induces an effective repulsion between the local phonons. This interaction provides the phase transition from phononic SF state to composite SF and MI phases of the joint phononic and qubit excitations. Consider ion qubits with a transition frequency ω_0, which interact along the radial direction with a common travelling-wave laser light addressing the whole ion chain with frequency ω_{L}. The Hamiltonian of the system after the optical rotating-wave approximation is given by [107]

$$\hat{H} = \hat{H}_x + \hbar\Omega \left[\sum_{k=1}^{N} \hat{\sigma}_k^{+} \mathrm{e}^{\mathrm{i}\eta(\hat{a}_k^{\dagger}+\hat{a}_k)-\mathrm{i}\delta t} + \mathrm{h.c.} \right]. \tag{8.8}$$

Here $\hat{\sigma}_k^{+} = |e_k\rangle\langle g_k|$ and $\hat{\sigma}_k^{-} = |g_k\rangle\langle e_k|$ are the spin flip operators, $|e_k\rangle$ and $|g_k\rangle$ are the qubit states of the kth ion, Ω is the real-valued Rabi frequency, $\delta = \omega_{\mathrm{L}} - \omega_0$ is the laser detuning, and $\eta = |\mathbf{k}|x_0$ is the Lamb-Dicke parameter, with $\mathbf{k}$ the laser wave vector, and $x_0 = \sqrt{\hbar/2M\omega_x}$ is the spread of the ground-state wave function. The Hamiltonian, after transforming into the interaction picture by the unitary transformation $\hat{U} = \mathrm{e}^{\mathrm{i}\hat{H}_0 t/\hbar}$, with $\hat{H}_0 = -\hbar\omega_x \sum_{k=1}^{N} \hat{a}_k^{\dagger}\hat{a}_k + \hbar\Delta \sum_{k=1}^{N} |e_k\rangle\langle e_k|$, in the Lamb-Dicke limit and after the vibrational

rotating-wave approximation, reads

$$\begin{aligned}\hat{H}_I &= \hbar\sum_{k=1}^{N}\omega_k\hat{a}_k^\dagger\hat{a}_k + \hbar\Delta\sum_{k=1}^{N}|e_k\rangle\langle e_k| \\ &+\hbar g\sum_{k=1}^{N}(\hat{\sigma}_k^+\hat{a}_k + \hat{\sigma}_k^-\hat{a}_k^\dagger) \\ &+\hbar\sum_{\substack{k,m=1\\k>m}}^{N}\kappa_{km}(\hat{a}_k^\dagger\hat{a}_m + \hat{a}_k\hat{a}_m^\dagger),\end{aligned} \tag{8.9}$$

where $\hat{H}_I = \hat{U}^\dagger\hat{H}\hat{U} - \mathrm{i}\hbar\hat{U}^\dagger\partial_t\hat{U}$. We assume that the laser is tuned near the red motional sideband $\delta = -\omega_x - \Delta$, with a small detuning Δ ($\Delta \ll \omega_x$). The coupling between the internal qubit and local phonon states is $g = \eta\Omega$. The Hamiltonian (8.9) is valid when $\kappa_{km}, g \ll \omega_x$, which ensures that higher terms, which violate the conservation of the total number of excitations, can be neglected. The first three terms in Eq. (8.9) describe the Jaynes-Cummings model. The first two terms correspond to the energies of the local phonons and the ions, while the third term describes the laser-ion interaction. The fourth term in Eq. (8.9) describes the non-local hopping of phonons between different ions and allows the comparison to Hubbard systems. The Hamiltonian (8.9) commutes with the total excitation operator $\hat{N} = \sum_{k=1}^{N}\hat{N}_k$, hence the total number of excitations is conserved. Here $\hat{N}_k = \hat{a}_k^\dagger\hat{a}_k + |e_k\rangle\langle e_k|$ is the number operator of the total qubit and phononic excitations at the kth site. If the laser detuning δ is tuned near the blue motional sideband then the system is represented by the anti-Jaynes-Cummings dynamics, which shows equivalent behavior by redefinition of the excitation operator $\hat{N}_k = \hat{a}_k^\dagger\hat{a}_k + |g_k\rangle\langle g_k|$. In the following we only assume small detunings Δ around the red sideband transition, so that the anti-Jaynes-Cummings interaction does not occur.

In the JCH model the effective on-site interaction is provided by the interaction of phonons and qubit states at each site. The strength of the on-site interaction depends on external parameters, such as the Rabi frequency Ω and the laser detuning Δ. This interaction creates an energy gap, which prevents the absorption of additional phonons by each ion. When the hopping frequency is increased the energy gap decrease and a quantum phase transition occur between the SF and MI phase [108].

8.2 Numerical Demonstration and Interpretation

We describe the quantum phase transition between the MI and SF states by the variance $\mathcal{D}N_k = (\langle\hat{N}_k^2\rangle - \langle\hat{N}_k\rangle^2)^{1/2}$ of the number operator $\hat{N}_k$ with respect to the ground state of the

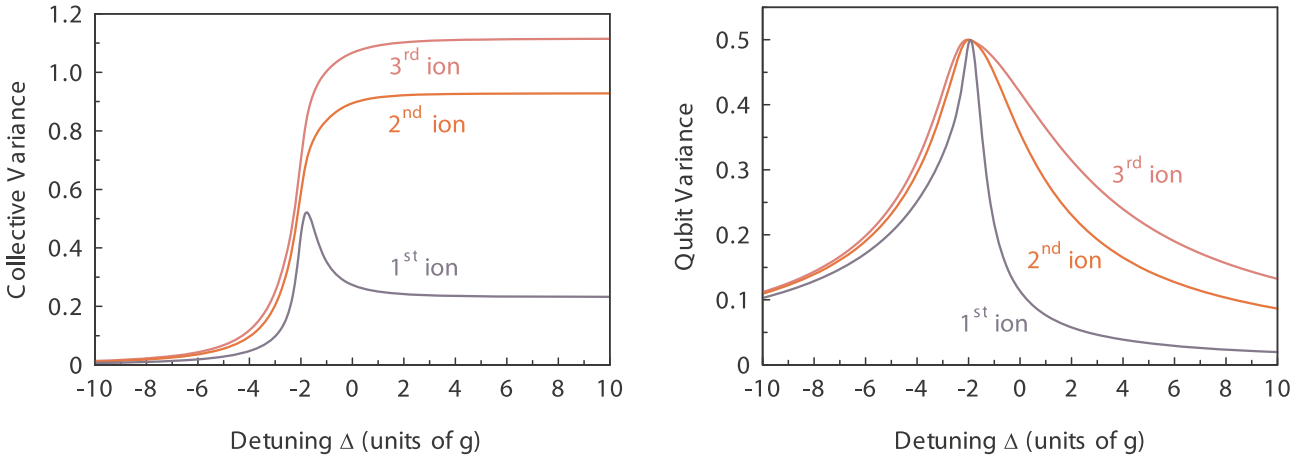

Figure 8.1: Total (qubit+phonon) variance $\mathcal{D}N_k$ (top) and the qubit variances $\mathcal{D}N_{a,k}$ ($k = 1, 2, 3$) (bottom) for a chain of five ions with five excitations as a function of the laser detuning Δ for fixed hopping $\kappa = 0.3g$. Negative values of Δ correspond to blue detuning with respect to the red-sideband transition.

Hamiltonian (8.9) for fixed number of excitations [106]. If the on-site interaction between the phonons dominates the hopping, the ground-state wave function is a product of local qubit and phononic states for each site with a fixed number of excitations. Hence in the MI state, the variance $\mathcal{D}N_k$ for any k vanishes. When the hopping term dominates the on-site interaction, then the ground state consists of a superposition of qubit and phononic states with delocalized excitations over the entire chain. In this state the variance $\mathcal{D}N_k$ at each site (i.e. each ion) is non-zero.

Figure 8.1 (top) shows the variance $\mathcal{D}N_k$ ($k = 1, 2, 3$) for a chain of five ions with five collective excitations versus the laser detuning Δ for fixed hopping frequency $\kappa = \alpha\omega_z/2$ calculated by an exact diagonalization of the Hamiltonian (8.9). Due to the symmetry of the trap with respect to the center it is not necessary to plot the phase diagrams for ions 4 and 5. For sufficiently large negative detuning Δ, there exists an energy gap, which prevents the absorption of additional phonons. Hence, the system is in the MI phase, where the qubit and phononic excitation are localized. When the detuning Δ increases, the energy gap decreases and the system makes a phase transition to the SF phase. The phase transition is stronger for the ions near the center of the trap due to stronger Coulomb interaction and increased hopping strengths, and weaker at the ends of the ion chain. The comparison between the variance at the different sites demonstrates two characteristic features. Firstly, there is a range of detunings where the qubit and phononic excitations at ion 1 (end of the chain) are predominantly in a MI phase, whereas the other ions are in the SF phase. Secondly, there is a broad range of Δ

along which the joint excitations at all ions are in the SF phase.

Figure 8.1 (bottom) shows the variance of the qubit excitations $\mathcal{D}N_{a,k}$ with $\hat{N}_{a,k} = |e_k\rangle\langle e_k|$ [106]. This allows us to distinguish the following phases: in the region of large negative detuning Δ the collective and the qubit variances are small, indicating that the system is in the qubit MI phase. Increasing the detuning, the collective variance stays small but the qubit variance increases, which shows that the system is indeed in a collective MI phase. Approaching $\Delta = 0$ the system makes a phase transitions into the collective qubit and phononic SF phase as now both collective and qubit variance are large. Finally, for sufficiently large positive detuning the qubit variance decreases but the collective variance stays large, which shows that the system is in the phononic SF phase.

The experiment is started by initializing the ion chain to the superfluid state (see Eq. 8.7) with N phonons in the lowest energy radial mode. To avoid off resonant excitation of unwanted radial modes, α could be increased temporarily so that $\omega_z/2\pi$ is increased to about 2 MHz. The lowest energy radial mode is then separated by $2\pi \cdot 0.5$ MHz from the other modes and is excited by a laser field on the blue sideband transition with more than 2μs duration [109]. Then $\omega_z/2\pi$ is decreased adiabatically within 10μs to $2\pi \cdot 0.1$ MHz. This leads to a hopping frequency $\kappa/2\pi$ of 0.5 kHz. Now the coupling laser is switched on. The experimental proof for the phase transition can be carried out by local measurements on a single ion which should be performed faster than the hopping time $(\kappa/u^3)^{-1}$, where u is the dimensionless average distance between two ions. In the case of 5 ions the hopping time amounts to 1 ms. For $^{40}Ca^+$ ions the qubit states could be represented by the ground state $S_{1/2}$ and the metastable state $D_{5/2}$. The laser, which creates the phonon-phonon repulsion, would be detuned to the red sideband of the quadrupole qubit transition between the two states. Then the readout could be performed by scattering photons on the dipole transition $S_{1/2} \rightarrow P_{1/2}$. This would lead to momentum recoil and changes of the phononic excitation, but to circumvent this we have to perform a measurement of the qubit states, which does not affect the phononic state as in the following steps. 1) Make a random guess for the qubit excitation. 2) If the guess was the $S_{1/2}$ ground state, then swap the population $S_{1/2} \Leftrightarrow D_{5/2}$ by a carrier π pulse leaving the phononic excitation unchanged. 3) Now expose the ion to laser light on the dipole transition. 4) If the ion scatters light the guess was wrong and we have to discard the measurement and restart, otherwise the initial guess was right and we transfer the qubit excitation back to the $S_{1/2}$ ground state by another carrier π pulse, then drive Rabi oscillations on the red sideband by perpendicular Raman light beams (difference momentum vector in the radial direction). 5) The phononic population can now be extracted by a Fourier analysis of the Rabi oscillations. In order to

minimize the major error source of heating of the radial phonon modes the whole procedure for our choice of parameters must be performed faster than the heating time of the radial phonons of 2 s, obtained by $1/\omega^2$ scaling [110] of the experimental radial heating rates [111]. This leaves enough time for state preparation, evolution and readout [112]. Fortunately the higher heating rates of the axial modes do not affect our scheme as they are decoupled from the radial modes.

In conclusion, we have proposed a novel implementation of the JCH model by trapped ions simulating polaritonic phase transitions in coupled cavity arrays. The system shows a MI to SF phase transition of the collective qubit and phononic excitation even with a small number of ions. The features can be easily measured by local addressing. Compared to atoms in optical cavities, our implementation is easier to manipulate, as all parameters can be tuned by changing the trap frequency, laser detuning and intensity. Additionally, the system can be extended by adding impurities of ions with different masses, which allows for simpler addressing of the radial phonon modes and a separation of coexistent phases.

Publications

Author's publications included in the thesis

1. G. S. Vasilev, S. S. Ivanov, and N. V. Vitanov
   Degenerate Landau-Zener model - Analytical solution,
   Phys. Rev. A **75**, 013417 (2007).

2. S. S. Ivanov and N. V. Vitanov,
   Steering quantum transitions between three crossing energy levels,
   Phys. Rev. A **77**, 023406 (2008).

3. S. S. Ivanov, P. A. Ivanov and N. V. Vitanov,
   Simple quantum search with trapped ions,
   Phys. Rev. A **78**, 030301 (2008).

4. M. Krug, T. Bayer, M. Wollenhaupt, C. Sarpe-Tudoran and T. Baumert; S. S. Ivanov and N. V. Vitanov,
   Coherent strong-field control of multiple states by a single chirped femtosecond laser pulse,
   New J. Phys. **11** 105051 (17pp) (2009).

5. P. A. Ivanov, S. S. Ivanov, N. V. Vitanov, A. Mering, M. Fleischhauer, and K. Singer,
   Simulation of a quantum phase transition of polaritons with trapped ions,
   Phys. Rev. A **80**, 060301 (2009).

6. S. S. Ivanov, P. A. Ivanov, I. E. Linington, N. V. Vitanov,
   Scalable quantum search using trapped ions,
   Phys. Rev. A **81**, 042328 (2010).

List of independent citations

Paper 1:

B. W. Shore, M. V. Gromovyy, L. P. Yatsenko, and V. I. Romanenko, A. J. Phys. **77** (2009)

H. Ribeiro, G. Burkard, Phys. Rev. Lett. **102**, 216802 (2009)

B. W. Shore, Acta Phys. Slovaca **58**, 243-486 (2008)

P. Foeldi, M. G. Benedict, European Phys. Journal (Special Topics) **160**, 175-181 (2008)

P. Foldi, M. G. Benedict, F.M. Peeters, Phys. Rev. A **77**, 013406 (2008)

Paper 2:

G. Dridi, S. Guerin, H. R. Jauslin, Phys. Rev. A **82**, 022109 (2010)

S. Vinjanampathy, A. R. P. Rau, J. Phys. A **42**, 425303 (2009)

A. R. Gorges, N. S. Bingham, M. K. DeAngelo, M. S. Hamilton, and J. L. Roberts, Phys. Rev. A **78**, 033420 (2008)

Paper 3:

Z. J. Deng, L. M. Liang, W. L. Yang, Int. J. Theor. Phys. **49**, 1904-1910 (2010)

W. L. Yang, H. Wei, F. Zhou, W. L. Chang and M. Feng, J. Phys. B **42**, 145503 (2009)

Paper 4:

C. Brif, R. Chakrabarti, H. Rabitz, New J. Phys. **12**, 075008 (2010)

S. Clow, T. Weinacht, Phys. Rev. A **82**, 023411 (2010)

H. Rabitz, N. J. Phys. **11**, 105030 (2009)

Paper 5:

S. Schmidt, G. Blatter, Phys. Rev. Lett. **104**, 216402 (2010)

J. Quach, M. I. Makin, C.-H. Su, A. D. Greentree, and L. C. L. Hollenberg, Phys. Rev. A **80**, 063838 (2009)

Contributions

In chapter two (part one) we calculate the propagator and the transition probabilities for a coherently driven quantum system with three-states, whose energies change linearly in time. We derive a highly accurate analytic approximation based on the two state Landau-Zener model, which is the most popular tool for estimating the transition probability between two states with crossing energies.

In chapter three (part one) a generalization of the famous Landau-Zener model is developed. We generalize the model to describe transitions between two degenerate sets of states and show some interesting effects: not all transition probabilities exist for infinite time duration.

In chapter four (part one) we present a theoretical interpretation for an experiment on selective population of particular quantum states in sodium atoms by an intensive chirped femtosecond laser pulse. By tuning one parameter – the chirp, selectivity among the population in the highly excited states $5p$, $6p$, $7p$ and $5f$, $6f$ is achieved. We built a mainly qualitative five-state model for the predominant excitation channel to provide insights into the physical mechanisms at play.

In chapter six and seven (part two) we propose a simple implementation of Grover's quantum search algorithm with a linearly (chapter six) and exponentially (chapter seven) growing with the number of ions databases. Utilizing the physical symmetries of the trapped-ion linear crystal, the physical realization of the algorithm represents a dramatic simplification: each logical iteration (oracle and inversion about average) requires only *two* physical interaction steps, in contrast to the large number of concatenated gates required by previous approaches. This not only facilitates the implementation, but also increases the overall fidelity of the algorithm.

In chapter eight (part two) we propose a novel implementation of the JCH model by trapped ions simulating polaritonic phase transitions in coupled cavity arrays. The system shows a MI to SF phase transition of the collective qubit and phononic excitation even with a small number of ions. This implementation is easy to manipulate, as all parameters can be tuned by changing the trap frequency, laser detuning and intensity.

Bibliography

[1] L.D. Landau, Phys. Z. Sowjetunion **2**, 46 (1932); C. Zener, Proc. Roy. Soc. (Lond) **A137**, 696 (1932).

[2] L.K. Grover, Phys. Rev. Lett. **79**, 325 (1997).

[3] K.-A. Brickman *et al.*, Phys. Rev. A **72**, 050306(R) (2005); M. Feng, Phys. Rev. A **63**, 052308 (2001); C.D. Hill and H.-S. Goan, *ibid.* **69**, 056301 (2004).

[4] B. W. Shore, *The Theory of Coherent Atomic Excitation* (Wiley, New York, 1990).

[5] L. Allen and J. H. Eberly, *Optical Resonance and Two-Level Atoms*, (Wiley, New York, 1975).

[6] N. V. Vitanov, Z. Kis, and B. W. Shore, Phys. Rev. A **68**, 063414 (2003).

[7] E. S. Kyoseva and N. V. Vitanov, Phys. Rev. A **73**, 023420 (2006).

[8] Z. Kis, A. Karpati, B. W. Shore, and N. V. Vitanov, Phys. Rev. A **70**, 053405 (2004).

[9] N. V. Vitanov and B. M. Garraway, Phys. Rev. A **53**, 4288 (1996).

[10] B. Broers, H. B. van Linden van den Heuvell, and L. D. Noordam, Phys. Rev. Lett. **69**, 2062 (1992); B. Broers, L. D. Noordam, and H. B. van Linden van den Heuvell, Phys. Rev. A **46**, 2749 (1992); R. B. Vrijen, G. M. Lankhuijzen, D. J. Maas, and L. D. Noordam, Comments At. Mol. Phys. **33**, 67 (1996).

[11] N.V. Vitanov and K.-A. Suominen, Phys. Rev. A **56**, R4377 (1997).

[12] C.E. Carroll and F.T. Hioe, J. Phys. A: Math. Gen. **19**, 1151 (1986); C.E. Carroll and F.T. Hioe, J. Phys. A: Math. Gen. **19**, 2061 (1986).

[13] V.N. Ostrovsky and H. Nakamura, J. Phys. A **30**, 6939 (1997).

[14] D.A. Harmin, Phys. Rev. A **44**, 433 (1991).

[15] S. Brundobler and V. Elser, J. Phys. A **26**, 1211 (1993).

[16] N. V. Vitanov and B. Girard, Phys. Rev. A **69**, 033409 (2004).

[17] R. G. Unanyan, N. V. Vitanov, and K. Bergmann, Phys. Rev. Lett. **87**, 137902 (2001); R. G. Unanyan, M. Fleischhauer, N. V. Vitanov, and K. Bergmann, Phys. Rev. A **66**, 042101 (2002).

[18] A. A. Rangelov, J. Piilo, and N. V. Vitanov, Phys. Rev. A **72**, 053404 (2005).

[19] A.V. Shytov, Phys. Rev. A **70**, 052708 (2004).

[20] M.V. Volkov and V.N. Ostrovsky, J. Phys. B: At. Mol. Opt. Phys. **37**, 4069 (2004).

[21] N. V. Vitanov, Phys. Rev. A **59**, 988 (1999).

[22] Y.N. Demkov and V. I. Osherov, Zh. Eksp. Teor. Fiz. **53**, 1589 (1967) [Sov. Phys. JETP **26**, 916 (1968)].

[23] Y.N. Demkov and V.N. Ostrovsky, J. Phys. B **28**, 403 (1995).

[24] B. M. Garraway and N. V. Vitanov, Phys. Rev. A **55**, 4418 (1997).

[25] National Institute of Standards and Technology, *http://www.nist.gov*

[26] A. Präkelt, M. Wollenhaupt, C. Sarpe-Tudoran, T. Baumert, Phys. Rev. A **70**, 0634707 (2004)

[27] A. Präkelt, M. Wollenhaupt, A. Assion, C. Horn, C. Sarpe-Tudoran, M. Winter, T. Baumert, Rev. Sci. Instrum. **74**, 4950 (2003)

[28] M. Wollenhaupt, A. Präkelt, C. Sarpe-Tudoran, D. Liese, T. Baumert, Appl. Phys. B **82**, 183 (2006)

[29] B. Whitaker, *Imaging in Molecular Dynamics* (Cambridge University Press, 2003)

[30] G. A. Garcia, L. Nahon, I. Powis, Rev. Sci. Instrum. **75**, 4989 (2004)

[31] M. Wollenhaupt, M. Krug, J. Köhler, T. Bayer, C. Sarpe-Tudoran, T. Baumert, Appl. Phys. B **95**, 245 (2009)

[32] M. Wollenhaupt, M. Krug, J. Köhler, T. Bayer, C. Sarpe-Tudoran, T. Baumert, Appl. Phys. B (2009), in print

[33] A. Assion, T. Baumert, J. Helbing, V. Seyfried, G. Gerber, Chem. Phys. Lett. **259**, 488 (1996)

[34] P. Avan, C. Cohen-Tannoudji, J. Dupont-Roc, C. Fabre, J. de Phys. **37**, 993 (1976)

[35] A. L'Huillier, L. A. Lompré, D. Normand, X. Tang, P. Lambropoulos, J. Opt. Soc. Am. B **6**, 1790 (1989)

[36] M. J. Seaton, Rep. Prog. Phys. **46**, 167 (1983)

[37] S. N. Dixit, P. Lambropoulos, Phys. Rev. A **27**, 861 (1983)

[38] G. Leuchs, S. J. Smith, S. N. Dixis, P. Lambropoulos, Phys. Rev. Lett. **56**, 708 (1986)

[39] M. Wollenhaupt, A. Präkelt, C. Sarpe-Tudoran, D. Liese, T. Bayer, T. Baumert, Phys. Rev. A **73**, 063409 (2006)

[40] M. Wollenhaupt, T. Bayer, M. Krug, C. Sarpe-Tudoran, T. Baumert, J. Phys. Conf. Ser. **88**, 012053 (2007)

[41] N. V. Vitanov, T. Halfmann, B. W. Shore, K. Bergmann, Annu. Rev. Phys. Chem. **52**, 763 (2001)

[42] B. W. Shore, *The Theory of Coherent Atomic Excitation, Vol. I* (Wiley, New York, 1990)

[43] B. W. Shore, Act. Phys. Slov. **58**, 243 (2008)

[44] C. E. Carroll, F. T. Hioe, J. Phys. A **19**, 1151 (1986)

[45] C. E. Carroll, F. T. Hioe, J. Phys. A **19**, 2061 (1986)

[46] V. N. Ostrovsky, H. Nakamura, J. Phys. A **30**, 6939 (1997)

[47] D. A. Harmin, Phys. Rev. A **44**, 433 (1991)

[48] S. Brundobler, V. Elser, J. Phys. A **26**, 1211 (1993)

[49] S. Zamith, J. Degert, S. Stock, B. de Beauvoir, V. Blanchet, M. A. Bouchene, B. Girard, Phys. Rev. Lett. **87**, 033001 (2001)

[50] T. Rickes, L. P. Yatsenko, S. Steuerwald, T. Halfmann, B. W. Shore, N. V. Vitanov, K. Bergmann, J. Chem. Phys. **113**, 534 (2000)

[51] S. D. Clow, C. Trallero-Herrero, T. Bergeman, T. Weinacht, Phys. Rev. Lett. **100**, 233603 (2008)

[52] M. Wollenhaupt *et al.*, in *Springer Handbook of Lasers and Optics*, Ch. 12 (Springer, 2007)

[53] L. Allen and J. H. Eberly, *Optical Resonance and Two-Level Atoms* (Dover, New York, 1975); F. T. Hioe, Phys. Rev. A **30**, 2100 (1984).

[54] E.S. Kyoseva and N.V. Vitanov, Phys. Rev. A **73**, 023420 (2006).

[55] J. R. Morris and B. W. Shore, Phys. Rev. A **27**, 906 (1983).

[56] F. R. Gantmacher, *Matrix Theory* (Springer, Berlin, 1986).

[57] N. V. Vitanov and B. M. Garraway, Phys. Rev. A **53**, 4288 (1996).

[58] F. T. Hioe, Phys. Rev. A **30**, 2100 (1984).

[59] N. V. Vitanov, J. Phys. B **33**, 2333 (2000); N. V. Vitanov, Z. Kis, and B. W. Shore, Phys. Rev. A **68**, 063414 (2003); Z. Kis, A. Karpati, B. W. Shore, and N. V. Vitanov, Phys. Rev. A **70**, 053405 (2004).

[60] J. I. Cirac and P. Zoller, Phys. Rev. Lett. **74**, 4091 (1995).

[61] L.D. Landau, E.M. Lifshitz, Mechanics, page 122 (1988).

[62] W. Paul, Reviews of Modern Physics 62 (3): 531-540 (1990).

[63] D. Leibrfried, R. Blatt, C. Monroe and D. Wineland, Rev. Mod. Phys. **75**, 281 (2001).

[64] M. Abramowitz and I. A. Stegun, *Handbook of Mathematical Functions* (Dover, New York, 1964).

[65] C. Monroe, D. M. Meekhof, B. E. King, S. R. Jefferts, W. M. Itano, and D. J. Wineland, Phys. Rev. Lett. **75**, 4011 (1995).

[66] D. F. V. James, Appl. Phys. B **66**, 181 (1998).

[67] A. Steane, Appl. Phys. B **64**, 623 (1997).

[68] D. G. Enzer, M. M. Schauer, J. J. Gomez, M. S. Gulley, M. H. Holzscheiter, P. G. Kwiat, S. K. Lamoreaux, C. G. Peterson, V. D. Sandberg, D. Tupa, A. G. White, and R. J. Hughes, Phys. Rev. Lett. **85**, 2466 (2000).

[69] D. J. Wineland, C. Monroe, W. M. Itano, D. Leibfried, B. E. King, and D. M. Meekhof, J. Res. Natl. Inst. Stand. Technol. **103**, 259 (1998).

[70] D. J. Wineland and W. M. Itano, Phys. Rev. A **20**, 1521 (1979); W. Vogel and R. L. de Matos Filho, Phys. Rev. A **52**, 4214 (1995).

[71] E. T. Jaynes and F. W. Cummings, Proc. IEEE, **51**, 89 (1963).

[72] A. S. Householder, Journal of the ACM **5** (4): 339-342 (1958).

[73] J. H. Wilkinson, Comput. J. **3**, 23 (1960).

[74] A. Barenco, C. H. Bennett, R. Cleve, D. P. DiVincenzo, N. Margolus, P. Shor, T. Sleator, J. A. Smolin, and H. Weinfurter, Phys. Rev. A **52**, 3457 (1995).

[75] A. S. Householder, J. ACM **5**, 339 (1958).

[76] P. A. Ivanov, E. S. Kyoseva, and N. V. Vitanov, Pys. Rev. A **74**, 022323 (2006).

[77] P. A. Ivanov, B. T. Torosov, and N. V. Vitanov, Pys. Rev. A **75**, 012323 (2007).

[78] P. A. Ivanov and N. V. Vitanov, Pys. Rev. A **77**, 012335 (2008).

[79] A. A. Rangelov, N. V. Vitanov, and B. W. Shore, Phys. Rev. A **77**, 033404 (2008).

[80] G. L. Long, Phys. Rev. A **64**, 022307 (2001).

[81] G. L. Long, Y. S. Li, W. L. Zhang, L. Niu, Phys. Lett. A **262** (1999) 27-34.

[82] P. Hoyer, Phys. Rev. A **62**, 052304 (2000).

[83] B.E. King *et al.*, Phys. Rev. Lett. **81**, 1525 (1998).

[84] P.A. Ivanov and N.V. Vitanov, Phys. Rev. A **77**, 012335 (2008).

[85] P.A. Ivanov *et al.*, Phys. Rev. A **74**, 022323 (2006).

[86] P.A. Ivanov *et al.*, Phys. Rev. A **75**, 012323 (2007).

[87] E.S. Kyoseva and N.V. Vitanov, Phys. Rev. A **73**, 023420 (2006).

[88] H. Häffner *et al.*, Nature (London) **438**, 643 (2005).

[89] I.E. Linington and N.V. Vitanov, Phys. Rev. A **77**, 010302(R) (2008).

[90] I.E. Linington and N.V. Vitanov, to be published.

[91] G.L. Long, Phys. Rev. A **64**, 022307 (2001).

[92] L.K. Grover, Phys. Rev. Lett. **80**, 4329 (1998).

[93] E. Biham *et al.*, Phys. Rev. A **60**, 2742 (1999).

[94] J.-Y. Hsieh and C.-M. Li, Phys. Rev. A **65**, 052322 (2002).

[95] I. E. Linington and N. V. Vitanov, Phys. Rev. A **77**, 010302(R) (2008).

[96] A. A. Rangelov, N. V. Vitanov, and B. W. Shore, Phys. Rev. A **74**, 053402 (2006).

[97] D. B. Hume, C. W. Chou, T. Rosenband, and D. J. Wineland, Phys. Rev. A **80**, 052302 (2009).

[98] I. E. Linington and N. V. Vitanov, Phys. Rev. A **77**, 062327 (2008).

[99] N. V. Vitanov, B. W. Shore, L. Yatsenko, K. Böhmer, T. Halfmann, T. Rickes, and K. Bergmann, Opt. Commun. **199**, 117 (2001).

[100] E. S. Kyoseva, N. V. Vitanov, B. W. Shore, J. Mod. Opt **54**, 2237 (2007).

[101] A. D. Greentree *et al.*, Nat. Phys. **2**, 856 (2006); M. J. Hartmann *et al.*, Nat. Phys. **2**, 849 (2006); D. G. Angelakis *et al.*, Phys. Rev. A **76**, 031805(R) (2007); M. I. Makin *et al.*, Phys. Rev. A **77**, 053819 (2008); D. Rossini and R. Fazio, Phys. Rev. Lett. **99**, 186401 (2007).

[102] J. Hubbard, Proc. Roy. Soc. A **276**, 238 (1963).

[103] M. P. A. Fisher *et al.*, Phys. Rev. B **40**, 546 (1989).

[104] D. Porras and J. I. Cirac, Phys. Rev. Lett. **93**, 263602 (2004); X. L. Deng *et al.*, Phys. Rev. A **77**, 033403 (2008).

[105] A. Imamoglu *et al.*, Phys. Rev. Lett. **79**, 1467 (1997). K. M. Birnbaum *et al.*, Nature **436**, 87 (2005).

[106] E. K. Irish *et al.*, Phys. Rev. A **77**, 033801 (2008).

[107] D. J. Wineland *et al.*, J. Res. Natl. Inst. Stand. Technol. **103**, 259 (1998).

[108] A. Mering *et al.*, arXiv/quant-ph: 0907.1876 (2009).

[109] S.-L. Zhi *et al.*, Phys. Rev. Lett. **97**, 050505 (2006).

[110] L. Deslauriers *et al.*, Phys. Rev. Lett. **97**, 103007 (2006).

[111] F. Schmidt-Kaler *et al.*, J. Phys. B: At. Mol. Opt. Phys. **36**, 623 (2003).

[112] A. H. Myerson *et al.*, Phys. Rev. Lett. **100**, 200502 (2008).